Structure of the QCD vacuum and low-lying eigenmodes of the Wilson-Dirac Operator

Douglas Andrew Smith

Doctor of Philosophy

The University of Edinburgh

1997

To my mother

Abstract

This thesis details a study of the vacuum structure of QCD using the tool of lattice gauge theory.

Chapter 1 gives an introduction to path integrals, semi-classical approximations to path integrals, instantons, topological charge and instanton phenomenology.

Chapter 2 introduces lattice gauge theory and the problems of studying topological charge on the lattice. The cooling method and its pitfalls are discussed and details are given of a study undertaken of under-relaxed cooling.

In Chapter 3 the algorithms that were developed to study the instantons on the cooled configurations are discussed.

Chapter 4 gives the results for the structure of the vacuum: size distributions, spatial distributions, correlations between charges, and scaling of distributions with the lattice spacing.

Chapter 5 discusses an exploratory study of the low-lying eigenmodes of the Wilson-Dirac operator. The zero-modes of both the unimproved and improved operators on cold and heated instantons are calculated and the lattice artefacts investigated.

Chapter 6 contains my conclusions and suggestions for future work.

Acknowledgements

I would like to thank my supervisors Ken Bowler and Brian Pendleton. I would also like to thank my collaborators, Mike Teper and Hubert Simma, for working with me on the projects described in this thesis. My PhD was funded by the Carnegie Trust for the Universities of Scotland, whose support and funding of trips to conferences I gratefully ackowledge. I would also like to thank Ken, Brian, Mike and Hubert for their careful reading of this thesis.

My thanks to my colleagues in EDQCD; Peter, Zbysek, Harry, Stephen, Paul, Chris, David, Joyce, Gary and Balint for making my life in Edinburgh a great deal of fun.

Finally I would like to thank my Mum for her love and support throughout my PhD.

Contents

Chapter 1

Quantum Chromodynamics

Quantum Chromodynamics (QCD) is the theory of the strong interactions. It is a gauge theory based on the non-abelian group $SU(3)$. The quanta of this theory, the gluons, carry colour charge and interact both with quarks and with themselves.

The early quark models, postulating that hadrons were made up of fractionally charged spin-half particles, were successful in accounting for many observed hadron properties. However they predicted that the wave-functions of the baryons were symmetric under interchange of quarks which because of Fermi's Principle was clearly wrong. This and the problem of unobserved states was solved by the introduction of the colour degree of freedom which allowed the baryon wave-functions to be made anti-symmetric under interchange of the quarks. Quarks are now assumed to come in 3 colours which form a triplet under $SU(3)$. Because colour is not observed, quarks are assumed to be confined and only observed in $q\bar{q}$ or qqq states. The mechanism of confinement is still not understood.

QCD possesses the property of asymptotic freedom[1][2]; at high energies the coupling is small, allowing a perturbative calculation of high energy processes to be carried out. At low energies, however, the coupling is $O(1)$ and perturbation theory cannot be used. This means that other, non-perturbative, methods must be used to extract predictions of, for example, the hadron spectrum at low energies.

1.1 Gauge Theories

In QCD the quark fields transform as a triplet under $SU(3)$. Consider the Lagrangian density for free quarks

$$\mathcal{L} = \bar{\psi}(i\partial\!\!\!/ - m)\psi \tag{1.1}$$

The *colour* coordinates are internal degrees of freedom. The physical observables are postulated to be independent of how these phases are chosen i.e. physics is invariant under transformations of the form

$$\psi(x) \rightarrow \Lambda^{-1}(x)\psi(x) \tag{1.2}$$

but $\mathcal{L}$ is not invariant under these transformations. In order to make $\mathcal{L}$ invariant a new field $A_\mu(x)$ must be introduced and the derivatives changed to covariant derivatives. $\mathcal{L}$ now becomes

$$\mathcal{L} = \bar{\psi}(i\not{D} - m)\psi \tag{1.3}$$

where

$$\not{D} = \gamma^\mu(\partial_\mu + A_\mu) \tag{1.4}$$

The field $A_\mu(x) = gA^a_\mu T^a$ is called a gauge field, g is the gauge coupling constant and T^a are the generators of the gauge group. The transformation of $A_\mu(x)$ under gauge transforms is given by

$$A_\mu(x) = \Lambda^{-1}(x)(\partial_\mu + A_\mu(x))\Lambda(x) \tag{1.5}$$

The dynamics of the gauge-field are described by the Yang-Mills Lagrangian

$$\mathcal{L}_{YM} = \frac{1}{4g^2}\mathrm{tr}(F^{\mu\nu}F_{\mu\nu}) \tag{1.6}$$

where

$$F_{\mu\nu} = \partial_\mu A_\nu - \partial_\nu A_\mu + [A_\mu, A_\nu] \tag{1.7}$$

If the gauge field is non-Abelian, as in QCD, then the commutator is non-zero so the Yang-Mills action contains cubic and quartic self-interactions of the gauge-field. The gauge-field may be considered on its own which is called *Pure Yang-Mills Theory*

Covariant differentiation can be introduced in another way. The invariance under local gauge transformations is equivalent to physics being invariant under a local choice of basis of the colour fields.

Let $\mathcal{C}_{y,x}$ be a path connecting points x and y and ϕ be any field with colour indices. With each path we can associate an $SU(3)$ matrix. Then $U(\mathcal{C}_{y,x})\phi(x)$ is defined to be $\phi(x)$ parallel transported along the curve to y.

Under a gauge transform the parallel transporter transforms as

$$U(\mathcal{C}_{yx}) \to \Lambda^{-1}(y)U(\mathcal{C}_{yx})\Lambda(x) \tag{1.8}$$

Covariant differentiation is defined as follows. If we wish to compare the fields at points x and $x + dx$ then because the basis of the fields can be chosen independently at each point we must parallel transport the field at $x + dx$ to the field x. Because the points are infinitesimally far apart U only differs infinitesimally from the unit matrix

$$U(\mathcal{C}_{x,x+dx}) = 1 - A_\mu dx^\mu \tag{1.9}$$

and

$$\mathcal{D}\phi(x) = U^{-1}(\mathcal{C}_{x,x+dx})\phi(x + dx) - \phi(x) \tag{1.10}$$

$\mathcal{D}\phi(x) = \mathcal{D}_\mu\phi(x)dx^\mu$ then gives

$$\mathcal{D}_\mu\phi(x) = (\partial_\mu + A_\mu)\phi(x) \tag{1.11}$$

The transformation law of $U(\mathcal{C})$ gives the transformation law of the gauge-field.

The effect of parallel transporting the field $\phi(x)$ to a point y can be calculated by exponentiating 1.9 which gives

$$U(y,x) = \exp \int_x^y A_\mu(x')dx' \tag{1.12}$$

The field strength tensor $F_{\mu\nu}$ corresponds to the curvature tensor in general relativity. By parallel transporting around a parallelogram of sides dx^μ and dy^ν it is found that

$$U(\mathcal{C}_{xx}) = 1 - F_{\mu\nu}dx^\mu dy^\nu \tag{1.13}$$

and the field strength tensor transforms as

$$F_{\mu\nu} \to \Lambda^{-1}(x)F_{\mu\nu}\Lambda(x) \tag{1.14}$$

.

1.2 Path Integrals

Modern Quantum Field Theory (QFT) is written down in terms of path integrals. In Minkowski space, an observable is calculated from

$$\left\langle 0 \left| \hat{T}(\phi(x_1)..\phi(x_N)) \right| 0 \right\rangle = \frac{\int \mathcal{D}\phi e^{\frac{iS[\phi]}{\hbar}} \phi(x_1)...\phi(x_N)}{\int \mathcal{D}\phi e^{\frac{iS[\phi]}{\hbar}}} \tag{1.15}$$

where $\phi(x)$ is a field defined over all space-time and $\hat{T}$ denotes time-ordering. The integration takes place over all possible field configurations. $S[\phi]$ is the action of the configuration $\phi(x)$.

This integral is mathematically not well defined and is unsuitable for numerical simulations. However it can be continued to imaginary time (Euclidean space-time) where these problems are solved.

In Euclidean Space the path integral resembles a Boltzman ensemble with parti-

tion function

$$\mathcal{Z} = \int \mathcal{D}\phi e^{-\frac{S_E[\phi]}{\hbar}} \tag{1.16}$$

where $S_E[\phi]$ is the action in Euclidean space. The probability density is now well defined and can be simulated numerically.

As in quantum mechanics it is possible to do semi-classical approximations; in quantum mechanics, if $\hbar$ is assumed to be small then the WKB approximation can be used to solve the Schroedinger Equation. In QFT an approximation to the path-integral may be obtained in the small $\hbar$, semi-classical limit. Consider Yang-Mills theory,

$$\frac{S}{\hbar} = \frac{1}{4g^2\hbar}\mathrm{tr}\int(FF) \tag{1.17}$$

The quantity $g^2\hbar$ appears in the path integral and it can be seen that the small $\hbar$ limit is equivalent to the weak-coupling regime. For $\hbar$ small the Euclidean path integral will be dominated by paths that maximise $e^{-S_E[\phi]}$ i.e. paths close to the classical path. An expansion is made around each stationary point of the action and to first order the functional integrals are gaussian.

Consider a particle in 1 dimension moving in a potential $V(x)$. The energy of the particle is given by $E = \frac{p^2}{2m} + V(x)$ and classically it is only allowed in regions where $E > V(x)$. In Quantum Mechanics however the particle can tunnel through regions where $E < V(x)$. The amplitude for transmission through a potential barrier obeys the WKB formula

$$T(E) = \exp\left\{\frac{-1}{\hbar}\int_{-a}^{a} dx[2m(V-E)]^{\frac{1}{2}}\right\} \tag{1.18}$$

where $-a$ and a are the semi-classical turning points at energy E (assume $V(x) = V(-x)$). This is a semi-classical, weak-coupling, approximation but the amplitude vanishes more quickly than any power of $\hbar$ and hence of g^2 and so is not seen to any order of perturbation theory. In order for the particle to move in classically forbidden regions it would have to have imaginary momentum. This can be introduced by rotating the equations of motion to imaginary time $t = i\tau$. The energy of the particle now becomes $E = \frac{p^2}{2m} - V(x)$ and the particle can

now move in classically forbidden regions; tunnelling can be seen as motion in imaginary time.

The classical tunnelling solution, the centre point of the gaussian integral, is called an instanton. The instanton interpolates between $x = -a$ at $t = -\infty$ to $x = a$ at $t = \infty$. There will also be anti-instantons corresponding to tunnelling in the opposite direction ($x = a$ at t=$-\infty$ and $x = -a$ at $t = \infty$. Instantons are localised objects; to see this consider a potential $V(x)$ such that $V(-a) = V(a) = 0$ and $E = 0$. For $t \to \infty$, $x \to a$ and expanding the potential shows the equations of motion can be approximated by

$$\frac{d^2x}{dt^2} = V''(a)(a - x) \tag{1.19}$$

and

$$x = a - e^{-V''(a)t} \tag{1.20}$$

The instantons are localised objects, in this case of fixed size $\frac{1}{V''(a)}$. This localisation is important. It means that approximate solutions of the equations of motion can be constructed from strings of widely separated instantons and anti-instantons. This is the dilute gas approximation; it is assumed that the time between tunnellings (the separation of the instantons) is very much greater than the time taken to tunnel (the size of the instanton). The transition amplitude from one state to another will be given by sums over all possible strings of instantons and anti-instantons connecting to the 2 states. Exactly the same ideas can be applied to quantum field theory where the classical solutions of the field equations are studied. A fuller discussion of instantons can be found in [3].

1.3 Instantons in Yang-Mills Theories

For Yang-Mills theories in 4 dimensional Euclidean space-time, finite action implies

$$F_{\mu\nu} = O(\frac{1}{r^3}) \tag{1.21}$$

as $r \to \infty$.

This implies that as $r \to \infty$, A_μ is a gauge transform of zero. A_μ therefore has the form

$$A_\mu = g^\dagger \partial_\mu g + O(\frac{1}{r^2}) \tag{1.22}$$

as $r \to \infty$. g is a continuous function of the angular variables only. If the gauge group is $SU(2)$ then the function g describes a mapping $S^3 \to S^3$; a mapping from the surface at infinity of space-time onto the sphere S^3 of $SU(2)$. These mappings fall into topologically distinct classes; homotopy classes. A member of a homotopy class is continuously deformable into any another member of the same homotopy class but cannot be continously deformed into a member of a different homotopy class. Mathematically homotopy is defined as follows[4]. Consider 2 continuous maps α_1 and α_2 from a topological space X to a topological space Y;

$$\alpha_1 : X \to Y$$
$$\alpha_2 : X \to Y$$

The map α_1 is said to be homotopic to the map α_2 if $\exists$ a function F

$$F : X \times [0,1] \to Y, F \text{ continuous} \tag{1.23}$$

and F satisfies

$$F(x,0) = \alpha_1(x) \tag{1.24}$$
$$F(x,1) = \alpha_2(x) \tag{1.25}$$

Each homotopy class is characterised by a unique integer, the winding number or topological charge, Q. The winding number can thought of as the number of times the space X covers, or winds round, Y.

The winding number is additive; if $g = g_1 g_2$ with Q_i the winding number of g_i then the winding number Q of g is given by

$$Q = Q_1 + Q_2 \tag{1.26}$$

The topological charge is defined in terms of a (gauge dependent) current

$$K_\alpha = 4\epsilon_{\alpha\beta\gamma\delta}\mathrm{tr}(A_\beta\partial_\gamma A_\delta + \frac{2}{3}A_\beta A_\gamma A_\delta) \tag{1.27}$$

with

$$Q = \int d\underline{r}^\alpha K_\alpha \tag{1.28}$$

where $\underline{r}^\alpha$ is the normal vector to the surface at infinity. This integral over the surface at infinity can also be expressed in terms of an integral over all space by the divergence theorem thus

$$Q = \frac{1}{32\pi^2}\int d^4x \mathrm{tr} F_{\mu\nu}\tilde{F}_{\mu\nu} \tag{1.29}$$

where

$$\tilde{F}_{\mu\nu} = \frac{1}{2}\epsilon_{\mu\nu\rho\sigma}F_{\rho\sigma} \tag{1.30}$$

the dual of F. The quantity

$$Q(x) = \frac{1}{32\pi^2}\mathrm{tr}F_{\mu\nu}\tilde{F}_{\mu\nu} \tag{1.31}$$

is called the topological charge density.

The derivation of the instanton solution starts from the identity

$$\mathrm{tr}\int d^4x(F_{\mu\nu} \pm \tilde{F}_{\mu\nu})^2 \geq 0 \tag{1.32}$$

Now as

$$(F_{\mu\nu} \pm \tilde{F}_{\mu\nu})^2 = 2(F_{\mu\nu}F_{\mu\nu} \pm F_{\mu\nu}\tilde{F}_{\mu\nu}) \tag{1.33}$$

$$\mathrm{tr}\int d^4x F_{\mu\nu}F_{\mu\nu} \geq \left|\mathrm{tr}\int d^4x F_{\mu\nu}\tilde{F}_{\mu\nu}\right| = 32\pi^2 Q \tag{1.34}$$

and this gives the inequality

$$S \geq \frac{8\pi^2}{g^2}|Q| \tag{1.35}$$

The action is minimised i.e. $S = \frac{8\pi^2}{g^2}$ for (anti-) self dual solutions $F_{\mu\nu} = (\pm)\tilde{F}_{\mu\nu}$.

This gives a set of first order equations which can solved to find the instanton solution. For $Q = 1$ the instanton solution is

$$A_\mu = \frac{g^\dagger(x)\partial_\mu g(x)}{x^2 + \rho^2} \tag{1.36}$$

where

$$g(x) = \frac{1}{|x|}(x_4 + i\mathbf{x}.\sigma) \tag{1.37}$$

and $|x^2| = x_4^2 + \mathbf{x}^2$ The solution is [5]

$$A_\mu^a(x) = 2\frac{\eta_{a\mu\nu}x_\nu}{x^2 + \rho^2} \tag{1.38}$$

The gauge-fields can also be expressed in the singular gauge where there is a singularity in the gauge field

$$A_\mu^a = \frac{2\bar{\eta}_{a\mu\nu}x_\nu\rho^2}{x^2(x^2 + \rho^2)} \tag{1.39}$$

The η symbols are defined by

$$\eta_{a\mu\nu} = \epsilon_{a\mu\nu} + \delta_{a\mu}\delta_{\nu 4} - \delta_{a\nu}\delta_{\mu 4} \tag{1.40}$$

$$\bar{\eta}_{a\mu\nu} = \epsilon_{a\mu\nu} - \delta_{a\mu}\delta_{\nu 4} + \delta_{a\nu}\delta_{\nu 4} \tag{1.41}$$

For the instanton the topological charge density is given by

$$Q(x) = \frac{6}{\pi^2}\frac{\rho^4}{(x^2 + \rho^2)^4} \tag{1.42}$$

ρ is called the width of the instanton; it is the radius of the region that contains half the topological charge of the instanton. The anti-instanton solution is the spatial parity transform of the instanton solution. There are 8 degrees of freedom of the instanton solution in $SU(2)$; 3 gauge degrees of freedom, the size ρ and the position of the centre of the instanton, x_0.

Classically QCD is scale-invariant hence ρ is a degree of freedom (in contrast to

the 1-d case described earlier where the instantons were a fixed size). Small ρ implies a short tunnelling time and large field strengths, large ρ the opposite.

These are the only solutions with $Q = 1$ in 4-d with gauge group $SU(2)$. $SU(3)$ is parameterised by 8 angles (the gauge functions are not a mapping of $S^3 \to S^3$) hence there are no $SU(3)$ instanton solutions in 4 dimensions, however the $SU(2)$ solutions can be embedded into an $SU(2)$ subgroup of $SU(3)$ and these are the ones that appear in QCD. In $SU(3)$ there are 12 degrees of freedom for the $SU(2)$ instanton solutions; 1 from the width, 4 from the position of the instanton and 7 gauge degrees of freedom. One of the generators of $SU(3)$ leaves the instanton solution invariant.

The solutions with $Q = 1$ are the most important topologically non-trivial solutions. The contribution to observables from solutions of higher winding number is exponentially suppressed relative to the contribution from the instanton solutions.

1.4 Physical Interpretation

Instantons correspond to tunnelling processes in Minkowski Space. This tunnelling indicates a rich vacuum structure of the gauge theory vacuum . Consider pure gauge theory in Minkowski space and with the gauge fixed to Weyl gauge, $A_0 = 0$. Vacuum states are those with zero field strength; this implies that

$$A_i = U(\vec{x})\partial_i U^\dagger(\vec{x}) \tag{1.43}$$

An argument by Callan et al [6] shows that the only functions that need to be considered are those with $U(\vec{x}) \to 1$ as $x \to \infty$.

Originally $U(\vec{x})$ mapped $R^3 \to S^3$ if the gauge group is $SU(2)$. However the restriction $U(\vec{x}) \to 1$ means that all points x at infinity are identified with each other so the mapping becomes $S^3 \to S^3$ and will fall into homotopy classes. The

generic function with $Q = 1$ is

$$g_1(\vec{x}) = \exp\left[i\pi \frac{\vec{x}.\vec{\tau}}{(x^2 + a^2)^{\frac{1}{2}}}\right] \tag{1.44}$$

and for $Q = n$

$$g_n = (g_1)^n \tag{1.45}$$

Hence there are an infinite number of topologically distinct vacua, called n-vacua and denoted $|n\rangle$.

An argument by Rebbi[7] shows that there is an energy barrier between the n-vacua. Consider the class of field configurations

$$A_i^\beta = \beta A_i^1(x) \tag{1.46}$$

where β is a real parameter $0 \leq \beta \leq 1$ and $A_i^1(x)$ is the pure gauge classical vacuum with $n = 1$. For $\beta = 0$ and $\beta = 1$, A_i^β is pure gauge, but for $0 < \beta < 1$ A_i^β is not a pure gauge. The chromo-electric field F^{0i} vanishes since $\dot{A}_0^\beta = 0$ and A_i^β is time independent. But the chromo-magnetic field $B_i = \frac{1}{2}\epsilon_{ijk}F^{jk}$ will not vanish. It can be shown that

$$F_{jk} = (\beta^2 - \beta)[A_j^{(1)}, A_k^{(1)}] \tag{1.47}$$

which is not equal to 0. The energy of the system is proportional to $\int tr(F_{jk}F_{jk})d^3x$ and is therefore non zero for $0 < \beta < 1$. Varying β from $0 \to 1$ connects the $n = 0$ to the $n = 1$ vacuum but there is a finite energy barrier between the 2 sectors. In the quantum theory there will be tunneling through the energy barrier and the true vacuum will be a superposition of all the $n-$vacua.

Consider a gauge transform U with unit winding number 1. Applying U to $|n\rangle$ gives

$$|n\rangle \xrightarrow{U} |n+1\rangle \tag{1.48}$$

Gauge invariance of the Hamiltonian implies

$$[U, H] = 0 \tag{1.49}$$

hence the true vacuum of QCD must be an eigenstate of U[6][8] Its functional form is

$$|\text{vac}\rangle = \sum_n e^{in\theta}|n\rangle \tag{1.50}$$

where θ is a real number. These are called the θ vacua. The effect of U on this vacuum is

$$U|\text{vac}\rangle = e^{-i\theta}|\text{vac}\rangle \tag{1.51}$$

showing that the vacuum is an eigenstate of U [6][8].

In Euclidean space the classical path describing the tunneling from $|0\rangle \rightarrow |1\rangle$ is the instanton. The instanton solution has zero energy (the Euclidean Stress Tensor vanishes) and can be transformed so that $g = 1$ at $t = -\infty$ and $g = g_1$ at $t = \infty$.

The tunnelling between the $|n\rangle$ vacua in QCD gives rise to the parameter θ and adds a new (CP violating) term to the Lagrangian

$$\mathcal{L}_\theta = i\theta \frac{1}{32\pi^2} F\tilde{F} \tag{1.52}$$

In the pure gauge theory, if the instantons are sufficiently dilute then the vacuum energy density is given by

$$\frac{E(\theta)}{V} = -2K\cos(\theta)e^{-S_{inst}} \tag{1.53}$$

where K is a factor related to the determinant of the fluctuations of the gauge-field about the background of a single instanton (more about this will be said later).

1.5 Instantons and Fermions

Fermions are also affected by the existence of instantons. In particular instantons lead to the solution of the $U(1)$ problem. Consider QCD with 3 flavours of massless fermion. The QCD Lagrangian is invariant under chiral rotations of the fermion fields.

$$\psi_{Lf} \to U_L \psi_{Lf} \tag{1.54}$$

$$\psi_{Rf} \to U_R \psi_{Rf} \tag{1.55}$$

where $U_{L(R)} \in SU(3)$. If the quarks are massless then there is also an axial $U(1)$ symmetry

$$\psi_f \to e^{i\alpha\gamma_5}\psi_f \tag{1.56}$$

where $\alpha \in \mathcal{R}$. If the $U(1)$ symmetry wer manifest then all hadrons would come in parity pairs[9][10]. If the symmetry were spontaneously broken, as chiral symmetry is believed to be, then there would be a ninth Goldstone boson with a mass comparable to the π. In nature particles don't come in parity pairs and the candidate Goldstone boson, the η', is far too heavy. This is the $U(1)$ problem.

The problem is solved by the existence of instantons. Consider QCD with one massless fermion flavour. The instanton solutions are again the centre points for a semi-classical expansion of the path-integral. In particular the θ vacua remain. Including the fermion fields only alters the factor K in equation 1.53 by including a factor $\det(\not{D})$. The $U(1)$ problem is resolved by the observation that the axial current contains an anomaly

$$\partial_\mu j^5_\mu = \frac{N_c}{16\pi^2} F_{\mu\nu}\tilde{F}_{\mu\nu} \tag{1.57}$$

where

$$j^5_\mu = \bar{\psi}\gamma_\mu\gamma_5\psi \tag{1.58}$$

Define the axial charge Q_5 as

$$Q_5 = \int d^3x j_0^5 \tag{1.59}$$

Consider

$$\Delta Q_5 = Q_5(t = \infty) - Q_5(t = -\infty) = \int d^4x \partial_\mu j_\mu^5 \tag{1.60}$$

on a single gauge configuration. On integration over the fermion fields ΔQ_5 is given by

$$\Delta Q_5 = \int d^4x N_f \partial_\mu \mathrm{tr}(S(x,x)\gamma_\mu\gamma_5) \tag{1.61}$$

where $S(x,y)$ is the fermion propagator. On any given configuration the fermion propagator can be written in terms of the eigenfunctions ψ_λ of $\not{D}$

$$S(x,y) = \sum_\lambda \frac{\psi_\lambda(x)\psi_\lambda^\dagger(y)}{\lambda} \tag{1.62}$$

If $\not{D}\psi = \lambda\psi$ with $\lambda \neq 0$ then $\gamma_5\psi$ is an eigenmode $\not{D}$ with eigenvalue $-\lambda$ i.e. all non-zero modes come in pairs. If $\lambda \neq 0$ then the chirality of the mode, $\chi = \langle\psi^\dagger\gamma_5\psi\rangle$, is equal to zero. Zero modes have no partner and have $\chi = 1$. Hence only zero modes contribute to equation 1.61 so

$$\Delta Q_5 = 2N_f(n_+ - n_-) \tag{1.63}$$

where $n_{+(-)}$ is the number of right(left)-handed zero modes of $\not{D}$. In the instanton field the Dirac operator has a single zero mode and

$$\Delta Q_5 = 2N_f \tag{1.64}$$

Hence in the background of a single instanton the $U(1)$ current is not conserved. Instantons break the $U(1)$ symmetry.

In general the number of zero modes of the Dirac operator satisfies

$$Q = N_f(n_+ - n_-) \tag{1.65}$$

where Q is the topological charge of the configuration, and $n_{+(-)}$ is the number of right(left) handed zero modes of $\not{D}$. This is the Atiyah-Singer Theorem [11][12]. For a single instanton $n_+ = 1$ and $n_- = 0$ while for an anti-instanton $n_+ = 0$ and $n_- = 1$.

Recall that in the pure gauge theory the vacuum energy density depended non-trivially on θ. A single massless fermion flavour includes a factor $\det \not{D}$ in the factor K that appears in the energy density of the vacuum and the fermion zero mode now renders all θ vacua degenerate.

Witten[13] investigated the solution of the $U(1)$ problem in the large N limit. In this limit the leading contribution to the vacuum energy from quark loops is suppressed by a factor of $\frac{1}{N}$ relative to the leading contribution from gluon loops [14]. Now suppose that the leading contribution from quark loops to the θ dependence of the vacuum energy is also suppressed in the same way. The addition of quark loops renders the θ-vacua degenerate but how can this contribution whose leading order is suppressed by a factor $\frac{1}{N}$ cancel out the θ dependence?. This was answered by postulating the existence of a pseudoscalar particle with mass $\propto \frac{1}{N}$. At $N = \infty$ the $U(1)$ current is conserved (the anomaly is suppressed by a factor $\frac{1}{N}$) and there is a massless goldstone boson, the η'. At finite N the $U(1)$ symmetry is broken and the η' becomes massive through its interaction with the anomaly. It has been shown that in this picture the mass of η' is given by the following relation

$$\chi_t = \frac{1}{V}\left\langle \left(\int Q(x) d^4x \right)^2 \right\rangle = 2f_\pi(m_\eta^2 + m_{\eta'}^2 - 2m_K^2) \tag{1.66}$$

χ_t is called the topological susceptibility. It is calculated in the theory with *no* quarks i.e the quenched theory whereas the rhs is calculated in the full theory. For this mechanism to explain phenomonology

$$\chi_t \approx (180\text{MeV})^4 \tag{1.67}$$

θ is a free parameter in the standard model. Experimental bounds on θ from measurements of the neutron dipole moment make $\theta < 10^{-9}$[10]. The smallness of θ is the strong CP problem. One solution is a massless $u-$quark ; this makes all the θ vacua degenerate and CP would be conserved in all of them i.e. $\theta \equiv 0$. At the moment, however, it is not clear if the $u-$quark mass is zero and the strong CP problem is as yet unsolved.

1.6 Instanton phenomenology

In QCD the instanton width ρ is a free parameter and any calculation of a tunneling amplitude must integrate not only over the instanton position but ρ as well; for example the constant K in equation 1.53 will include contributions from all sizes.

For QCD the semi-classical tunnelling amplitude for a single instanton including quantum effects has been computed to one loop in [15], It was found that the contribution from instantons with sizes between ρ and $\rho + d\rho$ is given by

$$D(\rho)d\rho = \frac{d\rho}{\rho^5}\left(\frac{8\pi^2}{\bar{g}^2(1/\rho\mu)}\right)^{2N_c} \exp\left(-\frac{8\pi^2}{\bar{g}^2(1/\rho\mu)}\right) C(1 + O(\bar{g}^2(1/\rho\mu))) \quad (1.68)$$

where C is a numerical constant. In $SU(3)$

$$C = 0.1 \quad (1.69)$$

As $\rho \to 0$

$$\frac{8\pi^2}{\bar{g}^2(1/\rho\mu)} \overset{\rho\to 0}{\to} \left(\frac{11N_c}{3}\right) \ln\left(\frac{1}{\rho\mu}\right) \quad (1.70)$$

This gives the result for $SU(3)$

$$D(\rho) \propto \rho^6 \quad (1.71)$$

for small ρ. For large ρ the behaviour is unknown. One problem is the behaviour of the coupling; as ρ increases $\bar{g}^2\rho$ increases and the one-loop formula is no longer valid (the one loop formula diverges for large ρ).

If a true model of the vacuum is to be constructed, the behaviour of large instantons must be included. If instantons are large and their separation is small then the dilute gas approximation is invalid; the treatment of instantons as well separated non-interacting objects is wrong and interactions must be taken into account. Calculations involving mixed instanton anti-instanton configurations are highly non-trivial. An instanton anti-instanton pair is not a solution of the equations of motion (it belongs to the $Q = 0$ sector but has action, $S > 0$) and only in the case where the instanton and anti-instanton are infinitely far apart will $S = 2S_{inst}$.

For large separation the interaction was derived by Callan et. al.[6]. It was found that for a well separated instanton anti-instanton pair the interaction is given by

$$S_{int} = \frac{32\pi^2}{g^2}\frac{\rho^2\bar{\rho}^2}{R^4}R_{ab}\bar{\eta}_{a\mu\alpha}\eta_{b\mu\beta}\hat{R}_\alpha\hat{R}_\beta \tag{1.72}$$

where R_{ab} is the matrix describing the relative orientation of the instanton and the anti-instanton and $\hat{R}$ is the unit vector from the instanton to the anti-instanton.

For smaller separations the fields will be severely distorted and the interaction is hard to define. Various ansätze have been put forward [16][17]. In all the ansätze the interaction depends on the orientation of the objects; the interaction can either be attractive ($S_{pair} < 2S_{inst}$) or repulsive ($S_{pair} > 2S_{inst}$). The probability of finding a pair with a particular orientation and separation will depend on the action of the configuration and it is expected that instantons will be screened by anti-instantons because this will lower the action of the pair and hence increase $\exp(-S_{pair})$.

Models of the vacuum have been put forward such as the Interacting Instanton Liquid Model [18]. In this model the contribution of large instantons is exponentially suppressed by a factor $\exp\left(-\nu\frac{\rho^2}{\bar{\rho}^2}\right)$ where $\nu = 7$ in $SU(3)$ and $\bar{\rho}$ is the average size of the instanton; this weighting renders the integral over ρ finite allowing calculations to carried out.

A first principles calculation of the properties of the instanton vacuum is a non-

perturbative problem. One of the best tools for doing non-perturbative calculations of QCD is Lattice Gauge Theory. However when dealing with topology there are many technical difficulties to be overcome. These are reviewed in the next chapter.

Chapter 2

Lattice Gauge Theory and Cooling

2.1 Lattice Gauge Theory

To carry out a numerical simulation of QCD, the number of degrees of freedom must be made finite. Space time is discretised on a finite Euclidean lattice; $\int dx$ is replaced with $a\sum_x$ where a is the lattice spacing.

The gauge fields are represent by link fields $U_\mu(x)$ which belong to the gauge group $SU(3)$ unlike the continuum gauge fields A_μ which belong to the Lie Algebra of $SU(3)$.

The link field $U_\mu(x)$ is the parallel transporter from the point x to the point $x + a\hat{x}_\mu$ where $\hat{x}_\mu$ is the unit vector in the μ direction.

$$U_\mu(x) = P \exp\left[\int_x^{x+a\hat{x}_\mu} dz_\mu A_\mu(z)\right] \tag{2.1}$$

In the continuum limit the link variables become

$$U_\mu(x) = 1 - aA_\mu(x + \frac{1}{2}a\hat{x}_\mu) \tag{2.2}$$

Parallel transport from $x + a\hat{x}_\mu$ to x is given by $U_\mu^\dagger(x)$. The continuum functional integral $\int \mathcal{D}A_\mu$ is replaced by $\Pi_{x,\mu} \int \mathcal{D}U$. The gauge transformation properties of the U's are the same as those of path ordered integrals in the continuum

$$U_\mu(x) \to V^\dagger(x) U_\mu(x) V(x + a\hat{x}_\mu) \tag{2.3}$$

A lattice version of the pure gauge action can be constructed using the smallest closed loop on the lattice, the plaquette.

$$P_{\mu\nu}(x) = U_\mu(x)U_\nu(x + a\hat{x}_\mu)U_\mu^\dagger(x + a\hat{x}_\nu)U_\nu^\dagger(x) \tag{2.4}$$

For small a it can be shown that

$$\mathrm{Re}tr P_{\mu\nu} = 3 - \frac{g^2}{2}a^4\mathrm{Tr}(F_{\mu\nu}F_{\mu\nu}) + O(a^6) \tag{2.5}$$

The "Wilson (gauge) action" is then given by

$$S_g = \beta \sum_x \sum_{\mu>\nu>0} 1 - \frac{\mathrm{Re}\mathrm{Tr}P_{\mu\nu}(x)}{3} \tag{2.6}$$

β is defined as $\beta = \frac{6}{g^2}$ (for $SU(N)$ gauge theories $\beta = \frac{2N}{g^2}$).

The path integral is now amenable to numerical simulation. The integral is carried out using Monte Carlo methods. A dataset of N gauge field configurations $\{U_i\}_{i=1..N}$ is generated with "importance sampling" so that only those configurations which contribute most to the path-integral are chosen. In particular, choosing the configurations with probability density $P \propto e^{-S_g}$, an estimator for the expectation value of any quantity $\mathcal{O}$ (such as the instanton size distribution) is given by

$$\langle \mathcal{O} \rangle = \frac{1}{N}\sum_i \mathcal{O}(U_i) \tag{2.7}$$

where $\mathcal{O}(U_i)$ is the quantity calculated on the gauge configuration U_i. The configurations analysed in chapters 3 and 4 of this thesis were generated using a hybrid over-relaxed algorithm.

2.2 Topological Charge and Instantons on the Lattice

The topology of gauge fields is trivial on a lattice. This can be seen as follows. A topological fluctuation e.g. an instanton must have a core, of non-zero topological charge density, and can be characterised by the size, ρ of this core. In the

continuum the instanton size, ρ can be chosen to be any value and $Q = 1, \forall\rho$. Consider an instanton discretised on a lattice with $\rho >> a$. Integrating $F\tilde{F}$ over the lattice will give $Q = 1$. However if ρ is made small enough the core of the instanton will fall between the lattice sites and integrating $F\tilde{F}$ over the lattice gives $Q = 0$. The deformation described above is a smooth deformation; the transition from $Q = 1$ to $Q = 0$ is a smooth one. All that is left is a gauge singularity at the centre of the instanton along with a necessary gauge singularity of opposite winding number elsewhere [19]; the core of the instanton has disappeared from the lattice. This is an example of a general result that all lattice gauge fields are continuously deformable into each other. Although there is no topology on the lattice, if QCD has a continuum limit then as $a \to 0$, the physical continuum topological properties should be recovered e.g. the continuum instanton distributions.

The introduction of a lattice breaks the scale invariance of the theory and the action of an instanton will now depend on ρ. For $\rho >> a$, the corrections to the instanton action should be negligible and

$$S_I^{\text{lattice}} \approx S_I^{\text{cont}} \tag{2.8}$$

However if ρ decreases down to $\rho \sim a$ then

$$S_I^{\text{lattice}} \ll S_I^{\text{cont}} \tag{2.9}$$

This suggests a strong relative enhancement of instantons on the size scale of the ultraviolet cut-off. Indeed an argument by Pugh and Teper [19] shows that if lattice instantons can be constructed (in $SU(3)$) with action

$$S_I^{\text{lattice}} < \frac{8\pi^2}{11} \tag{2.10}$$

then the instanton size distribution, $D(\rho)$, and χ_t will diverge in the continuum limit. Lattice artefacts should decouple from the long-distance physics and so these small instantons should not be included in a calculation of χ_t and any

measurement of the instanton content of the vacuum.

The topological charge of each configuration is calculated by integrating the topological charge density $Q(x)$ over the whole lattice. A discretisation of the topological charge density can be constructed

$$Q(x) \equiv \frac{1}{32\pi^2}\epsilon_{\mu\nu\rho\sigma}\mathrm{Retr}P_{\mu\nu}(x)P_{\rho\sigma}(x) \tag{2.11}$$

The analysis carried out in chapters 3 and 4 uses the symmetrised form of the charge where the sum is over both the forward and backward directions. This operator has the correct *naive* continuum limit, however the operator undergoes a renormalisation

$$\langle Q_{\mathrm{latt}}(x)\rangle = Z(\beta)\langle Q_{\mathrm{cont}}\rangle \tag{2.12}$$

$Z(\beta)$ has been computed to 1 loop in reference [20] where for $SU(3)$ it was found that

$$Z(\beta) = 1 - \frac{5.451}{\beta} + O\left(\frac{1}{\beta^2}\right) \tag{2.13}$$

The relation of the lattice value of the topological susceptibility to the continuum value is complicated by an unphysical background term which becomes dominant in the continuum limit. χ_t on the lattice is given by [21]

$$\chi_{t(\mathrm{latt})}(g_0^2) = a^4 Z^2(g_0^2)\chi_t + M(g_0^2) \tag{2.14}$$

Any calculation of topological properties on the lattice will be dominated by lattice artifacts. One method used to resolve these problems is to use an improved lattice topological charge density operator [21][22][23] so that $Z(\beta)$ is closer to 1 and whose corresponding $\chi_{t(\mathrm{latt})}$ is not dominated by the background term. The method employed in this thesis is to remove the lattice artifacts by the technique known as cooling.

2.3 Cooling

The cooling method was invented to determine the topological susceptibility on the lattice in a way that was not plagued by contributions from localised lattice artefacts [24].

The problem of applying the discretised topological charge density (equation 2.11) is the presence of ultraviolet fluctuations. For small enough lattice spacing these fluctuations will take place on length scales much smaller than the length scales of physical interest. Therefore if the gauge field configuration was to be **locally** smoothed then the ultraviolet modes would be removed while the physical, long distance, topological modes would remain undisturbed. Since locally minimsing the action of a continuum gauge field does not change the topological charge of that field, the same should be true for lattice fields up to effects at the scale of the cut-off.

Cooling works as follows. The fluctuations around a link $U_\mu(x)$ are measured by the local piece of the action that involves $U_\mu(x)$ and its nearest neighbours. If the link $U_\mu(x)$ is replaced by a link $U'_\mu(x)$ such that the action is reduced, then the local variations are reduced and the field has been locally smoothed.

In $SU(2)$ choosing

$$U'_\mu(x) = \frac{\Sigma^\dagger}{|\Sigma|} \tag{2.15}$$

where Σ is the sum of all the staples around the link under consideration will locally minimise the action.

In $SU(3)$ this does not work because $\frac{\Sigma^\dagger}{|\Sigma|}$ is not an $SU(3)$ matrix. The method applied in this thesis (and earlier works [24]) is to update the link matrix by multiplying it by a matrix, V, from an $SU(2)$ subgroup.

$$U_{\mu(x)} \rightarrow V U_{\mu(x)} \tag{2.16}$$

where V is chosen so that within this class of transformations the action is locally minimised. In this investigation the contribution of each link to the total action is

minimised over all 3 diagonal subgroups and the cooling step employs a red-black update. The method described here is the $\beta \to \infty$ limit of the Cabibbo-Marinari Monte-Carlo updating scheme. Carrying out this proceedure for all links on the lattice is called a *cooling sweep.*

2.4 The effect of cooling on thermalised configurations

Cooling raises the "effective β value" of the configuration; the plaquette value becomes closer to 1. After a few cooling sweeps all the ultraviolet fluctuations will have been removed and what will be left is a semi-classical configuration; all that remains are long range topological excitations. On a configuration after a few cooling sweeps $Z(\beta_{eff}) = 1$ and the unphysical background term that dominates the susceptibility goes to zero. The topological charge of the configuration is then measured using equation 2.11.

The cooling curves (S vs cooling sweep and Q vs cooling sweep) for a typical configuration are shown in figures 2.1 and 2.2. During the first few cooling sweeps the action drops rapidly, and after many cooling sweeps the action has almost plateaued (the decrease in action after many sweeps is very small). The topological charge of the configuration has settled down to a near plateau after 10 cooling sweeps. After 10 sweeps the topological charge of this configuration is identifiable as $Q = 3$. The variation in Q with sweeps is a result of a small anti-instanton broadening out presumably as a result of the artificial dynamics induced by the cooling and then shrinking and disappearing; the disappearance of the anti-instanton occurs after 38 sweeps where there is a sudden jump in Q to $Q = 4$. What happens during the first few cooling sweeps is unclear although, because cooling is a local procedure it should only produce local changes in the configuration. This argument is purely heuristic. However, it has been checked in both $SU(2)$ and $SU(3)$ by both cooling close together Monte-Carlo configurations and by cooling the same gauge field configuration in a number of different ways by altering the order in which the cooling algorithm visits the links.

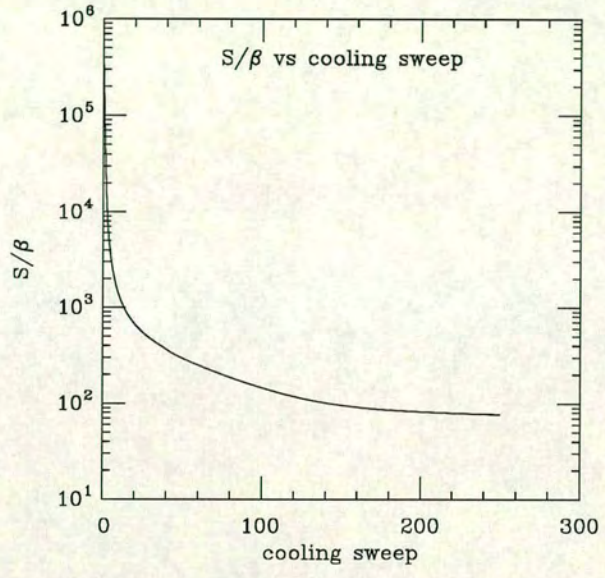

Figure 2.1: S/β vs cooling sweep

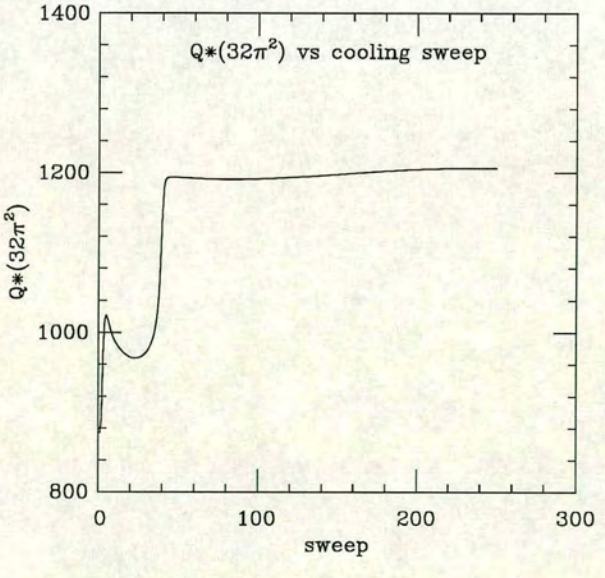

Figure 2.2: $Q \times (32\pi^2)$ vs cooling sweep

2.5 The effect of cooling on Instantons

In the continuum an instanton is scale invariant and is already a minimum action solution so ideally on the lattice cooling would not affect a single instanton. However, the lattice breaks the scale invariance of the theory and the action (charge) of an instanton as measured by summing up the action(charge) density will depend on the size of the instanton. An expansion can be made in powers of $\frac{1}{\rho}$ and in general

$$S(\rho) = 1 + c\frac{a^2}{\rho^2} + O\left(\frac{a^4}{\rho^4}\right) \tag{2.17}$$

$$Q(\rho) = 1 + b\frac{a^2}{\rho^2} + O\left(\frac{a^4}{\rho^4}\right) \tag{2.18}$$

Using the discretisation of the topological charge operator, equation 2.11 means that the topological charge of the configuration is now non-integer. In the calculation of the susceptibility described in chapter 4, the discretisation effects of the topological charge of an instanton are corrected for.

For the Wilson action $c < 0$ and so cooling will cause individual instantons to shrink (the lower ρ is, the smaller the action). Eventually the instanton will shrink out of the lattice and the topological charge of the configuration will go to zero. Very small instantons are unstable under cooling and they will disappear from the lattice very quickly. However, large (physical) instantons are stable under cooling and take many cooling sweeps to remove from the lattice [25]. One way to avoid the problem with small instantons is to cool by minimising an improved action as used by de Forcrand et. al. [26]. With this method the gauge action is improved so that instanton solutions are made scale invariant up to $O\left(\frac{a^6}{\rho^6}\right)$ by adding larger Wilson loops to the action. This has the effect of making the instantons much more stable under cooling.

A second problem with cooling is the problem of instanton anti-instanton annihilations. An instanton anti-instanton pair is not a solution of the equations of motion; it belongs to the $Q = 0$ sector of QCD but has $S > 0$, whereas the

minimum action configuration for $Q = 0$ has $S = 0$. Minimising the action of this configuration will move the configuration towards the unit gauge. The instanton and anti-instanton will move closer together and *annihilate* with each other. This process will reduce the action and will not change the topological charge of the configuration. Thus cooling introduces its own dynamics into the system and will change the system as more and more cooling is carried out, therefore it is necessary to do as few cooling sweeps as possible in order to try and reduce this problem.

The behaviour of a configuration under cooling can loosely be divided into 3 distinct stages. The first stage is the erasing of the ultra-violet modes of the configuration leaving behind long distance modes. The second stage is the annihilation of instantons with nearby anti-instantons. After this stage what will be left are large isolated instantons and anti-instantons which will be nearly stable under further cooling.

2.6 Under-relaxed Cooling

Under-relaxed cooling [27] was used in [28] to study the instanton content of the $O(3)$ vacuum and in [29] to study the instanton content of the $SU(2)$ vacuum. In $SU(2)$ the under-relaxed cooling step is

$$U'_{x,\mu} = c(\alpha U_{x,\mu} + \Sigma^{\dagger}_{x,\mu}) \tag{2.19}$$

where α controls the amount of under relaxation and c is a constant to normalise the new matrix to be in $SU(2)$.

Under-relaxed cooling is implemented in $SU(3)$ by changing the Cabibbo Marinari cooling update to

$$U'_{x,\mu} = c(\alpha + u^{\dagger})U_{x,\mu} \tag{2.20}$$

where again c normalises the matrices so that they remain in $SU(3)$, α controls the under-relaxation and $u^{\dagger}$ is the $SU(2)$ transformation that locally minimises the action. In this section the effect of under-relaxed cooling is investigated on

α	sweeps
0	23
0.5	38
1.0	54
1.5	71
2.0	88
2.5	105
3.0	122
4.0	156
6.0	222

Table 2.1: No of sweeps to remove a $\rho = 2$ instanton

instanton anti-instanton pairs and on thermalised configurations.

The number of under-relaxed cooling sweeps at different values of α cannot be compared directly, so to investigate the effect of under-relaxed cooling on, for example, instanton anti-instanton pairs it is first necessary to calibrate the cooling sweeps. In this study, as in [27], the calibration scale is set by measuring the number of sweeps it takes to remove an instanton of size $\rho = 2$; this is defined to be one calibrated sweep. For the $O(3)$ model it was found that for $\alpha \geq 2$ the final topological charge distributions became independent of α after one calibrated cooling sweep[27].

The instanton is set up on a 16^4 lattice using the discretisation of the continuum solution of Pugh[19][30]. The instanton is then cooled until $S/S_I < 0.1$. The number of sweeps taken to remove the instanton at each value of α is given in table 2.1 and plotted in Figure 2.3. The plot shows that the number of sweeps to destroy a single instanton is linear in α, however I am unable to offer an explanation for this behaviour.

Now that the calibrated sweep has been defined a comparison of different α values is made by comparing the number of calibrated sweeps. The number of calibrated sweeps is defined as $\frac{\#\text{sweeps}}{m(\alpha)}$, where $m(\alpha)$ is the number of cooling sweeps taken

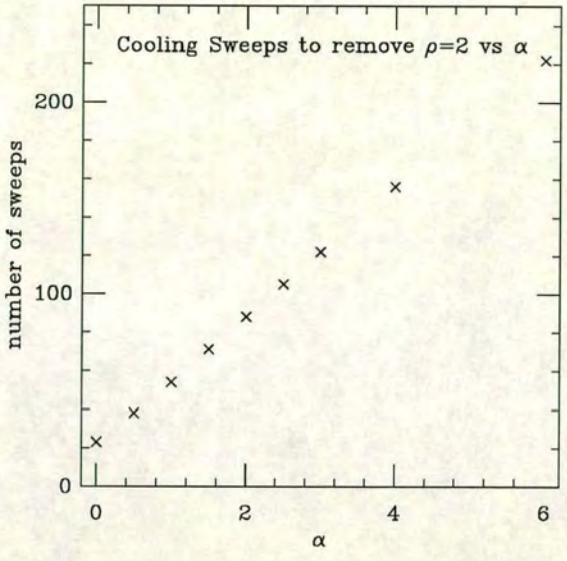

Figure 2.3: No of sweeps to annihilate a $\rho = 2$ instanton

to remove a $\rho = 2$ at this α value. In all the following plots in this chapter the x-axis scale is given in terms of calibrated sweeps.

2.6.1 Instanton anti-instanton pairs

The first investigation of the effects of under-relaxed cooling was on instanton anti-instanton pairs. The aim here is to see if using under-relaxation increases the number of *calibrated* cooling sweeps it takes to annihilate an instanton anti-instanton pair. Well-separated instantons were set up on a $16^3 \times 48$ lattice. On many of the configurations e.g. 2 instantons with $\rho = 2$ a distance 6 apart, the instantons didn't annihilate (they disappeared separately under cooling) however the examples below clearly demonstrate the effect of under-relaxation.

The first example is an instanton and an anti-instanton both of size $\rho = 3$ set up a distance 10 apart. The configuration was cooled and the pair annihilated. The action of the configuration is plotted in Figure 2.4 for different values of α. As α is increased the number of calibrated sweeps taken to annihilate the pair increases. Further information can be gained by examining the peak height (the local max-

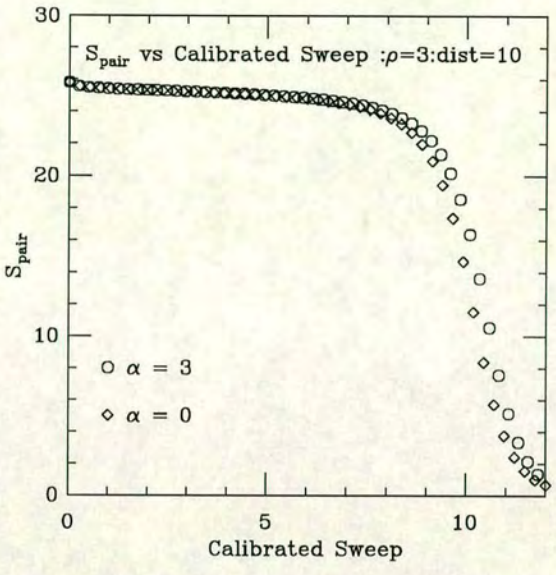

Figure 2.4: Action vs Calibrated Sweep

ima in the topological charge density), denoted by Q_{peak}, of the instantons. An isolated instanton will shrink under cooling and Q_{peak} will increase, while during annihilation Q_{peak} decreases. Another check of the effect of under-relaxed cooling is to look at the number of calibrated sweeps it takes for the peak height of, say, the instanton to start decreasing. This is plotted for the instanton in figure 2.5 and shows that as α is increased the number of sweeps increases but for $\alpha \geq 1$ the variation is much less.

The second example is an instanton and an anti-instanton both of size $\rho = 3$ set up a distance 9 apart. The action of the configuration is plotted in figure 2.6. Again it can be seen that increasing α increases the number of calibrated sweeps it takes for the pair to annihilate.

The effects here are quite small, however, the conclusion from these examples is that under-relaxed cooling slows down the annihilations of instanton anti-instanton pairs.

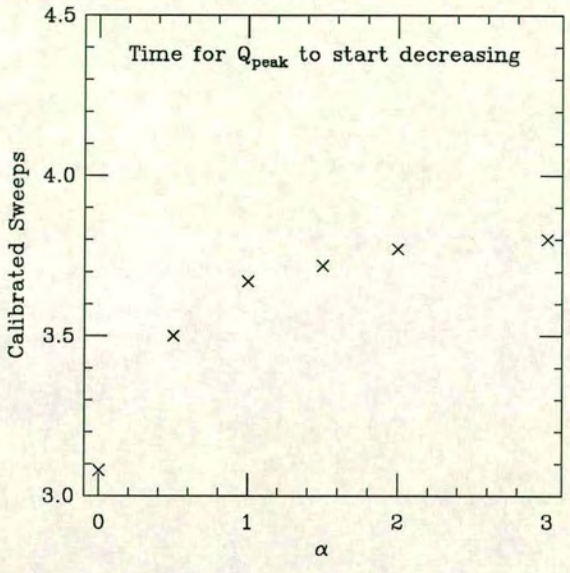

Figure 2.5: No of calibrated sweeps for Q_{peak} to start decreasing

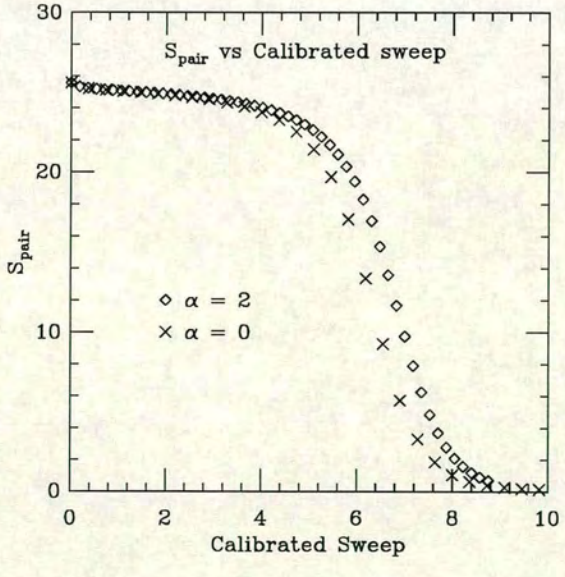

Figure 2.6: Action vs Calibrated sweep

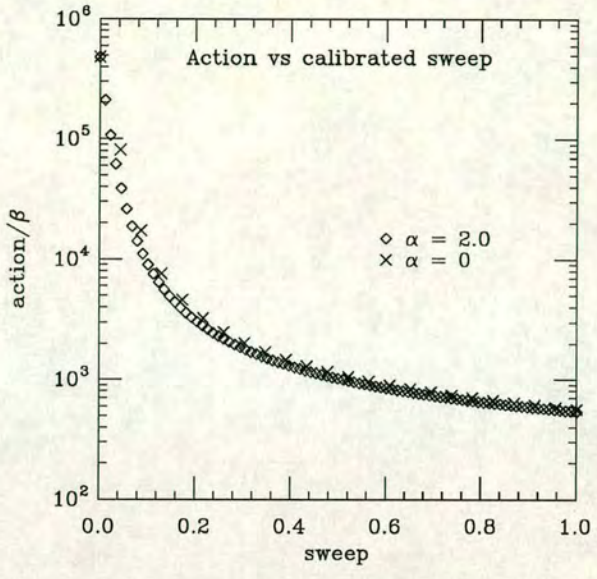

Figure 2.7: Action vs Calibrated sweep

2.6.2 Under-relaxed cooling on thermalised configurations

In this section the effect of under-relaxed cooling on thermalised configurations is studied. Five $\beta = 6.0$ $16^3 \times 48$ lattices were cooled using different levels of under-relaxation ($\alpha = 0.0, 0.5, 1.0, 1.5, 2.0, 2.5, 3.0$) and the cooling curves of the configurations were examined.

The calibrated sweep defined above can also be used on thermalised configurations. Figure 2.7 shows how the action varies with the calibrated cooling sweep. On the thermalised configurations the effect on the action of the configuration by a calibrated cooling sweep is almost independent of α; for $\alpha = 0$ after one calibrated sweep $\frac{S}{S_{init}} = 0.00117$ while for $\alpha = 2$ $\frac{S}{S_{init}} = 0.00112$. This shows that the equivalent calibrated sweep could have been defined by examining the action of the configuration during cooling.

The first observation of under-relaxed cooling is that it is a gentler cooling than full cooling. In full cooling the first cooling sweep generally causes a large jump in the topological charge of the configuration while using under-relaxed cooling

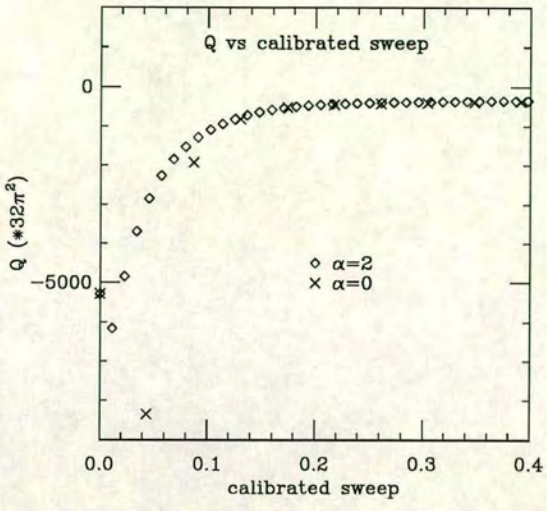

Figure 2.8: Q vs Calibrated sweep

gives a far smoother approach to the final value of Q as shown in figure 2.8.

On three of the configurations there was little variation of the cooling curve with α and the final topological charge did not vary. An example of this is shown in figure 2.9.

On the other two configurations the final value of Q did vary with α. These results are shown in figures 2.10 and 2.11.

In figure 2.10 there is a single narrow instanton that at $\alpha = 0$ broadens out whereas for $\alpha \neq 0$ the instanton disappears. Figure 2.11 shows a case where there are two narrow instantons that broaden out when $\alpha = 0$ and which disappear when $\alpha \geq 0.5$. This broadening of the narrow instantons is a result of their interaction with their environment. They will also affect the environment and so their removal by the under-relaxed cooling algorithm means that they will not have as much of an effect on their environment as with $\alpha = 0$. Further for $\alpha \geq 1$ the cooling curves become, almost, independent of α as shown in figures 2.10 and 2.11.

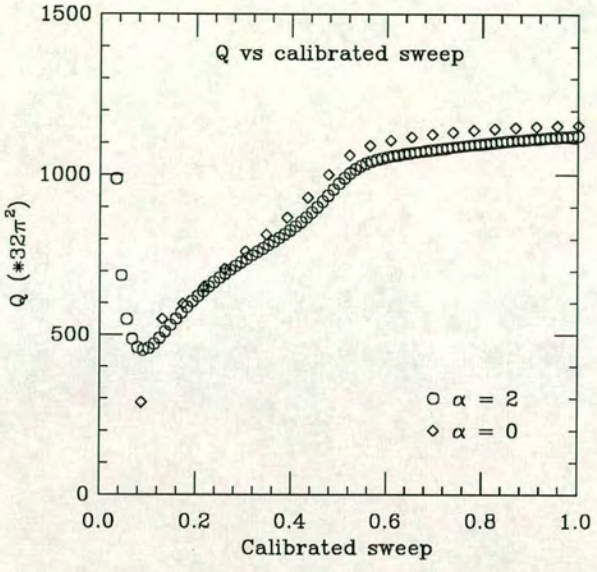

Figure 2.9: Q vs Calibrated sweep:no variation with α

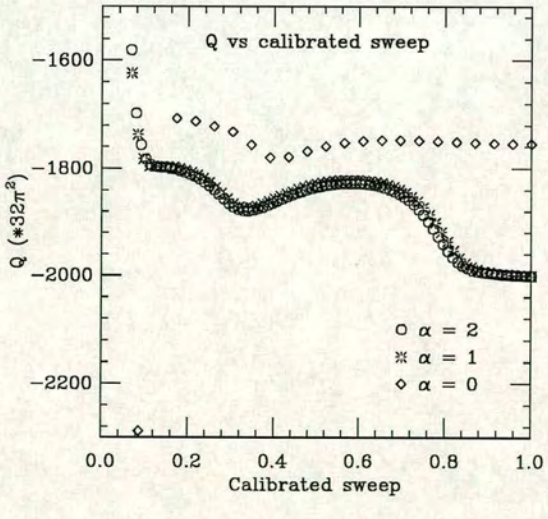

Figure 2.10: Q vs Calibrated sweep: variation with α

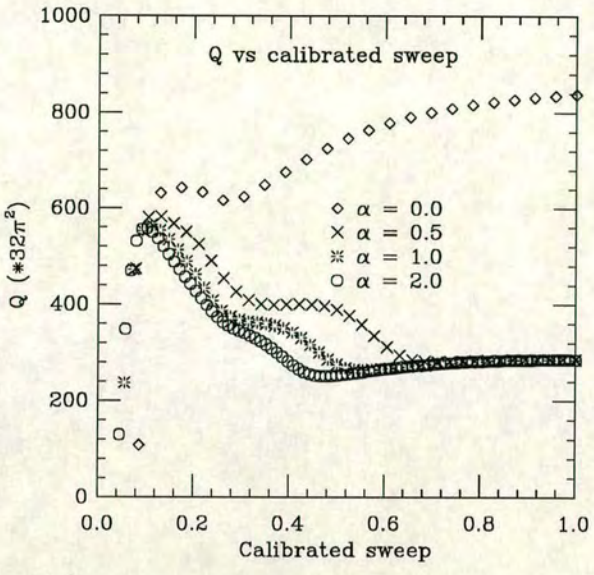

Figure 2.11: Q vs Calibrated sweep: variation with α

This is consistent with the results from the instanton anti-instanton pairs above where the number of calibrated sweeps to annihilate the pair increased with α. In the thermalised cases the annihilation of the narrow instanton with other anti-instantons does not happen fast enough to stop the narrow instanton disappearing under cooling.

The conclusion drawn from this study is that under-relaxed cooling is a better cooling algorithm to use for the study of the vacuum than cooling because it has slower annihilations in terms of a *calibrated* cooling sweep and because it is better at removing very narrow, unphysical, instantons. Further, the independence of the cooling curves for $\alpha \geq 1$ suggests using $\alpha = 1$ in all vacuum studies as a trade-off between gentle cooling and CPU time. In the following chapters, the properties of the vacuum are measured between 23 and 46 cooling sweeps at $\alpha = 1$ corresponding to between 10 and 20 full cooling sweeps ($\alpha = 0$).

Chapter 3

Analysis of the Cooled Configurations

3.1 Introduction

After the configurations have been cooled there remains the problem of extracting the instanton distributions. Large instantons will overlap and will be distorted through their interactions with each other. Various groups have tackled this problem in different ways.

Chu et. al. [31] measured the size of the instanton by calculating the correlation function

$$f(x) = \sum_y Q(y)Q(x+y) \tag{3.1}$$

and compared it with a convolution of the analytic expression for the topological charge (equation 1.42). This was fitted to the lattice data for $f(x)$ using a single value of ρ taken to be the average size. Their size distribution was obtained by analysing connected regions of the lattice and extracting ρ from the size of the region; two points belonged to the same region if the product of $Q(x)$ at these points was greater than the square of some threshold parameter.

Michael et. al. [29] also examined connected regions of the topological charge and action densities. They found all the local extrema in the density and then examined them in decreasing order of height. They looked for the connected region of sites for which the density is not less than half that at the peak. This is then related to the size assuming the continuum instanton formula.

De Forcrand et. al. [26] first looked for local maxima (relative to the points nearest neighbours) in the electric and magnetic contributions to the action density.

They counted as one instanton, peaks that were separated by no more than one lattice spacing along each direction and had also did not include peaks below a certain height. Their size distribution was calculated using 5 different definitions of the instanton width.

3.2 A first look at the cooled configurations

A single (anti-) instanton in the continuum in infinite volume is self-dual;

$$S = \frac{8\pi^2}{g^2}|Q| : |Q| = 1 \tag{3.2}$$

however an instanton anti-instanton pair is not.

$$S = \frac{16\pi^2}{g^2} : Q = 0 \tag{3.3}$$

If the pair are very far apart i.e. $R >> \rho_1, \rho_2$ where R is the distance between the centres, then the fields will be locally self-dual or antiself-dual i.e.

$$F_{\mu\nu}(x) = \pm\tilde{F}_{\mu\nu}(x) \tag{3.4}$$

and

$$S = \frac{8\pi^2}{g^2}\sum_x |Q(x)| \tag{3.5}$$

Measuring $\frac{\sum_x S(x)}{\sum_x |Q(x)|}$ gives a crude measurement of how dilute the instantons are in the vacuum. This is plotted against cooling sweep for 10 configurations at $\beta = 6.0$ in figure 3.1 and is normalised so that if the configuration is locally (anti) self dual then $\frac{\sum_x S(x)}{\sum_x |Q(x)|} = 1$. This data shows that at the number of cooling sweeps considered the cooled configurations are far from being locally (anti)self-dual. If it were to be assumed that, at the sweeps considered, it is only instantons and anti-instantons that remain then this implies that instantons and anti-instantons will be close together and overlapping.

The first stage of the analysis of the instanton content of the cooled configurations is to find all the local maxima and minima of a cooled density. When finding

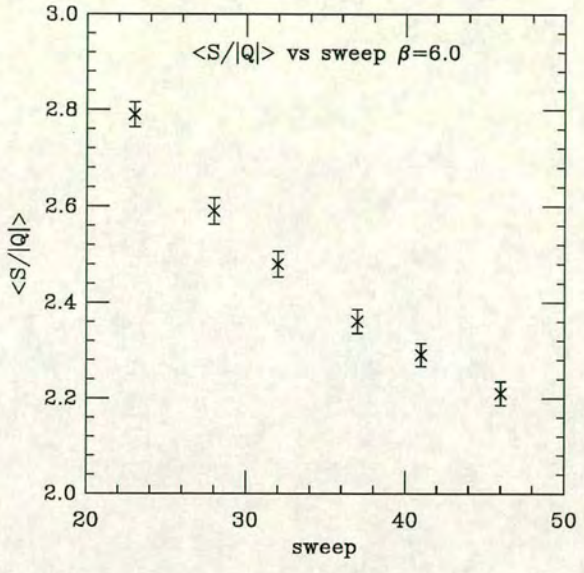

Figure 3.1: $\frac{\sum_x S(x)}{\sum_x |Q(x)|}$ vs cooling sweep

the local extrema, the density at the point under consideration is compared to densities on all the points in the surrounding 3^4 block; comparing the density at a point only to its nearest neighbours gives many spurious peaks e.g. on a single instanton during cooling, comparing only the nearest neighbours gives 3 close together peaks on the instanton while comparing with the 3^4 block gives only 1 peak.

3.3 Relation between peak height and width on the lattice

In the continuum the maximum topological charge density of an instanton is given by

$$Q_{\text{peak}} = \frac{6}{\pi^2 \rho^4} \tag{3.6}$$

however this formula does not hold on the lattice for small instantons. The relation between Q_{peak} and ρ was investigated on the lattice by cooling a single instanton on a 16^4 lattice. In the continuum the width of the instanton is the radius of the region, centered on the peak, that contains topological charge $\frac{1}{2}$. The width of the instanton on the lattice was measured by finding the minimum

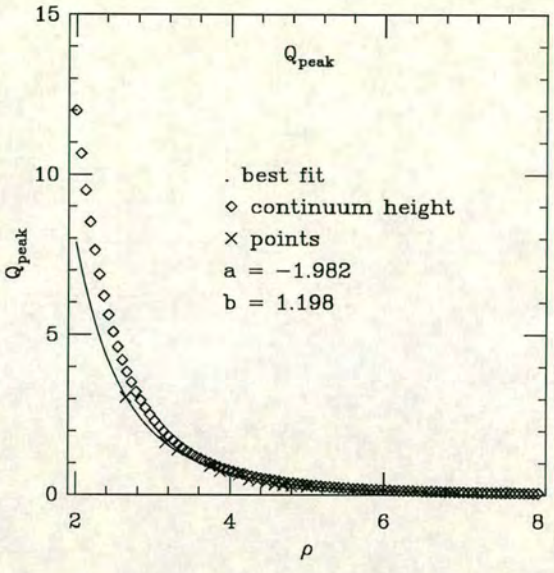

Figure 3.2: Q_{peak} vs ρ

radius around the peak that contained more than half the total charge on the lattice **not topological charge** $\frac{1}{2}$. There is an ambiguity here as a range of peak heights will be associated with the same width. The peak height that corresponds to that width is chosen to be the lowest one (which will correspond to the instanton with width closest to the radius). The data was fitted to the form

$$Q_{peak} = \frac{6}{\pi^2}\left(\frac{1}{\rho^4} + \frac{a}{\rho^6} + \frac{b}{\rho^7}\right) \tag{3.7}$$

(The leading order correction to the continuum formula is expected to be $\propto \frac{1}{\rho^6}$; the $\frac{1}{\rho^7}$ term is to represent all other corrections) and the best fit was $a = -1.962$ and $b = 1.198$. The data and best fit are plotted in figure 3.2 along with the continuum result.

3.4 Comparison of the action and charge

There are 2 densities that can be analysed to extract the instanton distributions; the cooled action density and the cooled charge density. On single instanton and very dilute configurations both will be equivalent, however, as shown above, the

sweep	#peaks $Q(x)$	#peaks $S(x)$
23	168	95
46	63	46

Table 3.1: No. of peaks in $Q(x)$ and $S(x)$

cooled configurations are not dilute so which density to analyse is an important question.

This was investigated on 5 $\beta = 6.0$ configurations after 23 and 46 cooling sweeps. The first observation is that the number of peaks of the charge density is much greater than the number of peaks of the action density although this discrepancy decreases as the number of cooling sweeps is increased as shown in table 3.1. Plotting the size distribution of the peaks obtained from using equation 3.7 (the same formula was used for the action but with the appropriate factor inserted), and binning the widths in bins of size 0.5, gives the size distributions shown in figures 3.3 and 3.4. $Q(x)$ clearly records more structure than $S(x)$ especially at larger values of ρ where $S(x)$ records no structure at all. At 23 sweeps $S(x)$ records no peaks with $\rho > 6$ while at 46 sweeps it records no peaks with $\rho > 7.5$. An explanation for this could be instanton anti-instanton pairs annihilating. A measurement of the charge would give 2 peaks, (one positive and one negative), however, because the action is always positive, it may be the case that this situation will only give one peak in the action.

Note that the size distribution measured from the action also peaks at a smaller value of ρ than that measured from the charge; at 23 sweeps the maximum of the size density calculated from the action is at $\rho_{\max} = 4.5$ while the maximum of the size density measured from the charge occurs at $\rho_{\max} = 5.5$. The action is always positive and so it is assumed that the action density at the instanton centre is given as

$$S_{\text{peak}} = S_{\text{inst}} + S_{\text{background}} \tag{3.8}$$

where $S_{background}$ is the contribution from all other peaks in the action, while

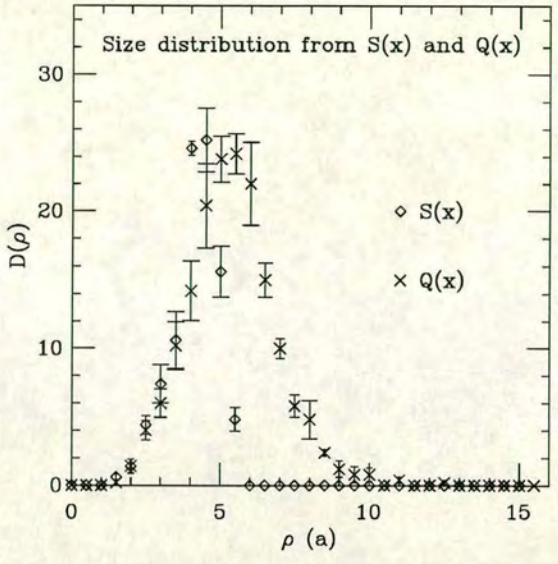

Figure 3.3: size distribution from $S(x)$ and $Q(x)$ at 23 sweeps

because the topological charge has either sign, the correction is assumed to be negligible at least relative to the correction from the action. This approximation will be improved later in this chapter. Therefore

$$Q_{\text{peak}} = Q_{\text{inst}} \tag{3.9}$$

Now assume there is an instanton of width $\rho \approx 5.5$. If equation 3.8 is assumed then including the background term, which is taken to be the average action, $\langle S(x) \rangle$, on one configuration, in the calculation of the instanton width gives a ρ_{peak} calculated from the action of approximately 4.8 which will be binned in the bin corresponding to $\rho = 4.5$. The above argument involves many approximations but it does explain the shift to smaller sizes of the distribution calculated from the action density. Given this large discrepancy in the number of peaks it is interesting to see how the peaks in the action and charge are related to each other. If the configurations were (locally) self dual then the peaks in the action and charge would occur at the same point. A peak in the action and a peak in

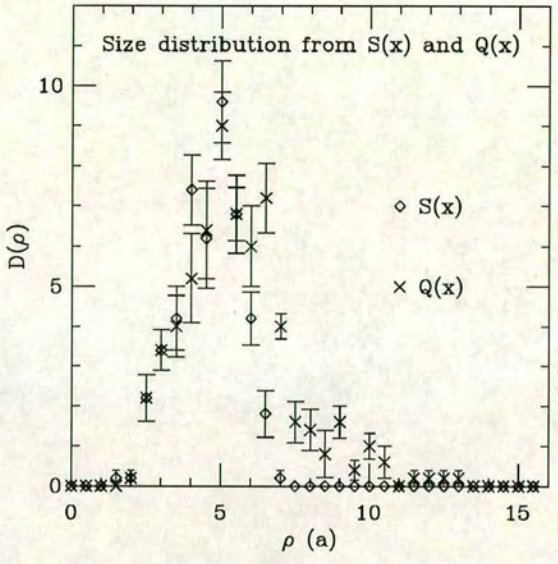

Figure 3.4: size distribution from $S(x)$ and $Q(x)$ at 46 sweeps

sweep	#peaks in $S(x)$	R	#peaks with $\lvert x_{action} - x_{charge} \rvert \leq R$
23	95	0	54
23	95	2	86
46	46	0	33
46	46	2	43

Table 3.2: Number of peaks in $S(x)$ that can be indentified with a peak in $Q(x)$

the charge are defined to belong to the same object if

$$\|x_{action} - x_{charge}\| \leq R \tag{3.10}$$

The results are given in table 3.2 for $R = 0, 2$ (R is chosen to be much less than than the average size of the instantons) and show that most of the peaks in the action can be idenitified with peaks in the topological charge.

In light of the fact that the action only gives information on small objects there is little to be gained from using it to identity large instantons. The analysis that

follows uses only $Q(x)$ and not $S(x)$.

3.5 Peak Iteration

The previous results have shown that the cooled configurations are very crowded. Because of their interactions the instantons are expected to be distorted.

Each local maximum (minimum) is assumed to be an (anti-)instanton. The peak height of each object will receive contributions from all the other objects in the vacuum. In order to get the true width of each object it is therefore necessary to disentangle the contributions to each peak of all the other peaks. Each peak is treated as a linear superposition of the contributions from all the instantons

$$Q_i(x) = Q_{\text{peak}}(\rho_i) + \sum_{j \neq i} \text{sign}(i) Q_I(|x_j - x_i|, \rho_j) \tag{3.11}$$

where Q_{peak} is the lattice corrected formula for the peak height defined in equation 3.7 and $Q_I(|x - x_0|, \rho)$ is the continuum instanton charge density (eqn.1.42). A set of self-consistent widths is then found by iteration. This linearisation is only a first approximation (the topological charge densities will not be additive in general), as is the use of the continuum formula for the instanton charge density (equation) 1.42 in the subtractions.

The initial widths are calculated from the initial peak height using equation 3.7 and the Newton Raphson method. These widths are used to seed the Peak Iteration algorithm. The algorithm then proceeds as follows.

1. For each peak, calculate an adjusted peak height by subtracting from the original peak height all the contributions from every other peak assuming that the charge density contribution from each peak obeys the single instanton formula.

2. From this adjusted peak height calculate the new width using the Newton-Raphson method. This new peak height is now used in the subtraction of the contribution of this peak to the other peaks. Doing this for all the

peaks constitutes a sweep of the algorithm.

In order to remove some peaks that are just "ripples" in the charge density and do not correspond to instantons, any peak that has the opposite sign after the subtraction of the contribution from all the other peaks is removed from the procedure and plays no further part in the analysis. The number of peaks thrown out by this filter is in general small. For example on 20 $\beta = 6.0$ $16^3 \times 48$ lattices after 23 under-relaxed cooling sweeps at $\alpha = 1$ where, on average, there are 169 peaks per configuration this filter did not affect thirteen of the configurations, removed one peak from six of the configurations and removed four peaks from one configuration.

The criteria for convergence is

$$\frac{\rho_{\text{new}} - \rho_{\text{old}}}{\rho_{\text{new}}} < 0.001 \tag{3.12}$$

for all the peaks during a sweep. The peak iteration algorithm has converged on all the cooled charge densities it has been applied to.

The final results of the algorithm do not depend on the order in which the peaks are considered. This was checked by randomising the order in which the algorithm was applied to the peaks. In particular, the peaks frozen out by the algorithm do not change with the random ordering.

In order to see the effects of the algorithm it is useful to define

$$\delta\rho = \text{abs}\left(\frac{\rho_{\text{final}} - \rho_{\text{orig}}}{\rho_{\text{orig}}}\right) \tag{3.13}$$

Figure 3.5 shows the number of peaks that have a relative change $\delta\rho$ averaged over 20 $\beta = 6.0$ $16^3 \times 48$ lattices after 23 sweeps. This shows that the effect of the iteration procedure is not overly substantial; many final widths have not been moved very far from their original values. Figure 3.6 plots $\langle\delta\rho\rangle$ against ρ_{final}. The points with $\langle\delta\rho\rangle = 0$ are points where there was no ρ_{final} in that bin. This plot shows that in general a larger ρ_{final} of the peak corresponds to a larger $\langle\delta\rho\rangle$.

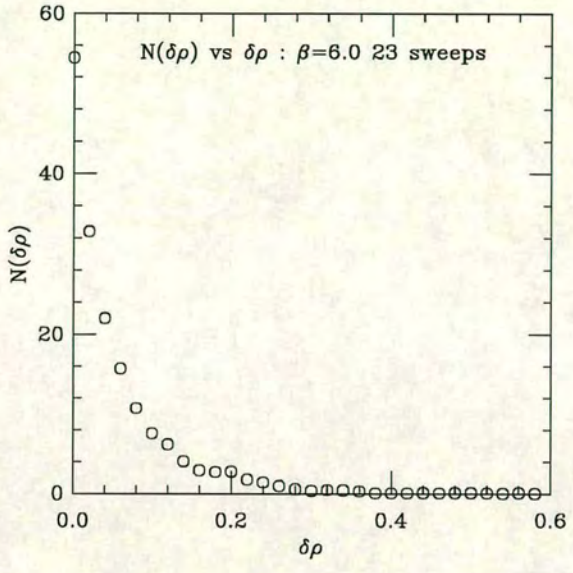

Figure 3.5: $N(\delta\rho)$ vs ρ

This can be explained as follows. Subtracting a small constant ϵ from a peak causes a relative change $\delta\rho \propto \rho^4_{\text{orig}}$; the effect on ρ of subtracting the constant will therefore increase as ρ_{orig} increases.

3.6 Filtering the results

Assuming that the topological charge of each configuration is carried solely by instantons then

$$Q = \frac{1}{32\pi^2}\int d^4x F_{\mu\nu}(x)\tilde{F}_{\mu\nu}(x) = n_I - n_{\bar{I}} \tag{3.14}$$

where n_I is the number of instantons and $n_{\bar{I}}$ is the number of anti-instantons in the configuration. Assuming each peak found in the charge density is an (anti-) instanton and comparing $n_I - n_{\bar{I}}$ to Q shows a large discrepancy. Calling each peak an instanton is therefore wrong and a way must be found of deciding which peaks correspond to instantons and which peaks are just fluctuations. Define the error δ as follows

$$\delta = \langle |Q - (n_I - n_{\bar{I}})| \rangle \tag{3.15}$$

δ for the $\beta = 6.2$ data is shown in table 3.3.

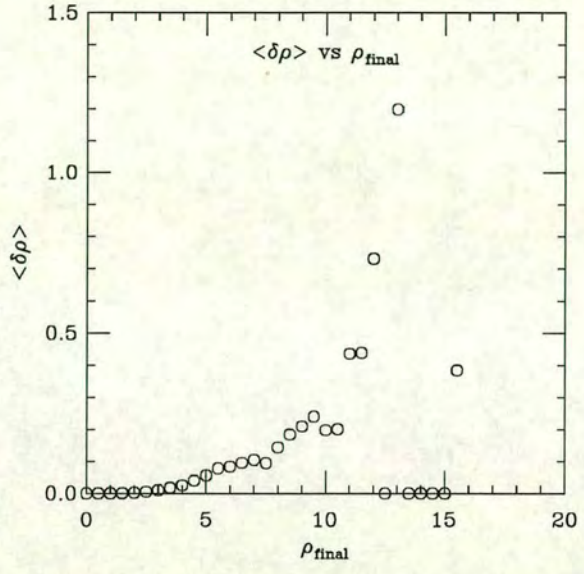

Figure 3.6: $\langle \delta\rho(\rho) \rangle$ vs ρ

sweep	δ
23	12.45
32	10.39
46	7.08

Table 3.3: δ vs cooling sweep for $\beta = 6.2$

Note that the discrepancy is very large. Secondly, note that as the number of sweeps increases δ decreases. This is to be expected as the further the configuration is cooled the smoother the configuration will be. Finally if our pattern recognition was perfect $Q = n_I - n_{\bar{I}}$. Filters are therefore imposed to reduce δ.

The first step in this procedure is to correct Q to take into account the discretisation errors from small instantons. Recall that measuring Q using $F_{\mu\nu}\tilde{F}_{\mu\nu}$ does not give an integer value as it would do in the continuum. This is a result of discretisation errors. In order to quantify these errors a single instanton is discretised on a 16^4 lattice (finite volume effects are not expected here as the instanton width is small compared to the lattice size) and cooled down. The data is plotted

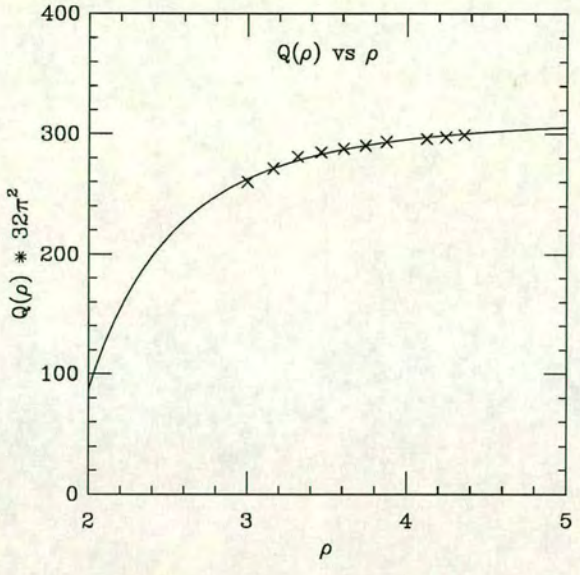

Figure 3.7: $Q(\rho)$ vs ρ

in figure 3.7. The data is fitted to

$$Q_{\text{fit}}(\rho) = 1 + \frac{a}{\rho^2} + \frac{b}{\rho^4} \tag{3.16}$$

and the best fit is $a = -0.413$ and $b = -9.956$. This function will fail for small ρ, at small enough ρ equation 3.16 will give $Q < 0$ for an instanton. We therefore impose that the charge of an instanton is

$$Q(\rho) = Q_{\text{fit}}(\rho), \rho > 2 : Q(\rho) = Q_{\text{fit}}(2), \rho \leq 2 \tag{3.17}$$

On each configuration Q is calculated from $F\tilde{F}$, corrected using equation 3.17, and finally rounded to the nearest integer. This is what is now used in the calculation of δ_{min}. Correcting the charge of the configuration using this function gives lower values of δ_{min} than not correcting using this function.

After this calculation was completed it was noticed that the charge used in $Q(\rho)$ had not been fixed in the same way as the peak height in the measurement of

$Q_{peak}(\rho)$ (the charge taken was the lowest charge at that radius as opposed to the highest one as it should have been). Fitting the new data to the same functional form gives $a = -0.65$ and $b = -5.344$ in equation 3.7. It has been explicitly checked that this makes no significant difference to the topological susceptibilty and the behaviour of the instanton distributions e.g. spatial distributions, charge correlations etc. remains the same.

3.7 Filter 1: Comparison of widths

So far ρ has been calculated from the corrected peak height of each instanton. In the peak iteration algorithm it has been assumed that all the instantons are spherically symmetric and the charge density is described by the continuum instanton formula 1.42. The first filter that is applied is to examine how well each peak resembles a continuum instanton. In order to do this it is necessary to define the width in another way. A second width is defined by examining the charge contained within a radius R of the center of the instanton.

In the continuum, the charge within a radius R can be calculated analytically

$$Q_{\text{cont}}(|x| \leq R) = 1 - 3y^2 + 2y^3 \tag{3.18}$$

with

$$y = \frac{1}{1 + \frac{R^2}{\rho^2}} \tag{3.19}$$

On the lattice for small ρ there are corrections to this formula and as before these are calculated by cooling an instanton on a 16^4 lattice. The corrections were calculated for $R = 2$ and $R = 3$ and are plotted in figures 3.8 and 3.9. The width calculated from the charge within a radius 2 of the centre of the instanton is denoted ρ_2 and within a radius 3, ρ_3.

The lattice formula was fitted to

$$Q_{\text{latt}}(|x| \leq R) = Q_{\text{cont}}(|x| \leq R) + \frac{a}{\rho^2} + \frac{b}{\rho^3} \tag{3.20}$$

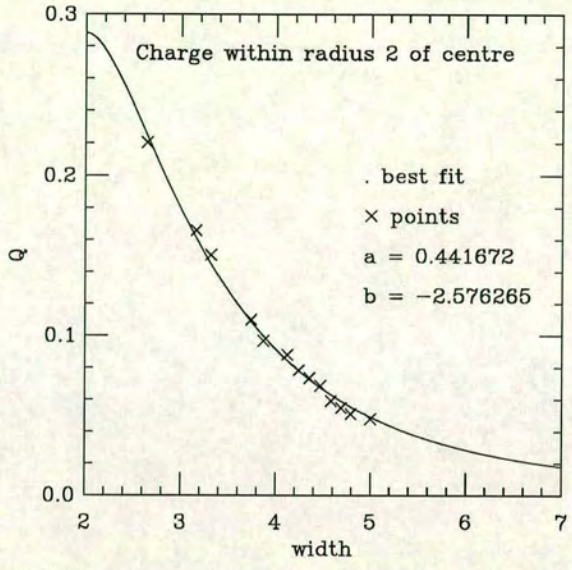

Figure 3.8: Charge within $R \leq 2$ for a single instanton

The functional form of the corrections is heuristic; a more theoretically motivated functional form is

$$Q_{\text{latt}}(|x| \leq R) = Q_{\text{cont}}(|x| \leq R)(1 + \frac{a}{\rho^2}) \tag{3.21}$$

The results are given in table 3.4. Our corrections do not work for $\rho < 3$ and

R	a	b
2	0.4417	-2.576
3	0.204	-2.920

Table 3.4: Best fits for charge within a radius R

also cannot find a width for peaks with too high a topological charge in the region; the fits do not give sensible results. However, this is not a problem as small instantons are distinct and there will be no problem identifying them and in these cases ρ_R is set to be ρ_{peak}.

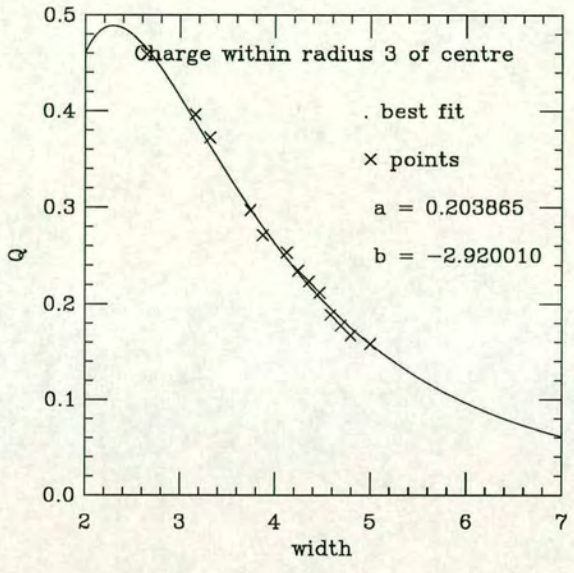

Figure 3.9: Charge within $R \leq 3$ for a single instanton

For large ρ our corrections also do not work. In the continuum, as $\rho \to \infty$ then

$$Q(|x| < R) \propto \frac{R^4}{\rho^4} \tag{3.22}$$

and the corrections go as $\frac{1}{\rho^2}$. Therefore for large ρ the corrections calculated must not be used as these will dominate the calculation of ρ_R from the $Q(|x| < R)$. The final function used is then

$$Q(|x| < R) = Q_{cont}(|x| < R) + \left(\frac{a}{\rho^2} + \frac{b}{\rho^3}\right)\theta(-\rho - \frac{b}{a}) \tag{3.23}$$

Each peak now has at least 2 widths associated with it and for the peak to be called an instanton the widths must sufficiently agree with each other.

The algorithm calculates $Q(|x| < R)$ for each instanton. It subtracts off the contributions to $Q(|x| < R)$ from all the other peaks assuming they all obey the continuum instanton formula and from the corrected quantity calculates ρ_R.

The consistency is then defined as follows; the peak is an instanton if

$$\text{Max}\left(\frac{\rho_R}{\rho}, \frac{\rho}{\rho_R}\right) - 1 < \epsilon \tag{3.24}$$

where ϵ is a parameter that must be fixed.

3.8 Filter 2: Spatial Filter

If the instantons are very large it is possible that as well as the peak at the centre, the instanton will also have extra "ripples" on it. These extra "ripples" will give extra peaks in the pattern recognition algorithm and contribute to the error δ. A "spatial filter" is imposed on the charge density to remove some of these spurious peaks.

A peak is discarded from the distribution if all the following conditions are satisfied.

1. The nearest neighbour to the peak under consideration has the same sign and has not already been removed by this filter.
2. The width of the peak, ρ_{peak}, and the width of its nearest neighbour, ρ_{closest}, are both greater than some ρ_{cut}. ρ_{peak} and ρ_{closest} are the widths calculated from the corrected peak height.
3. $c(\rho_{\text{peak}} + \rho_{\text{closest}}) > |\underline{x}_{\text{peak}} - \underline{x}_{\text{closest}}|$

The algorithm moves through the lattice in a random order so the peak removed by this algorithm is effectively chosen at random.

Condition 2 follows from the fact that this filter is only wanted to apply to broad instantons; small instantons will be distinct and should not need filtering by this method. Condition 3 looks at the distance between the peaks and compares this to a criterion based on the widths of the objects under consideration. The filter is based on the widths for the following reason. Suppose there were two like peaks a distance 7 apart. If the peaks had $\rho = 5$ then it is unlikely that one peak was a

fluctuation on top of the other but if both peaks had $\rho = 9$ then it is much more likely that one is just a "ripple" on top of the other.

This filter has two parameters that must again be fixed; ρ_{cut} and c. Making c a parameter to be fixed rather than setting it to be say $\frac{1}{2}$ allows lower values of δ.

3.9 Choice of Filters

The filters are applied to the cooled charge densities in the following order

1. The spatial filter is applied for a particular value of ρ_{cut} and c.
2. The width filter is then applied for a particular value of ϵ.

The data was generated for the ρ_2 filter and the $c\rho 3$ filter. Another width filter denoted $\rho_2 + \rho_3$ is also considered. With this filter a peak is an instanton if

$$\text{Max}\left(\frac{\rho_2}{\rho}, \frac{\rho}{\rho_2}\right) - 1 + \text{Max}\left(\frac{\rho_3}{\rho}, \frac{\rho}{\rho_3}\right) - 1 < \epsilon \tag{3.25}$$

In order to avoid a configuration dependent filter δ is minimised over all of the configurations considered. In this study for each β value, sweep and volume, δ was minimised over a subset of 20 configurations.

3.10 Consistency Check

The spatial filter throws out peaks on the basis of their width and their distance apart. As well as throwing out ripples on the instantons it may also be throwing out "real" instantons as well. It is therefore necessary to have an estimate of the number of "real" instantons thrown out by the filter. If this number is small then there is not a problem. However if this is not the case then the filter is itself introducing another source of error. The aim of this method is to estimate the number of times the filter has mistaken two nearby instantons as a single instanton and a ripple.

The number of instantons thrown out by the spatial filter is estimated using a Monte-Carlo technique. The data is first filtered using the filters that minimise δ for the data set considered. Any peak that passes all the filters is now counted as an instanton. After filtering the data, all remaining peaks are placed randomly on the lattice. The space filter is then applied and the number of peaks thrown out by it is calculated. This process is carried out 500 times and the results averaged.

This method is only an estimate of the number of "real" instantons thrown out by the filter; it will overestimate the number of real instantons thrown out because, as shown in Chapter 4, there is a tendency for instantons to sit close to anti-instantons in the vacuum. This means that the probability of an instantons' nearest neighbour being another instanton is less than the probability of the nearest neighbour being an anti-instanton. Further, close together like pairs are suppressed. In this method of estimating the error no such effects are taken into account.

3.11 Example : $\beta = 6.2$

This section gives an example of the application of the above methods and examines the effects of the filters. The data set considered is the $\beta = 6.2$, $24^3 48$ lattice after 23, 32 and 46 sweeps.

δ was minimised over a subset of 20 configurations. Care must taken however, a global minimum of δ does not always give the best filter to use. As an example of this consider the data for $\beta = 6.2$ after 32 sweeps. Minimising with respect to the ρ_3 filter gives the following values for the best filters

sweep	ϵ	ρ_{cut}	c	δ_{min}
32	0.46	6.04	0.55	3.50

In this case the model estimate of the number of instantons that are thrown out by the spatial filter are

sweep	#removed by spatial filter	model estimate
32	54.15	48.83

The estimate of the number of instantons thrown out by the values corresponding to the next lowest minima with a lower value of c (the values quoted in table 3.6) gives

sweep	#removed by spatial filter	model estimate
32	11.97	11.23

and shows that in this case the estimate of the systematic error induced by using the values that globally minimise δ is much greater than the estimate for the second set of filter values. The rather high estimate of the number of instantons thrown out by this algorithm with these parameters is an artefact of the low ρ_{cut} value.

In general, therefore, a trade off is made between a slightly higher value of δ and a lower value of c. The final criterion is that the filter used is either the one that gives the lowest value of δ or the values that give the next lowest minima with a higher cut factor and a lower ρ_{cut} than that which gives δ_{min}.

The values taken for the filters and δ_{min} are given for ρ_2 in table 3.5, for ρ_3 in table 3.6 and for $\rho_2 + \rho_3$ in table 3.7.

sweep	ϵ	ρ_{cut}	c	δ_{min}
23	0.27	7.8	0.3	4.40
32	0.20	6.83	0.25	3.55
46	0.11	9.31	0.20	2.25

Table 3.5: Filters for $\beta = 6.2$: ρ_2 filter

Note that, in general, the final δ value is very much less than the starting value; imposing the filters has significantly decreased the discrepancy as can be seen by

sweep	ϵ	ρ_{cut}	c	δ_{min}
23	0.62	7.60	0.3	3.65
32	0.46	6.83	0.25	3.85
46	0.24	7.18	0.20	1.90

Table 3.6: Filters for $\beta = 6.2$: ρ_3 filter

sweep	ϵ	ρ_{cut}	c	δ_{min}
23	0.99	7.60	0.25	4.15
32	0.72	6.83	0.25	3.15
46	0.38	7.18	0.20	2.05

Table 3.7: Filters for $\beta = 6.2$: $\rho_2 + \rho_3$ filter

comparing with table 3.3. Further in general δ decreases with sweep value. With the ρ_3 filter at 32 sweeps the rise in δ is a result of not choosing the filters that give the global minimum of δ. Further as the number of sweeps is increased the value of ϵ decreases. This is expected; as the configurations are cooled further, more and more instantons will annihilate with anti-instantons and the instantons left behind will be less distorted. ϵ for the ρ_3 filter is always greater than for the ρ_2; this may indicate that further from the instanton core the instanton is more distorted.

These filters were calculated over a subset of 20 configurations at $\beta = 6.2$. They are now applied to all the configurations. This can be justified by looking at the δ value from using these filters on all the configurations. As an example after 23 sweeps at $\beta = 6.2$ with the ρ_2 filter imposed δ over all 100 configurations is $\delta = 4.78$, not much higher than the value of δ_{min} quoted in table 3.5.

The effect of the filters varies with the sweep value. Table 3.8 shows how many peaks are thrown out by the filters at each sweep value averaged over all 100 $\beta = 6.2$ configurations.

The model estimate of the number of "real" instantons thrown out by the different

filters for this data set are shown tables 3.9; note that for this data set the estimate of the number of instantons lost is always less for the ρ_2 filter than for the others. The large estimate of the number of peaks thrown out by the filters at 32 sweeps is a results of the relatively low values of ρ_{cut}. At 46 sweeps the same is true for the ρ_3 and $\rho_2 + \rho_3$ data.

sweep	#peaks (unfiltered)	#peaks ρ_2	#peaks ρ_3	#peaks $\rho_2 + \rho_3$
23	540	494	497	498
32	302	274	274	274
46	164	151	150	151

Table 3.8: No of peaks before and after filter $\beta = 6.2$

The effects of the filter are shown by examining the size distribution. The size distribution is plotted in figure 3.10 for 20 configurations at $\beta = 6.2$ after 23 sweeps with both the filtered (using the ρ_2 filter) and unfiltered data. It shows that the filters are mainly affecting the larger instantons. This behaviour is found on all data sets and is expected; it is the large instantons that are expected to be the most distorted as they will overlap with other instantons.

In view of the smaller value of ϵ imposed by the ρ_2 filter it is only the results of this filter that are quoted in the next chapter. However the physics does not greatly change with the filter. As an example of this the size distribution (in lattice units) at $\beta = 6.0$ after 23 sweeps is plotted in figure 3.11 and after 32 sweeps is plotted in figure 3.12. This shows how the mean size of the distribution and the tail of the distribution are not much affected by which filter is used (within statistical errors).

3.12 Comments on Filters

This chapter has described the filters that were developed to analyse the instanton content of the cooled configurations. The whole analysis of the vacuum described here is based upon the semi-classical picture of instantons in QCD; whether this

sweep	filter	#removed by spatial filter	model estimate
23	ρ_2	9.44	3.05
23	ρ_3	12.97	4.33
23	$\rho_2 + \rho_3$	8.91	4.26
32	ρ_2	11.82	11.15
32	ρ_3	11.97	11.23
32	$\rho_2 + \rho_3$	11.82	12.43
46	ρ_2	0.82	0.31
46	ρ_3	1.8	2.22
46	$\rho_2 + \rho_3$	1.8	2.33

Table 3.9: model estimate of "real" instantons lost by filter

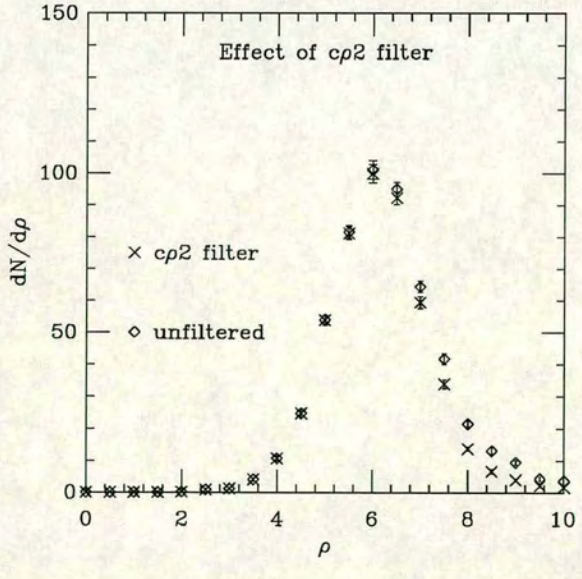

Figure 3.10: Filtered and unfiltered size distribution $\beta = 6.2$

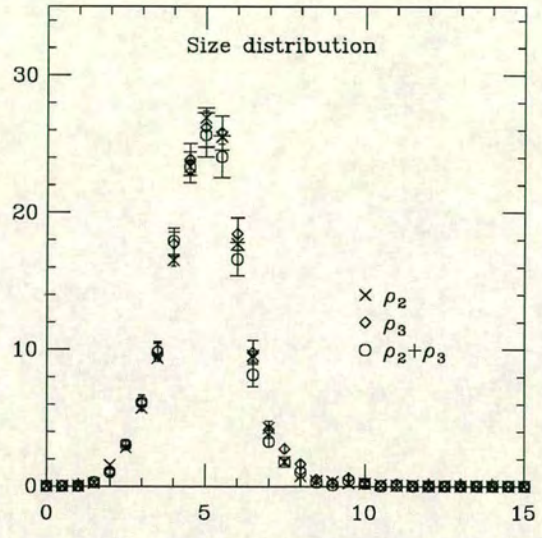

Figure 3.11: Size distribution $\beta = 6.0$: 23 sweeps

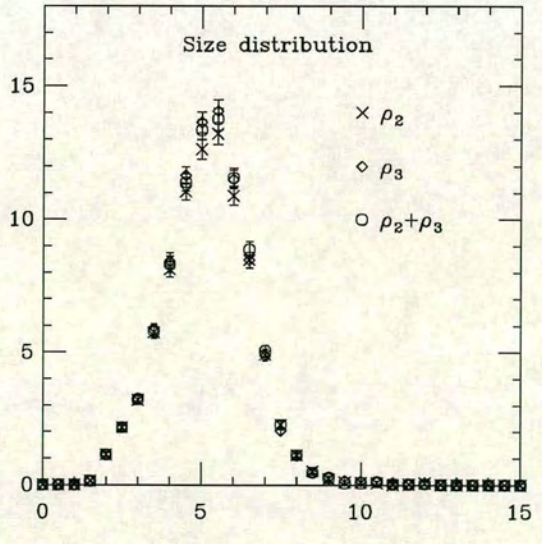

Figure 3.12: Size distribution $\beta = 6.0$: 32 sweeps

is the appropriate way to view the QCD vacuum is an open question[32] and will depend on the details of the instanton distributions [16]

The peak iteration algorithm has assumed a linear superposition of the topological charge densities of instantons and anti-instantons. This is only a good approximation if the instantons are dilute i.e. $\langle\rho\rangle << \langle R\rangle$ where $\langle\rho\rangle$ is the average size and $\langle R\rangle$ the average separation. However the results of chapter 4 show that this is not the case and the peak iteration algorithm may be improved by trying to (at least partially) correct for these distortions.

The width filter that was applied to the data also assumes that all the instantons are (nearly) spherical and the distortions minimal. The filters are imperfect; the fact that $\delta \neq 0$ shows this. It may be possible in the future to find better pattern recognition algorithms that will reduce δ further and also reduce the number of "real" instantons that are removed by the filter as well. It may also be possible to develop a better estimator of the number of "real" instantons thrown out by the algorithm as well. The estimator does, however, give a criterion for deciding on which filter values to use.

One final point. The techniques that are described in this chapter were developed as the calculation progressed; a future calculation would use, for example, more theoretically motivated fit functions for the filters. However this in no way detracts from the results of the methods presented here.

Chapter 4

Structure of the QCD vacuum

This chapter applies the analysis techniques developed in the previous chapters to elucidate the structure of the $SU(3)$ vacuum. The cooled vacua are studied for 100 $24^3 \times 48$, $\beta = 6.2$ configurations, 100 $16^3 \times 48$,$\beta = 6.0$ configurations and 50 $32^3 \times 64$, $\beta = 6.0$ configurations.

The question of at what level of cooling the data should be analysed is a difficult one. Ideally the cooling should be stopped before it changes the distribution. However in practice the cooling will continually change the distribution until all that is left are very isolated instantons. At this stage the distribution will not change much with cooling but it will have little to do with the original distribution in the hot configuration. In [28],the number of cooling sweeps at each β value was chosen to be the number of cooling sweeps it took to return a thermalised single instanton to a cold single instanton at each β value.

In this study, the data is analysed at a number of different sweeps in order to watch how the distributions vary during the cooling. This study uses under-relaxed cooling with $\alpha = 1$. The $\beta = 6.2$ data was analysed at $23, 32$ and 46 cooling sweeps and the small volume $\beta = 6.0$ data was analysed at $23, 28, 32$ and 46 cooling sweeps. A finite volume study is carried out by comparing the small $\beta = 6.0$ volume with the large $\beta = 6.0$ volume after 46 sweeps.

All errors in the chapter were estimated using the Jackknife method except the errors quoted on the fits to the size distributions which were estimated using the Bootstrap method.

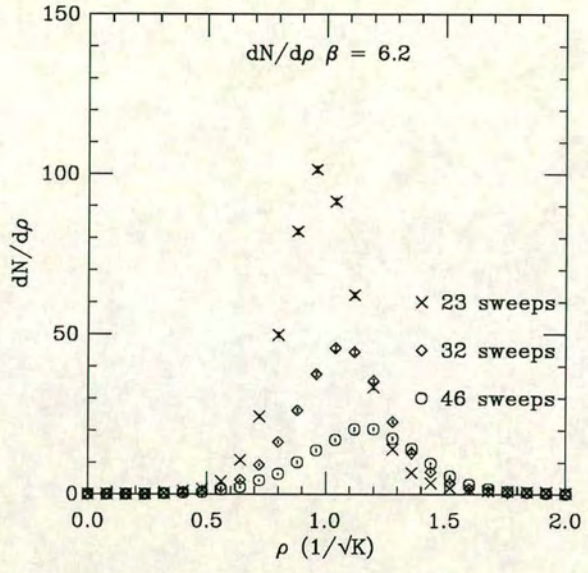

Figure 4.1: $\frac{dN}{d\rho}$: $\beta = 6.2$

The values of the string tension are taken to be $a\sqrt{K} = 0.22$ at $\beta = 6.0$ and $a\sqrt{K} = 0.16$ at $\beta = 6.2$ [33].

4.1 Size Distribution

The size distribution is plotted in figure 4.1 for the $\beta = 6.2$ data with the ρ_2 filter implemented. The data from the $\beta = 6.0$, $16^3 48$ lattices are shown in 4.2 again with the ρ_2 filter imposed.

As found in all other calculations, $\frac{dN}{d\rho}$ rises steeply to a peak and then falls off. The number of peaks varies rapidly with cooling as shown in table 3.8, however the average size of the instantons, $\langle\rho\rangle$, does not vary so much as shown in figure 4.3.

The distributions are peaked around $\rho \approx \frac{1}{\sqrt{K}}$ although as the configurations are cooled further the peak and the average size move to larger values of ρ. In [34] it was found that $\rho_{peak} \approx 0.6fm$ which is slightly larger than, but still consistent with, the values quoted here.

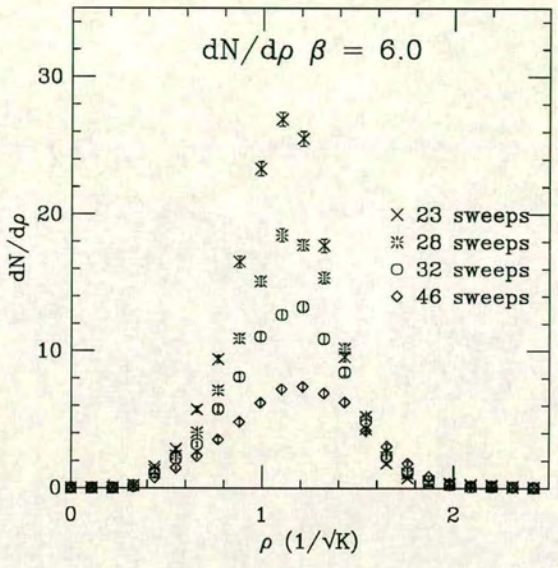

Figure 4.2: $\frac{dN}{d\rho}$: $\beta = 6.0$

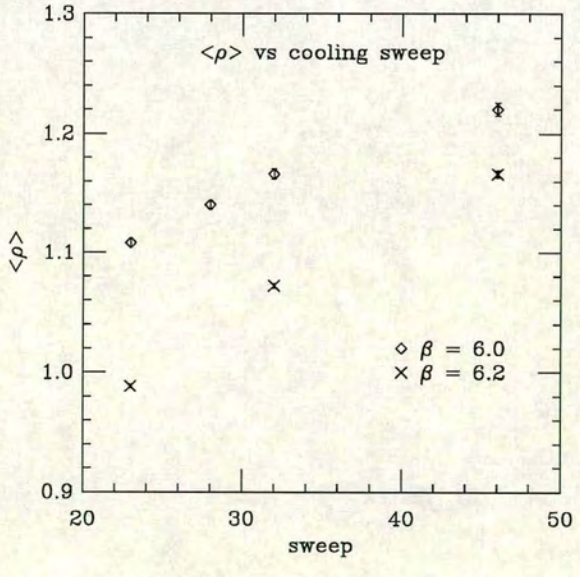

Figure 4.3: $\langle\rho\rangle$ vs sweep

The impact of a cooling sweep does not scale. The cooling sweep implemented here only depends on the links that form the plaquettes of which the link under consideration is a member. The influence of a particular link will only spread $\sqrt{2}a$ during every cooling sweep and so it will take longer for information about a particular link to travel the same physical distance at a higher β value. This makes the analysis of the scaling somewhat more complicated.

Figure 4.4 shows the size distributions for $\beta = 6.2$ and $\beta = 6.0$ after 23 cooling sweeps. Obviously the distributions do not scale although the tails of the distributions are more similar. However, comparing the size distributions at different levels of cooling does give (approximate) scaling behaviour, as shown in figure 4.5. The plot shows that the number of cooling sweeps can be tuned so as at

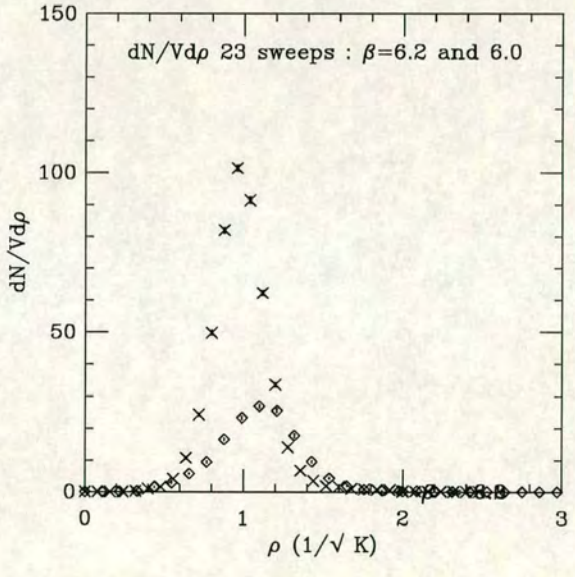

Figure 4.4: $\frac{dN}{Vd\rho}$ at 23 sweeps, $\beta = 6.2$ and $\beta = 6.0$

least the tails of the distributions will scale. The $\beta = 6.2$ data after 46 sweeps is much closer to the $\beta = 6.0$ data after 28 sweeps however there are some discrepancies; for $\rho < \rho_{\text{peak}}$, the $\beta = 6.2$ data lies below the $\beta = 6.0$ data. A more careful tuning of the number of cooling sweeps may yield an even better scaling behaviour for the distributions.

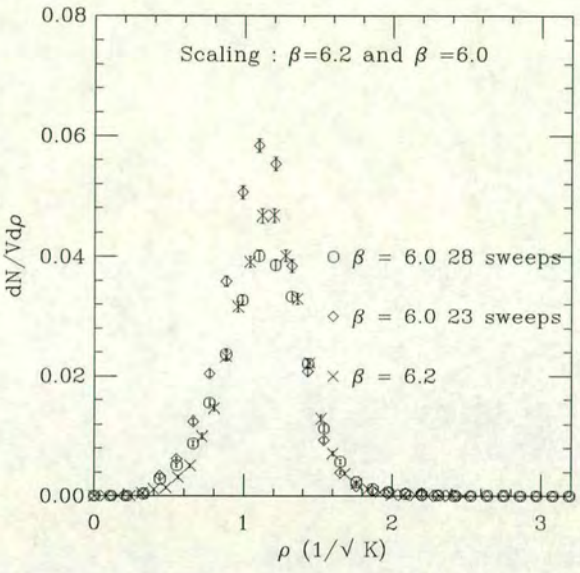

Figure 4.5: $\frac{dN}{d\rho}$ at 23 and 28 sweeps at $\beta = 6.0$ and 46 sweeps at $\beta = 6.2$

The small ρ distributions were fitted to a power law and the results are shown in table 4.1. The fit ranges are given in terms of the string tension. As explained in chapter 1 it would be expected that for small enough ρ $D(\rho) \propto \rho^6$. The distributions here do not show this behaviour. The ρ^6 behaviour is only true for very small ρ where it is expected that cooling will have a large effect on the underlying instanton distributions (cooling will remove instantons with $\rho = O(a)$). Further, for larger values of ρ the logarithmic corrections may have an effect as well so the fact that the distributions do not show the ρ^6 behaviour over the fit ranges (where ρ is not particulary small) is not a problem. For the small ρ distribution there is no stability of the distribution with respect to cooling. However, the trend is that the smaller the lattice spacing and the smaller the number of cooling sweeps the higher the power is. What is needed to further investigate these trends is another calculation at a smaller lattice spacing.

The large ρ tails of the distributions were fitted to both power and exponential functions. It was found that they are also best modelled by a power fall off. The results for the ρ_2 filter are shown in table 4.2 and plotted in figure 4.6. The fit

β	sweep	range	α	χ^2/dof
6.0	23	$0.44 \rightarrow 0.77$	$3.29^{+0.14}_{-0.12}$	1.18
6.0	28	$0.44 \rightarrow 0.99$	$3.11^{+0.08}_{-0.09}$	0.83
6.0	32	$0.44 \rightarrow 0.99$	$2.81^{+0.08}_{-0.09}$	1.82
6.0	46	$0.44 \rightarrow 0.99$	$2.50+0.09_{-0.11}$	0.68
6.2	23	$0.48 \rightarrow 0.80$	$6.86^{+0.11}_{-0.10}$	0.52
6.2	32	$0.48 \rightarrow 0.88$	$5.45^{+0.11}_{-0.13}$	1.24
6.2	46	$0.48 \rightarrow 0.88$	$4.60^{+0.12}_{-0.15}$	1.55

Table 4.1: Best fits to small ρ distribution

β	sweep	range	α	χ^2/dof
6.0	23	$1.43 \rightarrow 1.87$	$-11.90^{+0.38}_{-0.32}$	1.15
6.0	28	$1.54 \rightarrow 2.09$	$-11.68^{+0.45}_{-0.36}$	0.92
6.0	32	$1.54 \rightarrow 2.09$	$-11.78^{+0.53}_{-0.28}$	0.48
6.0	46	$1.65 \rightarrow 1.87$	$-10.04^{+0.97}_{-1.02}$	0.83
6.2	23	$1.2 \rightarrow 1.52$	$-12.49^{+0.25}_{-0.19}$	1.51
6.2	32	$1.36 \rightarrow 1.68$	$-12.34^{+0.23}_{-0.17}$	1.60
6.2	46	$1.44 \rightarrow 2.0$	$-11.79^{+0.35}_{-0.23}$	1.14

Table 4.2: Best fits to tails of distribution

ranges are again given in units of the string tension. In general for large ρ the distributions fall off very fast. There is little variation of the best fit between 23 and 32 sweeps at $\beta = 6.2$. Comparing $\beta = 6.2$ after 46 sweeps and $\beta = 6.0$ after 23 and 28 sweeps shows the best fits agree within errors over the same physical range (as expected). If it was assumed that the instanton distribution obeyed the semi-classical formula and the gauge coupling $g(\rho)$ stopped running above some value $\rho_{\mathbf{max}}$ then the size distributions would obey

$$D(\rho)d\rho \propto \frac{d\rho}{\rho^5} \tag{4.1}$$

The best fits above however indicate a much sharper cut-off than this.

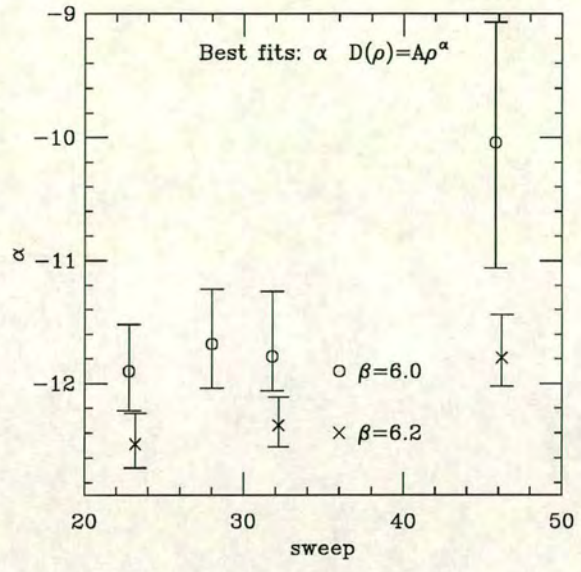

Figure 4.6: Best fits to tails of distributions

4.2 Spatial Distributions

The instanton spatial distributions were calculated by counting the number of (un)like charges in the spherical shell of width dR a distance R away from each object. The distributions are then normalised by the volume of each shell.

The first distribution examined is the like charge distribution. The results are plotted for $\beta = 6.2$ after 23 sweeps in figure 4.7 and at $\beta = 6.0$ after 23 sweeps in 4.8 , both with the ρ_2 filter imposed. The distributions are also normalised so that the maximum of the distribution is equal to one. The plots show the distributions are suppressed at short distances (there are very few instanton instanton pairs) and uniform at long distances. The suppression at short distances also occurs on the unfiltered data and so is not a product of the filtering proceedure.

The unlike distributions are plotted for the same data sets in 4.9 and 4.10. These plots show an amplification of unlike pairs close by each other. This is expected; the action of an annihilating pair will be less than the action of a well separated pair and so it is expected many such pairs will be seen. The data shows that as

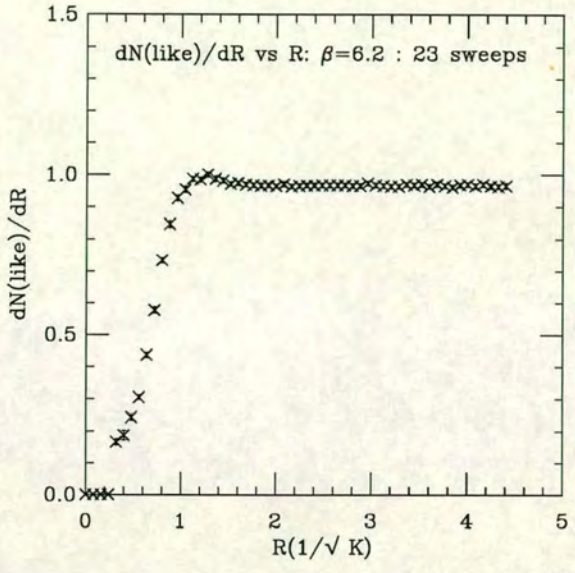

Figure 4.7: $\frac{dN(like)}{dR}$ after 23 sweeps at $\beta = 6.2$

in the like case the distribution is uniform at long distances. Note that in the $\beta = 6.2$ there is a dip in the spatial distribution near $R \approx \frac{1}{\sqrt{K}}$. This corresponds to a small amplification of like objects at this distance as shown by figure 4.7. The same dip is seen in the $\beta = 6.0$ data near $R = \frac{1.6}{\sqrt{K}}$. The mean distance to the nearest like and unlike neighbours is plotted against cooling sweep for both the $\beta = 6.2$ and $\beta = 6.0$ data in figure 4.11. The results show that at all the sweep values considered, unlike objects will on average sit closer to each other than like objects, as expected. Further as cooling proceeds the distance between objects increases. This is presumably a result of nearby instantons and anti-instantons annihilating each other as a result of the cooling.

4.3 Validity of the dilute gas approximation

The behaviour shown by the size and spatial distributions calls into question the assumption that the vacuum is dilute i.e. that the average size of the instantons is much less than their separation. The Interacting Instanton Liquid model assumes that instantons have an average size of $\frac{1}{3}fm$ and $\frac{\langle\rho\rangle}{\langle R\rangle} \approx \frac{1}{3}$; the results here give $\frac{\langle\rho\rangle}{\langle R\rangle} \approx 1$ and imply that a dilute description of the instanton vacuum is

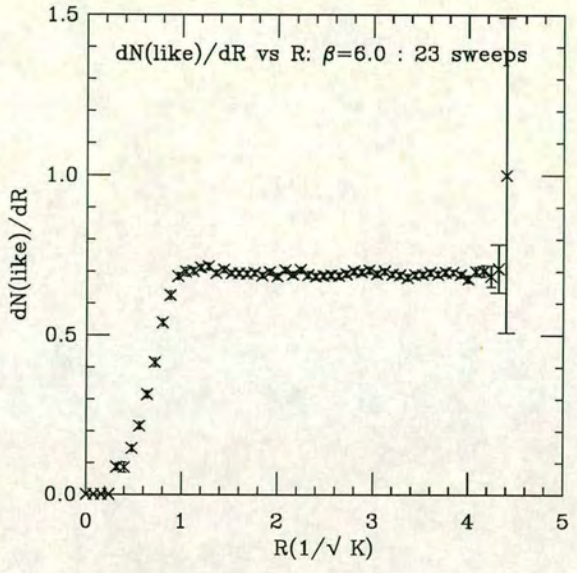

Figure 4.8: $\frac{dN(like)}{dR}$ after 23 sweeps at $\beta = 6.0$

questionable. The same conclusion was reached in [34].

It is interesting however to investigate if the dilute gas approximation does hold in some regime. The dilute gas approximation assumes that the distributions of instantons and anti-instantons are independently poisson.

$$P(n_I, n_{\bar{I}}) = \frac{e^{-m} m^{n_I}}{n_I!} \frac{e^{-m} m^{n_{\bar{I}}}}{n_{\bar{I}}!} \tag{4.2}$$

where $m = S_{inst}$. In this approximation it can be shown that

$$< Q^2 > = < n_I + n_{\bar{I}} > \tag{4.3}$$

On each configuration Q is calculated by integrating the topological charge density and then corrected using equation 3.17 for all peaks that have been identified as instantons. The results for the $\beta = 6.2$ are shown in 4.3. It is obvious from this table that the instanton vacuum does not obey the dilute gas approximation; even in an approximate sense. However the dilute gas approximation may hold for instantons below a certain size. In order to investigate this the following

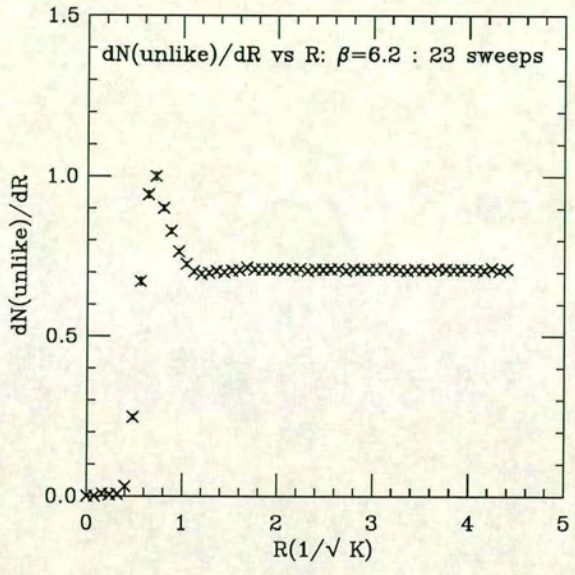

Figure 4.9: $\frac{dN(unlike)}{dR}$ after 23 sweeps at $\beta = 6.2$

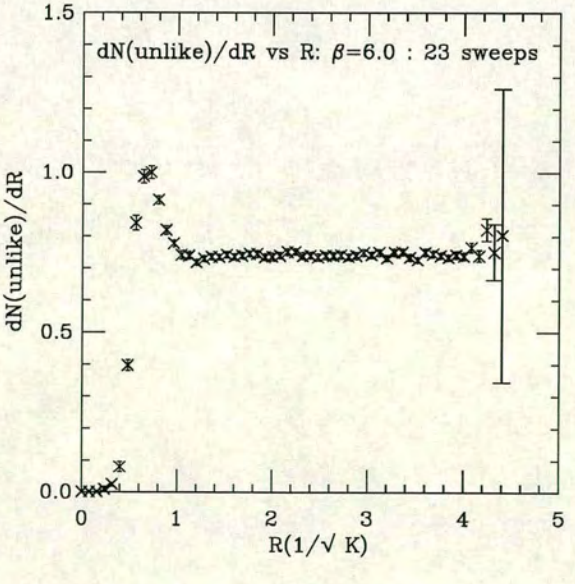

Figure 4.10: $\frac{dN(unlike)}{dR}$ after 23 sweeps at $\beta = 6.0$

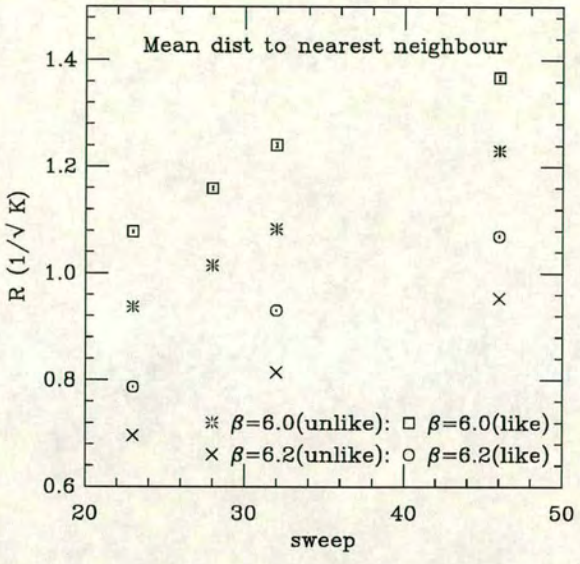

Figure 4.11: Mean distance to nearest (un)like neighbour

sweep	$< Q^2 >$	ρ_2
23	18.08	494
32	16.41	274
46	15.92	151

Table 4.3: $\langle Q^2 \rangle$ and $\langle n_I + n_{\bar{I}} \rangle$

quantity is investigated

$$P(\rho_{\rm cut}) = \left\langle \frac{Q^2(\rho \leq \rho_{\rm cut})}{N(\rho \leq \rho_{\rm cut})} \right\rangle \tag{4.4}$$

where $N(\rho \leq \rho_{\rm cut})$ is the number of instantons of size $\rho \leq \rho_c$ and $Q(\rho \leq \rho_{\rm cut})$ is the charge carried by them. The results are plotted for $\beta = 6.2$ data at 23 sweeps in figure 4.12 and 46 sweeps in figure 4.13.

The plots show that for small $\rho_{\rm cut}$ the distribution does approximately obey the dilute gas approximation, $P(\rho_{\rm cut}) \approx 1$. For large $\rho_{\rm cut}$ the behaviour is given by the ratio of the results in table 4.3. However, when $\rho_{\rm cut}$ is close to the peak in the

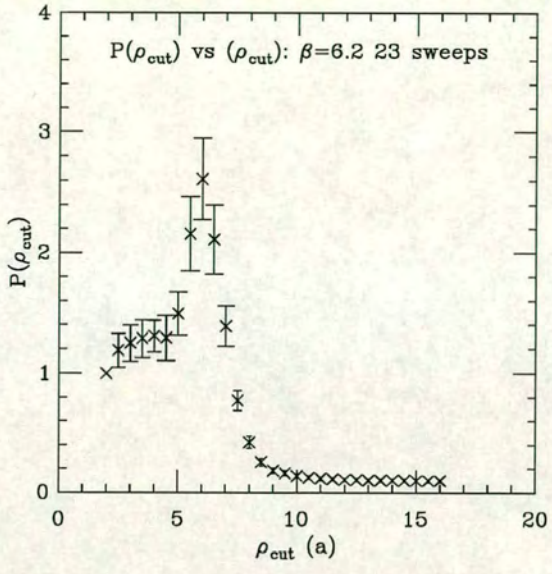

Figure 4.12: $P(\rho_{\rm cut})$ vs $\rho_{\rm cut}$: $\beta = 6.2$, 23 sweeps

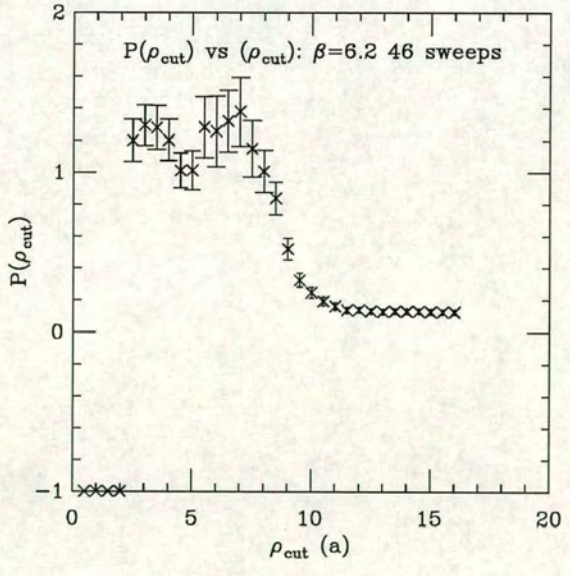

Figure 4.13: $P(\rho_{\rm cut})$ vs $\rho_{\rm cut}$: $\beta = 6.2$, 46 sweeps

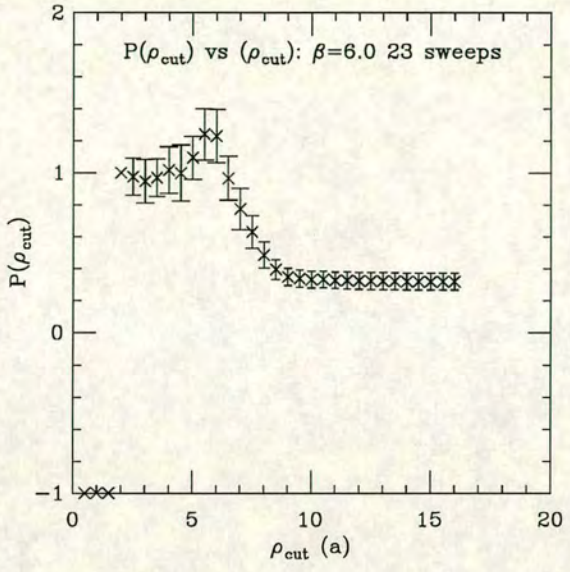

Figure 4.14: $P(\rho_{\text{cut}})$ vs ρ_{cut} : $\beta = 6.0$, 23 sweeps

size distribution there is a large peak in $P(\rho_{\text{cut}})$. Note as the cooling continues this peak monotonically decreases as shown by comparing figures 4.13 and 4.12 indicating that this is not an artefact of the cooling proceedure. This behaviour can also be seen on the $\beta = 6.0$ data as shown in 4.14. Note however that the peak of $P(\rho)$ at $\beta = 6.0$ after 23 sweeps and also after 28 sweeps is within errors of the peak of $P(\rho_{\text{cut}})$ at $\beta = 6.2$ after 46 sweeps and the values of ρ_{cut} of the maximum in physical units are within 10% of each other (to the accuracy they were measured).Further, the peak heights agree with each other within errors. This is, again, evidence with the observation that although the impact of the cooling sweep does not scale with β, the amount of cooling can be tuned so that the distributions (approximately) scale.

4.4 Correlations among the charges

The previous sections have shown that the vacuum is not dilute. Further it has been found that $P(\rho_{\text{cut}}) \geq 1$ for $\rho < \rho_{peak}$ and $P(\rho_{\text{cut}}) \ll 1$ for $\rho \gg \rho_{peak}$.The behaviour of $P(\rho_{\text{cut}})$ implies that as ρ_{cut} is increased there is a large fluctuation in $Q^2(\rho < \rho_{\text{cut}})$. This is shown for $\beta = 6.2$ in figure 4.15 and for $\beta = 6.0$ in figure 4.16

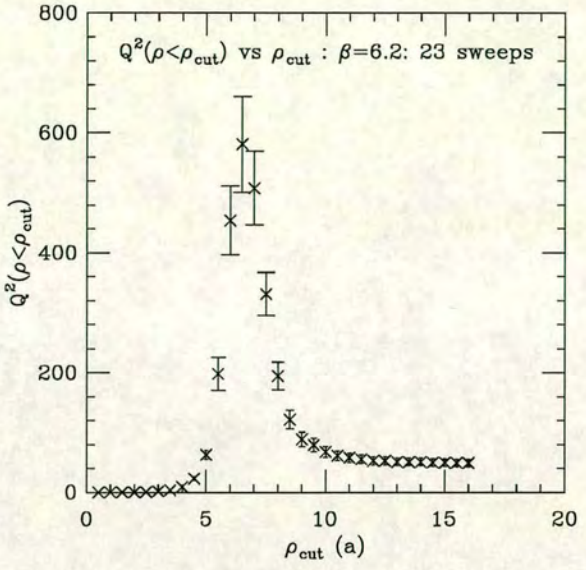

Figure 4.15: $Q^2(\rho < \rho_{\rm cut})$ vs $\rho_{\rm cut}$: $\beta = 6.2$, 23 sweeps

both with the ρ_2 filter imposed. As cooling is increased the height of the peak decreases indicating that this effect is not an artefact of the cooling proceedure; it is not being amplified by further cooling. The peak in $Q^2(\rho < \rho_{\rm cut})$ is very much greater than the average Q^2 of each configuration. The data indicates that there is a tendency for small instantons to have one sign and larger instantons to have the opposite sign; if only instantons with size $\rho < \rho_{\rm cut}$ with $\rho_{\rm cut} < \rho_{\rm peak}$ are considered then there is a large excess of topological charge which is then suppressed when larger instantons are included. This is investigated further by calculating

$$C(\rho) = \left\langle sign(Q).\frac{q(\rho)}{n(\rho)} \right\rangle \tag{4.5}$$

where $q(\rho)$ is the topological charge carried by objects of size ρ and $n(\rho)$ is the number of objects of size ρ on all configurations with topological charge $Q \neq 0$. The results are shown for $\beta = 6.2$ in figure 4.17 and for $\beta = 6.0$ in 4.18, both with the ρ_2 filter imposed.

Note the size at which the change from correlation with Q to anti- correlation with Q takes place almost scales (after the appropriate tuning of the cooling).

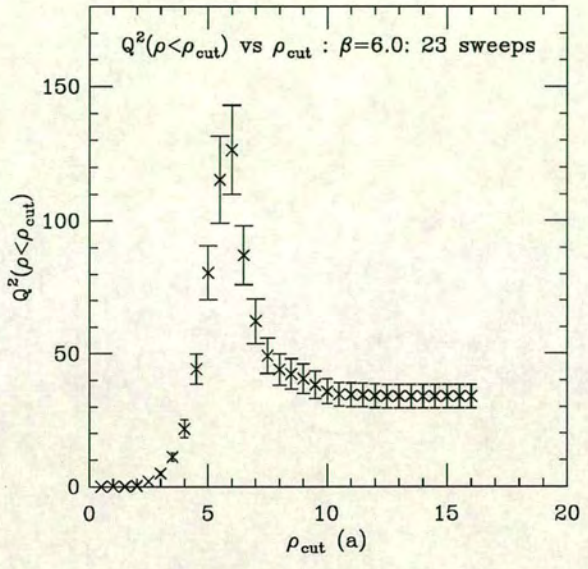

Figure 4.16: $Q^2(\rho < \rho_{\rm cut})$ vs $\rho_{\rm cut}$: $\beta = 6.0$, 23 sweeps

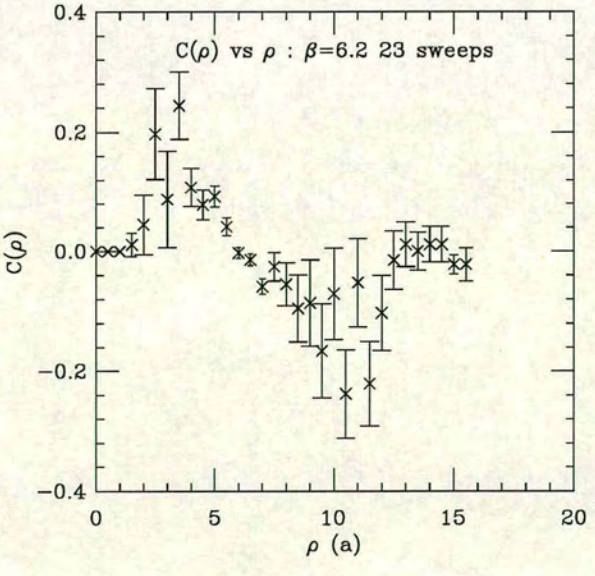

Figure 4.17: $C(\rho)$ vs ρ : $\beta = 6.2$, 23 sweeps

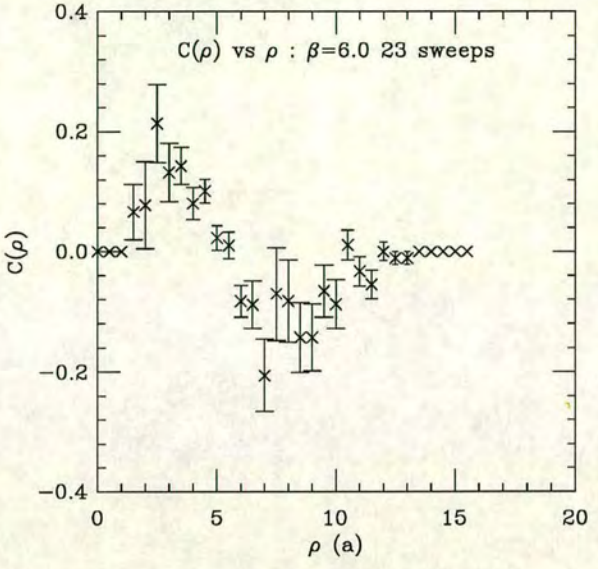

Figure 4.18: $C(\rho)$ vs ρ : $\beta = 6.0$, 23 sweeps

At $\beta = 6.2$ after 46 sweeps $C(\rho) \approx 0$ with $\rho \approx \frac{1.28}{\sqrt{K}}$ while at $\beta = 6.0$ after both 23 and 28 sweeps $C(\rho) \approx 0$ with $\rho \approx \frac{1.21}{\sqrt{K}}$.

The plots show that the charge carried by the small instantons is correlated with the overall topological charge of the configuration and anti-correlated with the charge carried by the large instantons. The implication from this is that the large instantons are *over screened* by small instantons of the opposite sign; i.e a large instanton has more than one small instanton of the opposite sign close by it.

For each instanton the quantity $N_{\text{same}} - N_{\text{opp}}$ is calculated , where N_{same} is the number of instantons of the same charge as the reference instanton, less than a distance R away from the reference instanton, and with size in the range $\rho_{\text{min}} \leq \rho < \rho_{\text{max}}$, and N_{opp} defined in the same way for the opposite charges. $N_{\text{same}} - N_{\text{opp}}$ is binned against the size of the reference instanton ρ_{ref}. Exact screening of each charge would give $N_{\text{same}} - N_{\text{opp}} = -1$; $N_{\text{same}} - N_{\text{opp}} < -1$ indicates overscreening.

Figures 4.19 and 4.20 show $N_{\text{same}} - N_{\text{opp}}$ with $\rho_{\text{min}} = 0$, $\rho_{\text{max}} = \infty$ and $R = \infty$. The plots show that the large instantons are overscreened (for each large instanton

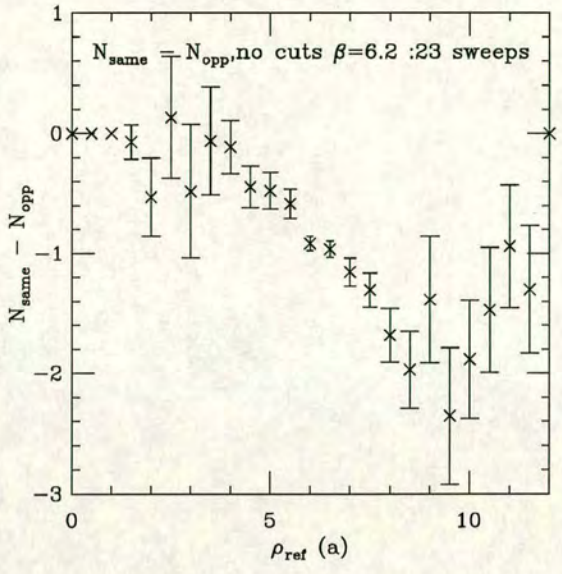

Figure 4.19: $N_{\text{same}} - N_{\text{opp}}$ vs ρ_{ref} : $\beta = 6.2$ 23 sweeps : no cuts

there is more than one anti-instanton). Note that as the configurations are cooled further the overscreening effect disappears.

In figures 4.21 and 4.22 $\rho_{\text{min}} = 0$ and ρ_{max} is taken to be the point where $C(\rho) = 0$. At $\beta = 6.2$ at 23 sweeps $\rho_{\text{max}} = 6.0$ while at 46 sweeps $\rho_{\text{max}} = 8.0$. (in lattice units). The results are shown for three different values of R at $\beta = 6.2$ after 23 sweeps in figure 4.21 and after 46 sweeps in figure 4.22, both with the ρ_2 filter imposed. These plots show that very large instantons are overscreened by nearby anti-instantons. After 23 sweeps, for small ρ_{ref} $|N_{\text{same}} - N_{\text{opp}}|$ is close to zero. As ρ_{ref} in increased $N_{\text{same}} - N_{\text{opp}}$ decreases until for $\rho \geq 8$ and $R \geq 8$ $N_{\text{same}} - N_{\text{opp}} < -1$. At 46 sweeps for $R > 8$ and $\rho_{\text{ref}} > 8$ $N_{\text{same}} - N_{\text{opp}} < -1$; the situation has changed (the screening is not as marked) but again the larger the instanton the more it is screened by instantons of smaller than average size.

Finally $N_{\text{opp}} - N_{\text{same}}$ is plotted but with $\rho_{\text{min}} = 6.0$ and $\rho_{\text{max}} = \infty$ after 23 sweeps in figure 4.23 and $\rho_{\text{min}} = 8.0$ after 46 sweeps in figure 4.24. At 23 sweeps for $\rho_{\text{ref}} > 7.0$, $N_{\text{same}} - N_{\text{opp}} > 0$ for $R = 7, 8, 9$. The same is true after 46 sweeps with $\rho_{\text{ref}} > 9.0$. The implication from these plots is that close together large

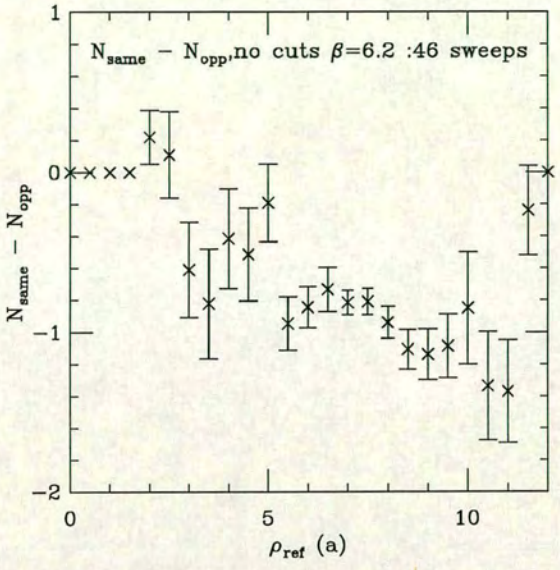

Figure 4.20: $N_{\text{same}} - N_{\text{opp}}$ vs ρ_{ref} : $\beta = 6.2$ 46 sweeps : no cuts

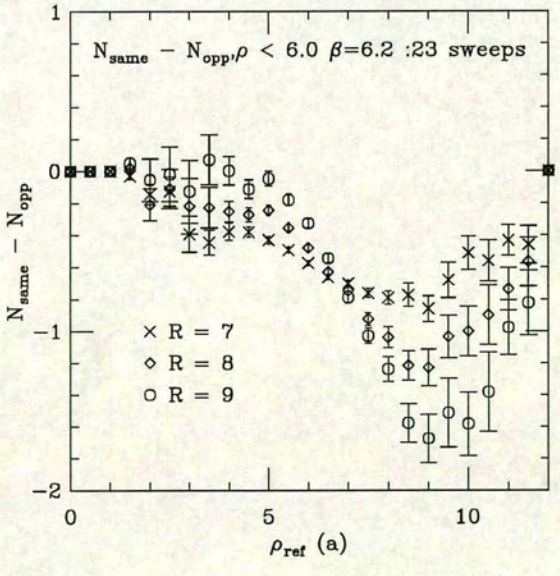

Figure 4.21: $N_{\text{same}} - N_{\text{opp}}$ vs ρ_{ref} : $\beta = 6.2$ 23 sweeps

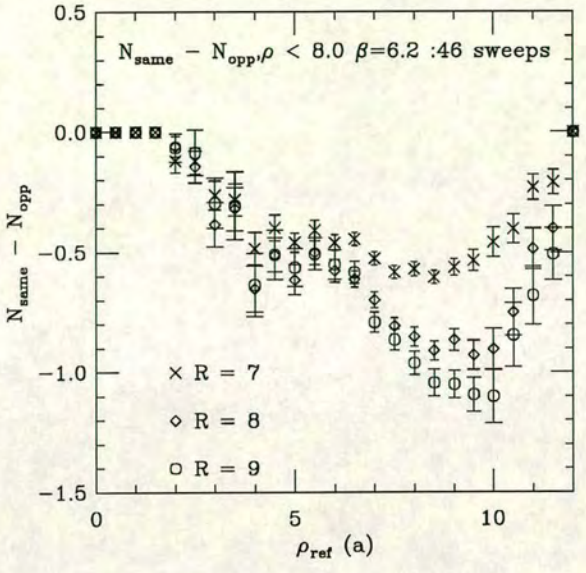

Figure 4.22: $N_{\text{same}} - N_{\text{opp}}$ vs ρ_{ref} : $\beta = 6.2$ 46 sweeps

instantons tend to have the same sign as each other while smaller than average instantons tend to be screened by large instantons.

The picture of the vacuum that emerges from this study is that there is a bias towards large instantons with one sign being overscreened by smaller than average instantons with the opposite sign. This picture explains both the large peak in $Q^2(\rho < \rho_{\text{cut}})$ and the behaviour of the function $C(\rho)$.

4.5 Finite volume effects

The results presented above have shown that there are many large instantons in the vacuum. In view of this it is necessary to check whether the calculation presented here is suffering from finite volume effects. The comparison is carried out at 46 sweeps at $\beta = 6.0$ on the $16^3 \times 48$ lattices and the $32^3 \times 64$ lattices. As a first check the size distributions are compared in figures 4.25 for the ρ_2 filter and in figures 4.26 for the ρ_3 filter.

The best fits to the data are given in table 4.4. The fits ranges are given in units of the string tension. For small instantons there are no finite volume effects

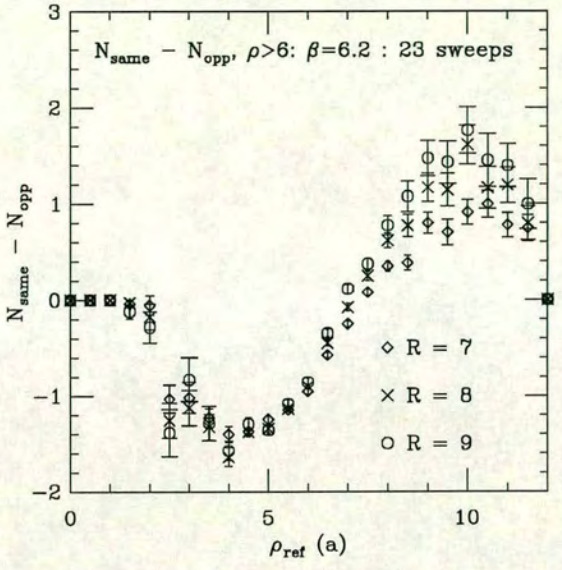

Figure 4.23: $N_{\text{same}} - N_{\text{opp}}$ vs ρ_{ref} : $\beta = 6.2$ 23 sweeps

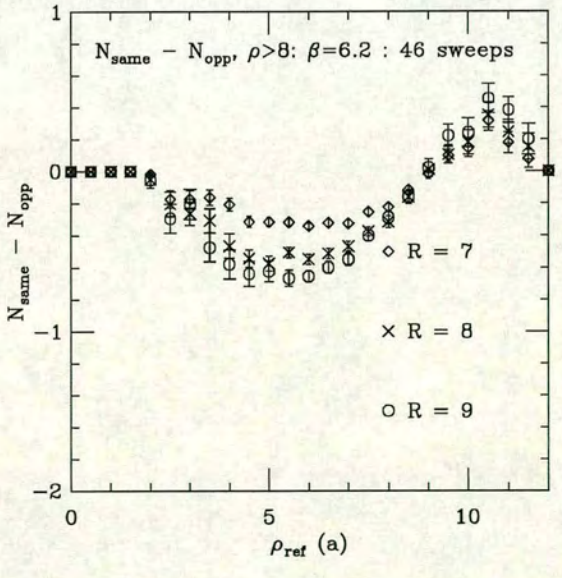

Figure 4.24: $N_{\text{same}} - N_{\text{opp}}$ vs ρ_{ref} : $\beta = 6.2$ 46 sweeps

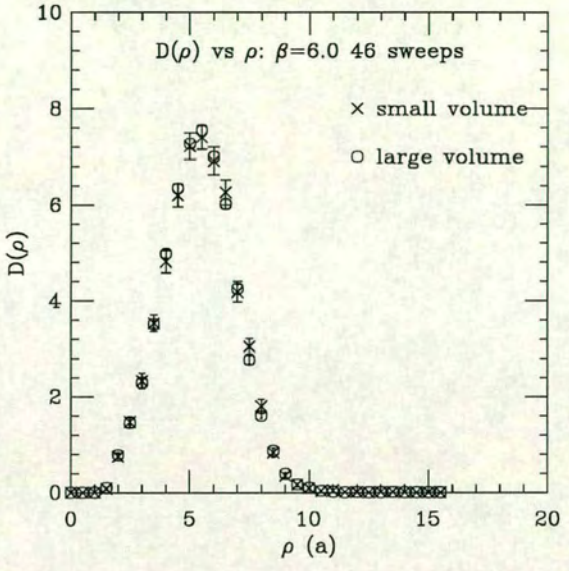

Figure 4.25: Comparison of size distributions : ρ_2 filter

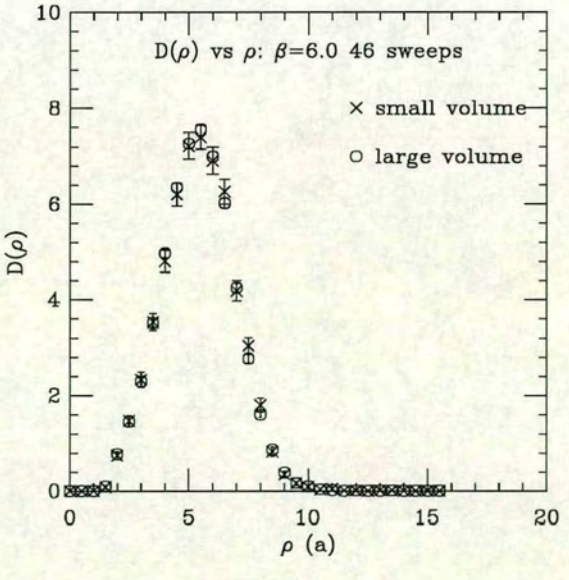

Figure 4.26: Comparison of size distributions : ρ_3 filter

β	sweep	range	α	χ^2/dof
6.0	46	$0.44 \rightarrow 0.99$	$2.58^{+0.040}_{-0.053}$	1.72
6.0	46	$1.87 \rightarrow 2.42$	$-14.93^{+0.74}_{-0.49}$	0.53

Table 4.4: Best fits to large volume data : ρ_2 filter

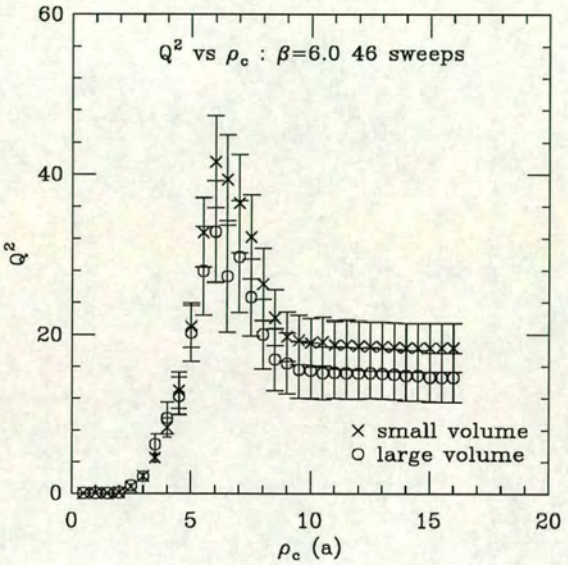

Figure 4.27: Comparison of $Q^2\rho \leq \rho_{\rm cut}$: ρ_2 filter

at all; the size distributions are quite consistent. In the large size tail of the distribution there are some discrepancies. The best fits do differ and do not agree within errors. However, this may be a result of the filter parameters used.

The behaviour of the $Q^2(\rho \leq \rho_{\rm cut})$ plots are also the same on the large and small volumes. The large volume also gives the peak in $Q^2(\rho \leq \rho_{\rm cut})$ near ρ_{peak} as shown in figure 4.27 (in this plot the value of $Q^2(\rho \leq \rho_{\rm cut})$ on the large volume has been divided by the ratio of the large to small volumes). Again the plot shows that the peak values on both volumes are consistent with each other and again there are no finite volume effects. It is therefore concluded that the size distributions are not showing any significant finite volume effects.

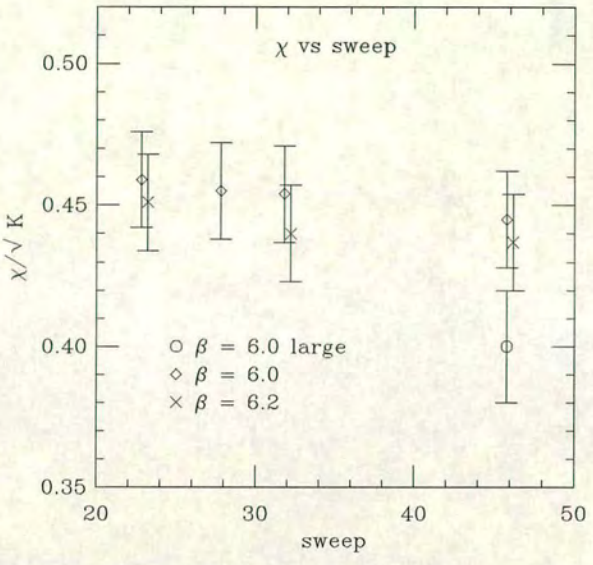

Figure 4.28: χ_t vs sweep

4.6 Topological Susceptibility

The topological $\chi_t^{\frac{1}{4}}$ has been calculated from

$$\chi_t = \frac{1}{V}\left\langle \left(\int d^4x Q(x) \right)^2 \right\rangle \tag{4.6}$$

In order to reduce the discretisation errors from small instantons in the vacuum the charge of each configuration is corrected by using equation 3.7 for each instanton. The topological charge is then rounded to the nearest integer and the topological susceptibility is calculated. The results for χ_t are plotted vs sweep for all the data sets analysed in figure 4.28 and given in table 4.5.

Note as the number of cooling sweeps is increased there is a slight decrease in the topological susceptibility at both $\beta = 6.0$ and $\beta = 6.2$. The calculated values of $\chi^{\frac{1}{4}}$, in physical units, are given in table 4.6. The value $\chi_t^{\frac{1}{4}}$ is taken at 46 sweeps at both $\beta = 6.2$, and $\beta = 6.0$ on the small lattice and on the large $\beta = 6.0$ lattice.

Note that there is a (small) discrepancy between $\chi_t^{\frac{1}{4}}$ calculated on the small

β	sweep	$\frac{\chi_t^{\frac{1}{4}}}{\sqrt{K}}$
6.2	23	0.451 ± 0.017
6.2	32	0.440 ± 0.017
6.2	46	0.437 ± 0.017
6.0	23	0.459 ± 0.017
6.0	28	0.455 ± 0.017
6.0	32	0.454 ± 0.017
6.0	46	0.445 ± 0.017
6.0 large	46	0.400 ± 0.020

Table 4.5: $\frac{\chi_t^{\frac{1}{4}}}{\sqrt{K}}$ vs sweep

β	$\chi_t^{\frac{1}{4}} MeV$
6.2	192.3 ± 7.5
6.0	195.8 ± 7.5
6.0_{large}	176.0 ± 8.8

Table 4.6: Physical values of $\chi_t^{\frac{1}{4}}$

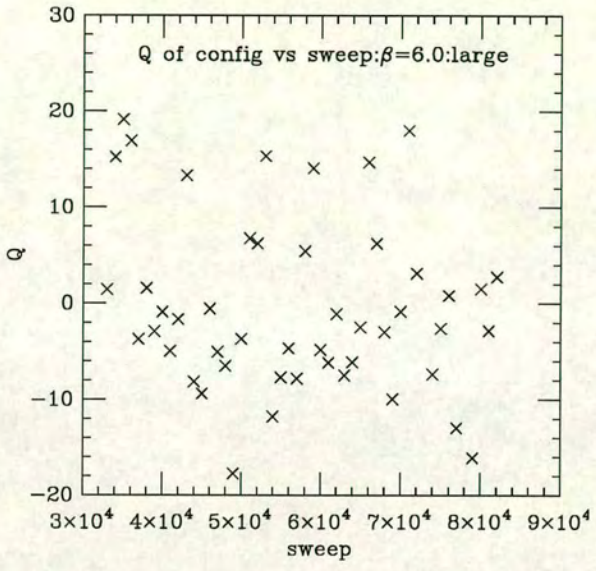

Figure 4.29: Q of config vs sweep

volume with $\chi_t^{\frac{1}{4}}$ calculated on the large volume at $\beta = 6.0$. If the error on the difference between $\chi_t^{\frac{1}{4}}$ on large and small volumes is calculated then the difference is 0.045 ± 0.026. Thus the discrepancy is a 2σ effect and so is not significant. Further, plotting the charge of the large configurations against update sweep suggests that there are correlations among the configurations (figure 4.29). It is therefore possible that the errors quoted above are not the true errors; they will be underestimates of the true error. Therefore no significance is placed on this discrepancy.

A naive extrapolation of the susceptibility on the small volumes can be carried out if the following relation is assumed.

$$\frac{\chi^{\frac{1}{4}}(a)}{\sqrt{K}} = \frac{\chi_{cont}^{\frac{1}{4}}}{\sqrt{K}} + ba^2K \tag{4.7}$$

One possible choice is to extrapolate the data after 46 cooling sweeps which gives $\chi_{cont}^{\frac{1}{4}} = 188 \pm 18\text{MeV}$. This agrees with the value predicted by Witten [13].

4.7 Conclusion

This chapter has described a calculation of the structure of the $SU(3)$ vacuum using the techniques described in chapters 2 and 3. In general the instanton sizes are peaked around $\rho \approx 1\sqrt{K}$. It has been shown that in the vacuum instantons in general will sit close to anti-instantons as expected. Evidence has also been discovered of overscreening of large instantons by small anti-instantons. It is possible to tune the cooling so that the distributions obtained will approximately scale and it has been checked that there are no significant finite volume effects.

However, the variation of the distributions under cooling demonstrates the major objection to using cooling. The results for the distributions depend on where the cooling is stopped (the best fits to the distributions vary with the amount of cooling) and scaling of the distributions can only be found at the expense of fine tuning the number of cooling sweeps.

The results discussed in chapters 2,3 and 4 will be presented in [35].

Chapter 5

Low-lying eigenvalues of the Wilson-Dirac operator

5.1 Introduction

5.1.1 Instanton zero modes in the continuum

In the continuum the zero modes of the Dirac operator $\not{D}$ on a given gauge configuration are related to its topological charge, Q, through the Atiyah-Singer theorem.

$$Q = n_+ - n_- \tag{5.1}$$

where $n_{+(-)}$ is the number of right(left) handed zero modes of the Dirac operator. A single instanton, in infinite volume satisfies the index theorem with a single right-handed zero mode. In regular gauge the zero mode has the form

$$\not{D}\ \psi = 0 \tag{5.2}$$

where

$$\psi = \frac{\rho^3}{(x^2+\rho^2)^{\frac{3}{2}}} u \tag{5.3}$$

where u is a constant right-handed spinor and ρ is the size of the underlying instanton. Similarly an anti-instanton satisfies the index theorem with a single left-handed zero mode.

The index theorem holds for any gauge configuration whether it is a solution of the gauge field equations of motion or not.

As described in Chapter 1 these zero modes lead to the solution of the $U(1)$ problem[3][15]. The zero modes of the Dirac Operator are related to chiral symmetry breaking through the Banks Casher relation

$$\langle \bar{\psi}(x)\psi(x) \rangle = \nu(0) \tag{5.4}$$

where $\nu(\lambda)$ is the eigenvalue density and chiral symmetry is broken if $\nu(0) \neq 0$. Lattice studies by Hands and Teper[36] with staggered fermions have indicated that instantons may be partially responsible for chiral symmetry breaking but it is not clear yet whether they are wholly responsible.

5.1.2 The Wilson-Dirac Operator

Naively discretising fermions on the lattice leads to 16 flavours of degenerate fermions in the continuum limit. This is a consequence of a theorem by Nielsen and Ninomiya [37] (the "No-go" theorem) which states that if the fermion action is translationally invariant, hermitian, local, bilinear in the fermion fields and has a continuous chiral symmetry then fermions occur in opposite chirality pairs. Wilson [38] cured this problem by adding the so-called Wilson term to the fermion action which gives all but one of the fermion flavours a mass of $O(\frac{1}{a})$ where a is the lattice spacing. In the continuum limit the mass of the doublers becomes infinite and they decouple from the theory.

On the lattice the Wilson-Dirac operator M is defined through

$$\begin{aligned}[M\psi](x) = \psi(x) - \kappa \sum_{\mu=1}^{4} \Big\{ & (1-\gamma_\mu) U_\mu(x) \psi(x+\mu) + \\ & (1+\gamma_\mu) U_\mu^\dagger(x-\mu) \psi(x-\mu) \Big\}\end{aligned} \tag{5.5}$$

with

$$\kappa = (2ma + 8)^{-1} \tag{5.6}$$

κ now takes the place of the quark mass and must be fixed during calculations. The addition of the Wilson term breaks chiral symmetry and introduces a renormalisation of the quark mass. In hadron spectrum calculations the renormalised quark mass is fixed by the following method. The quark mass, m_q, is taken to be zero where the pion mass is zero. The pion mass is calculated at a number of different κ values and linearly extrapolated in $\frac{1}{\kappa}$ to the point where $m_\pi = 0$. This κ value, denoted κ_c, defines $m_q = 0$. In the chiral regime $m_q a = \left(\frac{1}{\kappa} - \frac{1}{\kappa_c}\right)$.

The matrix M is γ_5 hermitian i.e.

$$M = \gamma_5 M^\dagger \gamma_5 \tag{5.7}$$

By considering the characteristic equation of M it can be shown that the eigenvalues of M are either real or come in complex conjugate pairs.

Further it can be shown that, for any eigenvectors r_i of M,

$$(\mu_k^* - \mu_i).r_k^\dagger \gamma_5 r_i = 0 \tag{5.8}$$

Defining the chirality as $\chi = r_i^\dagger \gamma_5 r_i$ shows that only modes with $\mu \in \mathcal{R}$ can have non-zero chirality; the other eigenmodes, those with complex λ must have $\chi = 0$.

Writing $M = (1 + \kappa R)$ it can be seen that the eigenvectors of M are independent of κ while the spectrum of M is shifted and dilated by varying κ. Further, only real modes of R can become zero modes of M at a particular κ value.

In the continuum only zero modes of $\not{D}$ can have $\chi \neq 0$ and this indicates that only the eigenvectors of M corresponding to real eigenvalues can play the role of zero modes in the continuum[39].

This discretisation is correct to $O(a)$. The operator can be fully $O(a)$ improved through the addition of the Clover term $c_{sw}\bar{\psi}\sigma_{\mu\nu}F_{\mu\nu}\psi$. c_{sw} has recently been determined non-perturbatively by the ALPHA collaboration allowing fully $O(a)$ improved simulations to be carried out [40]

5.1.3 The Hermitian matrix Q

For this study the low-lying eigenmodes, i.e. those with eigenvalues closest to zero, of **Q** have been investigated.

Q is defined through

$$\mathbf{Q} = c_0 \gamma_5 M \tag{5.9}$$

where c_0 defined by $c_0 = 1+8\kappa$ restricts the eigenvalues of the unimproved matrix to $[-1, 1]$. Unlike M, **Q** is hermitian and the eigenvectors and the eigenvalues of **Q** both depend non-trivially on κ. However, all hadronic observables can be computed in terms of **Q**:

$$M^{-1} = \mathbf{Q}^{-1} \gamma_5 c_o \tag{5.10}$$

The relation between **Q** and M is very complicated. The low-lying spectrum of $\mathbf{Q}(\kappa)$ is related to those eigenvalues of M closest to zero. Writing $M = 1 + \kappa R$ where R is the hopping term, then it can be seen that if ρ is a real eigenvalue of R then $M(\kappa)$ and $\mathbf{Q}(\kappa)$ have a common zero-mode at $\kappa_0 = -\frac{1}{\rho}$.

The non-trivial κ dependence of the eigenvalues and eigenvectors of **Q** means that to extract information about the spectrum of M it is necessary to calculate the low-lying modes of **Q** at different κ values; so-called κ scans.

An approximate dependence of the eigenvalues of **Q** on κ can be derived. If

$$Q(\kappa)\psi = \lambda(\kappa)\psi \tag{5.11}$$

then if $\kappa \to \kappa + \delta\kappa$, $\lambda \to \lambda + \delta\lambda$ with

$$\delta\lambda = \frac{\delta\kappa}{\kappa}(\lambda(\kappa) - \chi(\kappa)) + O\left(\frac{\delta\kappa}{\kappa}\right)^2 \tag{5.12}$$

In particular, if one is close to a zero mode then κ_0, position of the zero mode,

can be estimated by

$$\kappa_0 \approx \kappa \left(1 + \frac{\chi}{\lambda - \chi}\right) \tag{5.13}$$

This relation is used to guide searches for zero modes of $\mathbf{Q}$.

The chiralities of the eigenmodes of $\mathbf{Q}$ are related to the eigenvalues by

$$\chi_i(\kappa) = \frac{d\tilde{\lambda}_i}{d(1/\kappa)} \tag{5.14}$$

where

$$\tilde{\lambda} = \lambda \frac{(1 + 8\kappa)}{\kappa} \tag{5.15}$$

In particular

$$\chi_i(\kappa) = 0 \leftrightarrow \frac{d\tilde{\lambda}_i}{d(1/\kappa)} = 0 \tag{5.16}$$

Throughout this report, κ_0 corresponds to the position of the zero mode while κ_χ corresponds to the position of a zero of chirality (of the lowest non-zero mode).

5.1.4 A simple example : The free case

As a simple example of the relation between M and $\mathbf{Q}$ we consider the case where all the $U_\mu(x) = 1$. It is possible to derive the exact results for the spectrum in this case by Fourier transforming the matrix.

For M the spectrum on an L^4 lattice is given by

$$\lambda = \frac{1}{2\kappa} - \sum_\mu cos(p_\mu) \pm i \sqrt{\sum_\mu sin^2(p_\mu)} \tag{5.17}$$

where if periodic boundary conditions are imposed on the fermion fields

$$p_\mu = \nu \frac{2\pi}{L} : \nu = 0, ...L - 1 \tag{5.18}$$

and if anti-periodic boundary conditions are imposed

$$p_\mu = \nu \frac{2\pi}{L} : \nu = \frac{1}{2}, ..., L - \frac{1}{2} \tag{5.19}$$

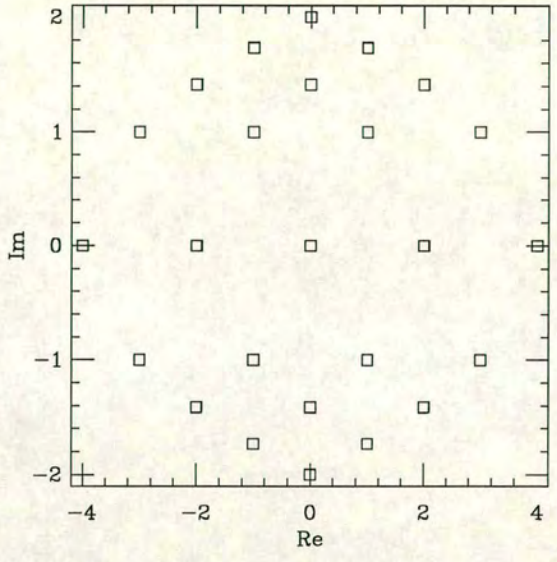

Figure 5.1: Spectrum of M: $L = 4$: periodic boundary conditions

The spectrum of the momentum dependent part, i.e. omitting the $\frac{1}{2\kappa}$ term and centering the spectrum on the origin is plotted for $L = 4$ in figure 5.1 for periodic boundary conditions and for anti-periodic boundary conditions imposed in the time direction in figure 5.2.

These plots explicitly show the symmetries of the spectrum of M. Note that if the gauge group is $SU(N)$ then there are $4N$ real modes, in the left hand leg of the spectrum with periodic boundary conditions whereas for the anti-periodic case there are none.

For $\mathbf{Q}^2$ the eigenvalues are given by

$$\lambda^2 = \sum_{\mu} sin^2(p_\mu) + \left(\frac{1}{2\kappa} - \sum_{\mu} cos(p_\mu) \right)^2 \tag{5.20}$$

This formula demonstrates explicitly the non-trivial dependence of the eigenvalues on κ. Note that in the free case

$$\lambda_Q^2 = |\lambda_M|^2 \tag{5.21}$$

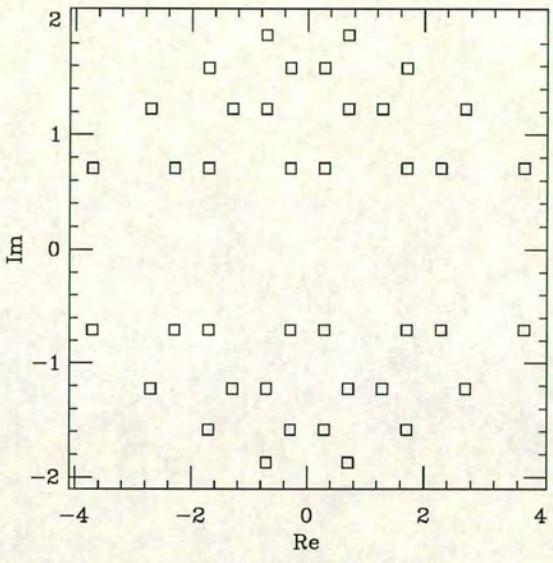

Figure 5.2: Spectrum of M: $L = 4$: anti-periodic boundary conditions

demonstrating that the low-lying eigenvectors of $\mathbf{Q}$ are related to the modes of M closest to the real axis.

The eigenvalues of $\mathbf{Q}^2$ are plotted for $L = 4$ with anti-periodic boundary conditions in figure 5.3 showing how as κ is varied different modes become the lowest.

With anti-periodic boundary conditions imposed in the 4 direction it can also be shown that the modes with the lowest momenta

$$p_\mu = \left(0, 0, 0, \frac{\pi}{L}\right) \tag{5.22}$$

have a zero of chirality at

$$\kappa_\chi = \frac{1}{2\left(3 + cos(\frac{\pi}{L})\right)} \tag{5.23}$$

This is just κ_{crit} for the free case with a volume correction which disappears as $L \to \infty$. This suggests that another measure of κ_{crit} may be κ_χ[41].

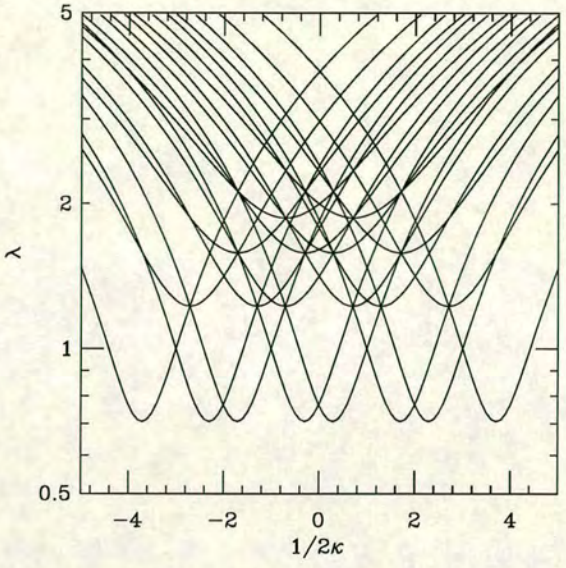

Figure 5.3: Spectrum of $\mathbf{Q}$: $L = 4$: anti-periodic boundary conditions

5.1.5 Calculation of the eigenmodes and eigenvectors

The eigenmodes of $\mathbf{Q}$ are calculated by using conjugate gradient to minimise the Ritz functional[42]

$$\frac{\langle \psi_k | \mathbf{Q}^2 | \psi_k \rangle}{\langle \psi_k | \psi_k \rangle} \tag{5.24}$$

Higher eigenmodes are calculated by finding ψ_k orthogonal to the approximate eigenspace spanned by previously calculated eigenvectors. The algorithm is accelerated by alternating incomplete conjugate gradient searches with intermediate diagonalisations of $\mathbf{Q}^2$ in the approximate eigenspace. The algorithm has the virtues of being numerically stable, giving rigorous error bounds on the eigenvalues and the correct degeneracies. This proceedure also gives the approximate eigenvectors of $\mathbf{Q}$ as well.

5.1.6 Localisation of the modes

To investigate the space-time localisation of the modes, the eigenvector density

$$\phi(x) = \psi^\dagger(x)\psi(x) \tag{5.25}$$

is calculated.

An estimate of how delocalised the mode is is given by the Participation Ratio (PR) which measures what fraction of the lattice the mode fills. It is defined by

$$PR = \frac{1}{V} \frac{(\sum_n \phi(x)^2)^2}{\sum_n (\phi^4(x))} \tag{5.26}$$

where V is the lattice volume. It has the properties

- if $PR = 1$ then $\phi(x) = c$, a constant.
- if $PR = \frac{1}{V}$ then $\phi(x) = \delta(0)$.
- if $\phi(x)$ is random, $PR = \frac{1}{3}$.

5.1.7 Instantons on the Lattice

As described in Chapter 2, on the lattice there is no real topology. Therefore it is necessary to investigate whether as we approach the continuum limit we regain continuum behaviour such as the index theorem [12]. In this chapter the index theorem is investigated on instanton configurations. The behaviour of the modes in the right hand leg of the spectrum is investigated as this is where hadron spectrum calculations are carried out.

As in chapter 2 the discretisation of [30] is used to set up the instantons on the lattice. The index theorem has been investigated on instanton configurations in 4-d with staggered fermions in [30] and with staggered fermions on thermalised configurations in [43]. Wilson fermions in 2-d have been investigated in [44] and [45] and in 4-d on thermalised configurations by [46].

In this chapter the instanton size quoted (except in the study of exceptional configurations) is the input parameter when the instanton was set up the instanton on the lattice. In plots of the size dependence of the low-lying modes the figures marking each point e.g. 2 corresponds to the size used to set up the instanton.

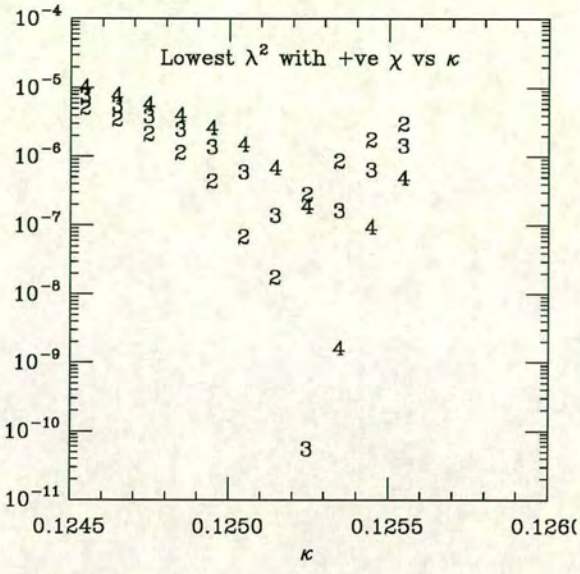

Figure 5.4: Lowest mode with positive chirality

5.2 Single Instanton with periodic boundary conditions

Consider the single instanton case, with periodic boundary conditions imposed on the fermion fields. The single instanton satisfies the index theorem by having 4 right handed zero modes and 3 left handed zero modes (with staggered fermions, where there are 4 degenerate flavours of fermion, it was found that the index theorem was satisfied with 16 right handed and 12 left handed modes [30])

The size dependence of the spectrum is shown in figures 5.4 and 5.5. The plots show kappa scans carried out on a 12^4 lattice. Figure 5.4 shows the lowest modes with positive chirality calculated with 3 different instanton sizes, and figure 5.5 is similar but for the lowest mode with negative chirality. It can be seen that as $\rho \to 0$, $\kappa_0 \to \frac{1}{8}$ from above.

The eigenvector density $\psi^\dagger(x)\psi(x)$ of the modes is very delocalised. For all the sizes calculated the participation parameter is greater than 0.9, indicating that the zero modes are spread out over most of the lattice.

Calculating the chirality of the zero modes shows that $\chi > 0.99$, while for the

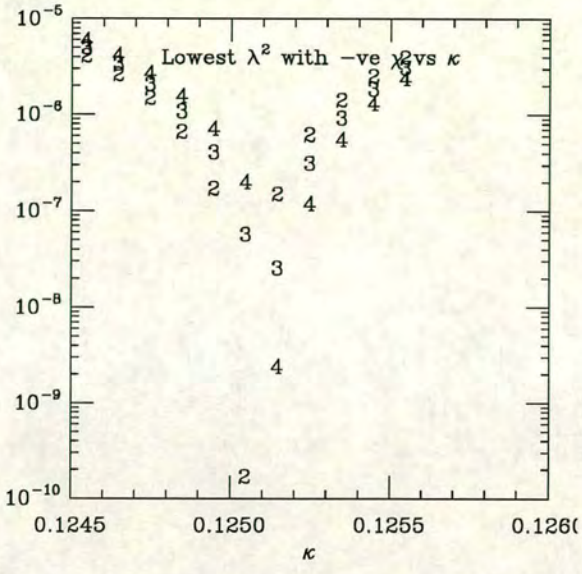

Figure 5.5: Lowest mode with negative chirality

other modes $\chi << 1$ at κ_0.

The size dependence of the spectrum can be explained as follows. If $\frac{\rho}{a} \to 0$ then the free case will be recovered because for ρ small enough the instanton falls through the lattice. In SU(2) the free case has 8 zero modes at $\kappa = 0.125$. The plots of size dependence show that, as ρ decreases, κ_0 moves towards $\kappa = 0.125$. Examining the first non zero mode of the spectrum it is seen that as $\rho \to 0$, $\chi \to -1$. Recall that in $SU(2)$ the free case had 4 right handed zero modes and 4 left handed zero modes; this shows that as $\rho \to 0$ the free case is restored. For periodic boundary conditions the index theorem is satisfied by the removal of a zero mode which restores itself as $\rho \to 0$.

When the clover term is added the index theorem is still satisfied with 4 right handed and 3 left handed zero modes. A single instanton corresponds to a very smooth gauge field; its average plaquette value is approximately 1, hence $c_{sw} = 1$ is used. The size dependence of κ_{min} has been lessened and all the zero modes lie between $\kappa = 0.125$ and $\kappa = 0.12505$; improvement has moved κ_0 closer to 0.125 for the instanton sizes considered. The absolute value of the chirality of the first

L	ρ	c_{sw}	κ_χ	κ_0
12	2	0	0.1260	0.135
12	3	0	0.1260	0.129
12	4	0	0.1263	0.127
12	2	1	0.1255	0.1258
12	3	1	0.1255	0.1251
12	4	1	0.1255	0.1250
16	2	0	0.1255	0.135
16	3	0	0.1255	0.129
16	4	0	0.1255	0.127
16	2	1	0.1255	0.1258
16	3	1	0.1255	0.1251
16	4	1	0.1255	0.1250

Table 5.1: Table of results for anti-periodic boundary conditions

non-zero mode is lower than that found with the unimproved operator and the chirality approaches -1 more slowly than in the unimproved case.

5.3 Anti-periodic boundary conditions

Consider now the case of a single discretised instanton with anti-periodic boundary conditions imposed on the fermion fields. [1]

In this case the single instanton satisfies the index theorem with one right-handed zero mode and no left-handed zero modes. As in the periodic case, κ_0 depends on the size of the underlying instanton. Table 5.1 gives the results for κ_0 and κ_χ of the lowest non-zero modes on all the lattices with all different sizes and Fig. 5.6 shows the size dependence of κ_0 on a 16^4 lattice with different size instantons.

In contrast to the periodic case, the smaller the underlying object the higher the value of κ_0. This can also be interpreted as the restoration of the free case as $\frac{\rho}{a} \to 0$. In the free case with anti-periodic boundary conditions in one direction

[1] The boundary conditions were imposed by flipping the sign of the links in the time direction on one time slice.

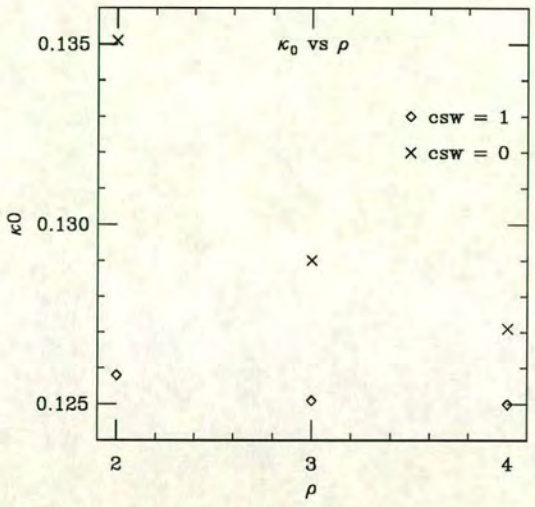

Figure 5.6: Size dependence of κ_0

there are no zero-modes, hence as the instanton is made smaller the single zero mode brought in by the instanton eventually disappears.

Adding in the improvement term with $c_{sw} = 1$ reduces the size dependence of κ_0 and it also moves κ_0 closer to $\frac{1}{8}$ at fixed ρ.

Discretisation effects are also shown by calculating the chirality of the modes. Figure 5.7 shows how $\chi \to 1$ as ρ is increased and as the clover term is added. The higher modes have a chirality crossing at κ_χ close to κ_0.

Recall that in the case of periodic boundary conditions the participation parameter of the zero mode was generally bigger than 0.9, indicating a very delocalised mode. In the anti-periodic case the participation parameter is $<< 1$ indicating a localised mode. The participation parameter is plotted versus the instanton size in figure 5.8. The plot shows that as ρ decreases the zero mode becomes more localised. It should also be noted that the improved zero mode is more localised than the unimproved zero-mode, but, as ρ increases, this difference becomes smaller (the smoother configuration has smaller discretisation effects). In both

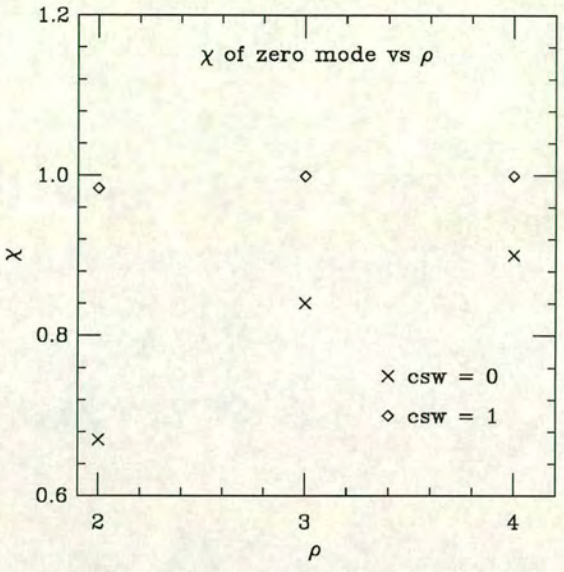

Figure 5.7: χ of mode vs ρ

the improved and unimproved cases the zero mode is centred on the instanton.

The volume dependence of the low-lying modes was also investigated by comparing the low-lying modes on 16^4 lattices with that calculated on 12^4 lattices. There was a very slight dependency of the low-lying modes on the volume of the system. Figure 5.9 shows the volume dependence of the low-lying modes with $\rho = 4$ and $c_{sw} = 0$, while figure 5.10 shows the volume dependence for $\rho = 4$ and $c_{sw} = 1$. Note also that the volume dependence is lessened by the introduction of the clover term. This may be related to the improved zero modes being more localised than the unimproved zero modes and so not being influenced so much by the boundary. Table 5.1 shows that κ_χ does not vary with ρ at least to the precision it was measured. The change in κ_χ of the $\rho = 4$ instanton with $L = 12$ and $c_{sw} = 0$ is a finite volume effect; it disappears on the $L = 16$ lattice. Note again that it also disappears with the introduction of the clover term. Finally, comparing κ_χ and κ_0 shows that increasing ρ and/or adding in the clover term makes $\kappa_\chi \to \kappa_0$.

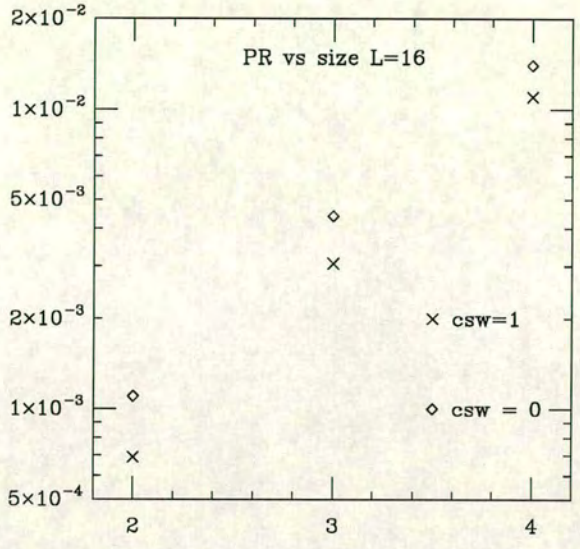

Figure 5.8: PR of zero-mode vs ρ

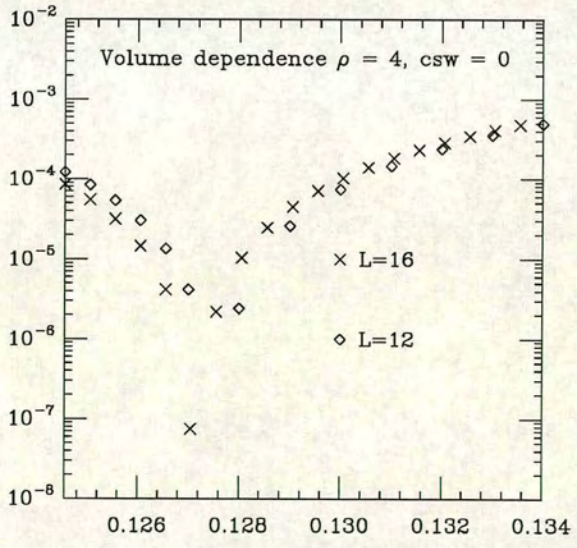

Figure 5.9: Volume dependence of low-lying modes $\rho = 4$, $c_{sw} = 0$

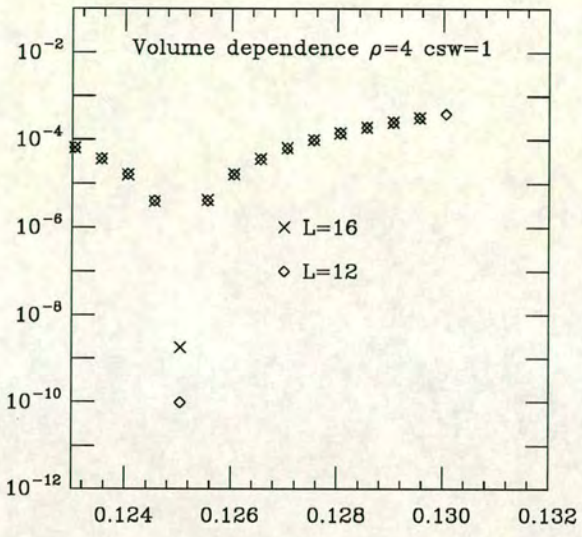

Figure 5.10: Volume dependence of low-lying modes $\rho = 4$, $c_{sw} = 1$

5.4 The effect of heating

The next question that is investigated is how the behaviour of the modes changes when noise is added to the system. Only the anti-periodic case is considered as this is what is relevant to hadron spectroscopy and the problem of exceptional configurations. The method is as follows. A cold instanton is set up on the lattice in the usual manner. Then the configuration is heated up using the *Cabibbo Marinari* heat bath at a chosen β value. The topological charge, Q, of the heated configuration was measured by the cooling algorithm [25]. In all plots of λ^2 vs κ and χ vs κ the bursts connected together by the solid line plot the lowest eigenmode of $\mathbf{Q}^2$, the squares to the second lowest mode and diamonds to the third lowest.

5.4.1 Stability of the modes during heating

In order to investigate this, cold instantons with $\rho = 2, 3, 4$ were heated up on a 12^4 lattice at $\beta = 6.0$. Zero mode searches were carried out at 5,10 and 15 sweeps with the unimproved operator. For each size four heatings were carried out.

For most of the configurations it was found that $Q = 1$ and that $n_+ = 1$ and $n_- = 0$. A typical scan is shown for a $\rho = 3$ instanton with a final $Q = 1$ in fig 5.11 (the first row corresponds to 5 sweeps, the 2nd to 10 sweeps and the 3rd to 15 sweeps).

Heating has two effects on the zero modes. Firstly κ_0 now varies from configuration to configuration and $\langle \kappa_0 \rangle$ on the heated configurations is close to κ_{crit} as measured from chiral extrapolations of m_π (for $\beta = 6.0$ and the unimproved action $\kappa_{crit} = 0.1571$ [47]). Secondly the chirality crossing of the higher modes has also moved to a higher κ value; κ_χ remains close to κ_{crit} and fluctuates much less than κ_0.

The modes on the heated configurations are localised; as in the cold case, the participation ratio $<< 1$. In all but one of the cases, the $\rho = 4$ case described below, the final Q value after 15 sweeps was $Q = 1$ and the maximum of the eigenvector density of the zero-mode remains close to the centre of the original instanton during the heating, showing the stability of the modes during heating.

When heating the instantons with $\rho = 2$ it was found that in two of the four cases the zero mode disappeared between 5 and 10 heating sweeps as shown in Fig. 5.12. Measuring the topological charge of these configurations after 10 and 15 sweeps using the cooling method, gave $Q = 0$ in accordance with the index theorem; this time the disappearance of the mode coincides with the removal of the instanton by the heating. However, on one of the configurations after 10 sweeps the *improved* operator has a zero mode at a very high kappa value, $\kappa_0 = 0.17465$. This shows that the improved operator is more sensitive to the narrow instantons than both the unimproved operator and the cooling method gives $Q = 0$.

Another discrepancy between the topological charge as measured by cooling and the topological charge from the zero modes was found in this study at $\beta = 6.0$. In one heating of a $\rho = 4$ instanton an extra zero mode of the *improved* operator appeared while the topological charge as measured by cooling remained at 1.

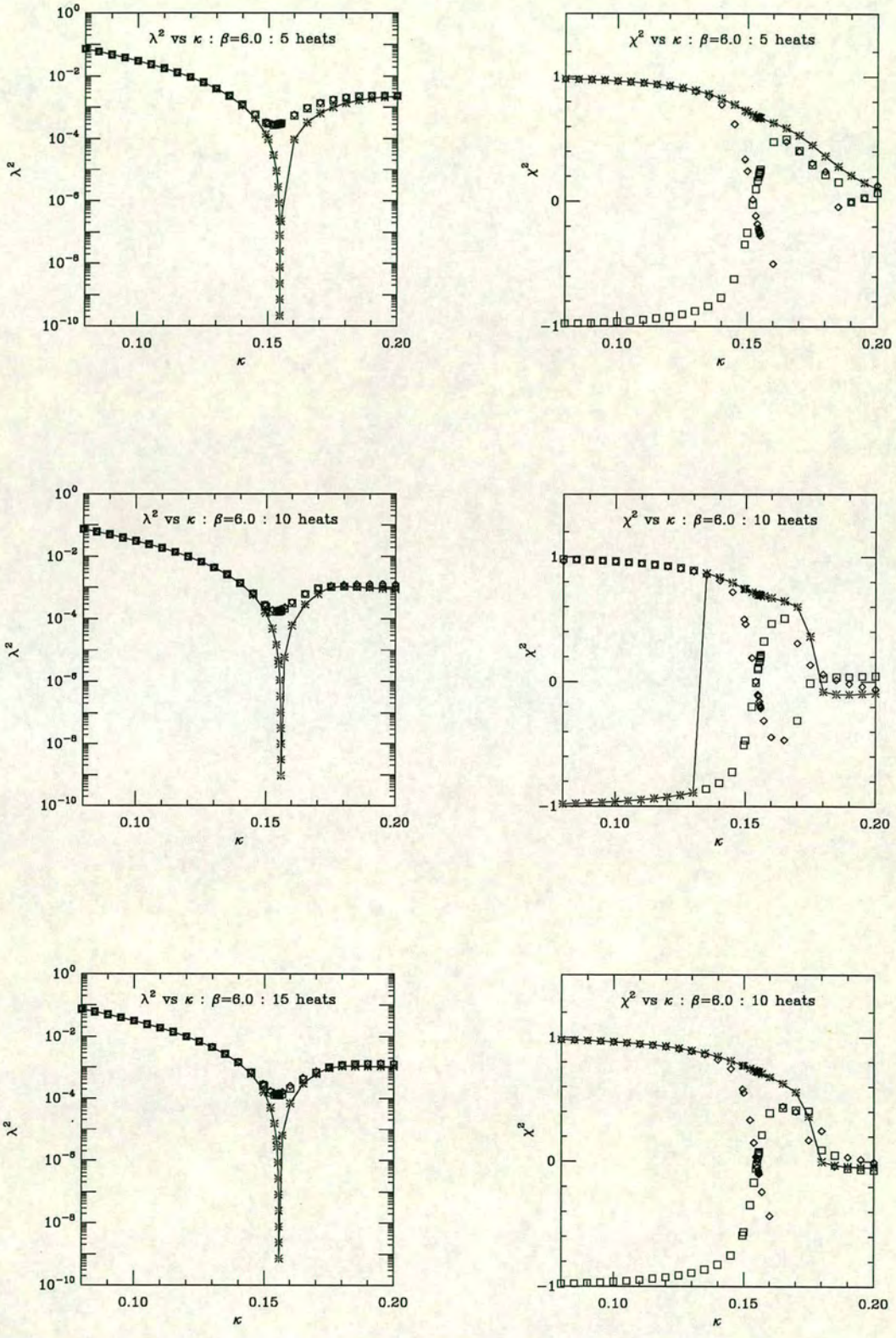

Figure 5.11: $\beta = 6.0 : \rho = 3$

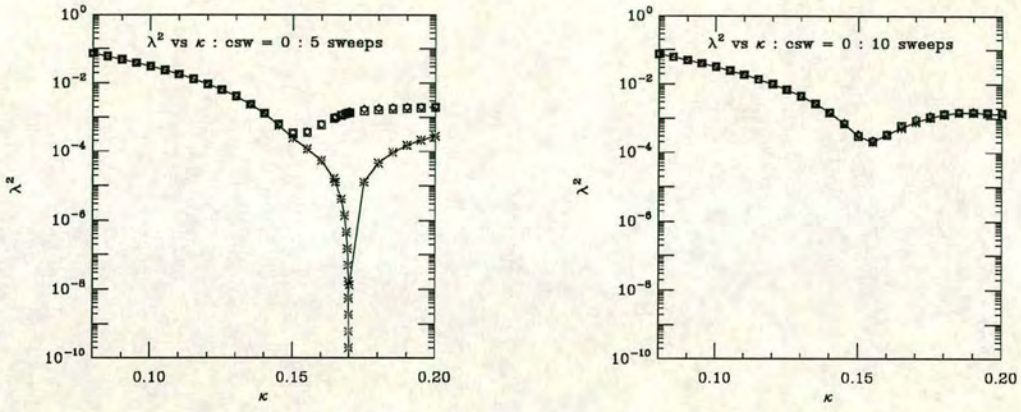

Figure 5.12: Disappearance of mode $\beta = 6.0 : \rho = 2$

Figure 5.13 shows both the improved and unimproved operators after 15 heating sweeps. Note that, for the κ range scanned, the zero mode only appears for the improved operator. The zero mode at the lower κ value corresponds to the original mode brought in by the instanton (it is localised close to the centre of the original instanton) while the mode at the higher κ value is centered at a different space-time point very far from the original object. Examining the cooling curve of this configuration shows no evidence of an instanton disappearing during cooling, hence it is likely that this zero mode belongs to a very narrow object that is removed during the first cooling sweeps. This interpretation is also supported by the higher κ_0 value of this mode (recall in the cold case the smaller the object the higher κ_0) and the observation that the mode is only seen in the κ range scanned for the improved operator. If there is a corresponding eigenmode for the unimproved operator then its κ_0 is at a very high κ value.

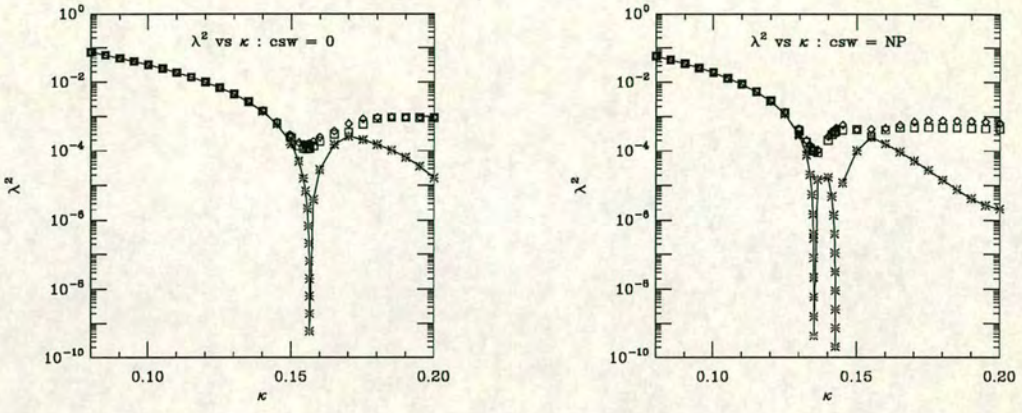

Figure 5.13: Appearance of extra zero-mode $\beta = 6.0$: $\rho = 4$

5.4.2 Heating at $\beta = 9.0$

This investigation was done on a 12^4 lattice with $\beta = 9.0$. The starting sizes were the same as before; $\rho = 2, 3, 4$ and these configurations were given 10 heat bath sweeps. The number of sweeps was chosen to ensure the average plaquette had reached its thermalised value. For $\rho = 3$ and $\rho = 4$, all 10 configurations had $Q = 1$, while for $\rho = 2$ only 8 did, the other 2 had $Q = 0$. As in the cold case both the improved and unimproved operators were investigated, c_{sw} was again calculated using the ALPHA formula [40].

Figures 5.14 and 5.15 show a typical scan on a heated instanton for $\rho = 2$ and $\rho = 4$ with both improved and unimproved operators. On all $\beta = 9.0$ configurations with $Q = 1$ it was found that the index theorem is satisfied with $n_+ = 1$ and $n_- = 0$, just as in the unheated case. Similarly, it was found that the zero mode was always localised on the core of the instanton, as in the unheated case.

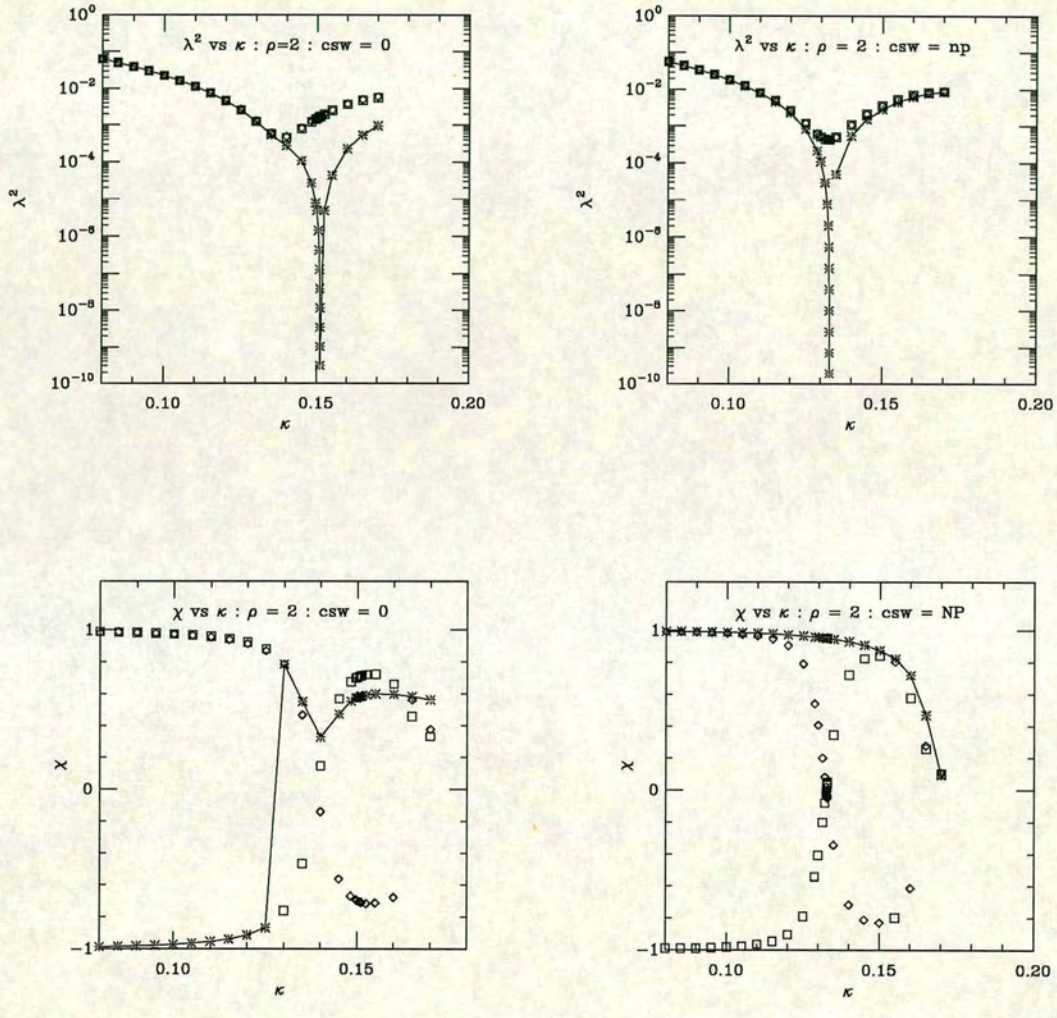

Figure 5.14: $\rho = 2\ \beta = 9.0$

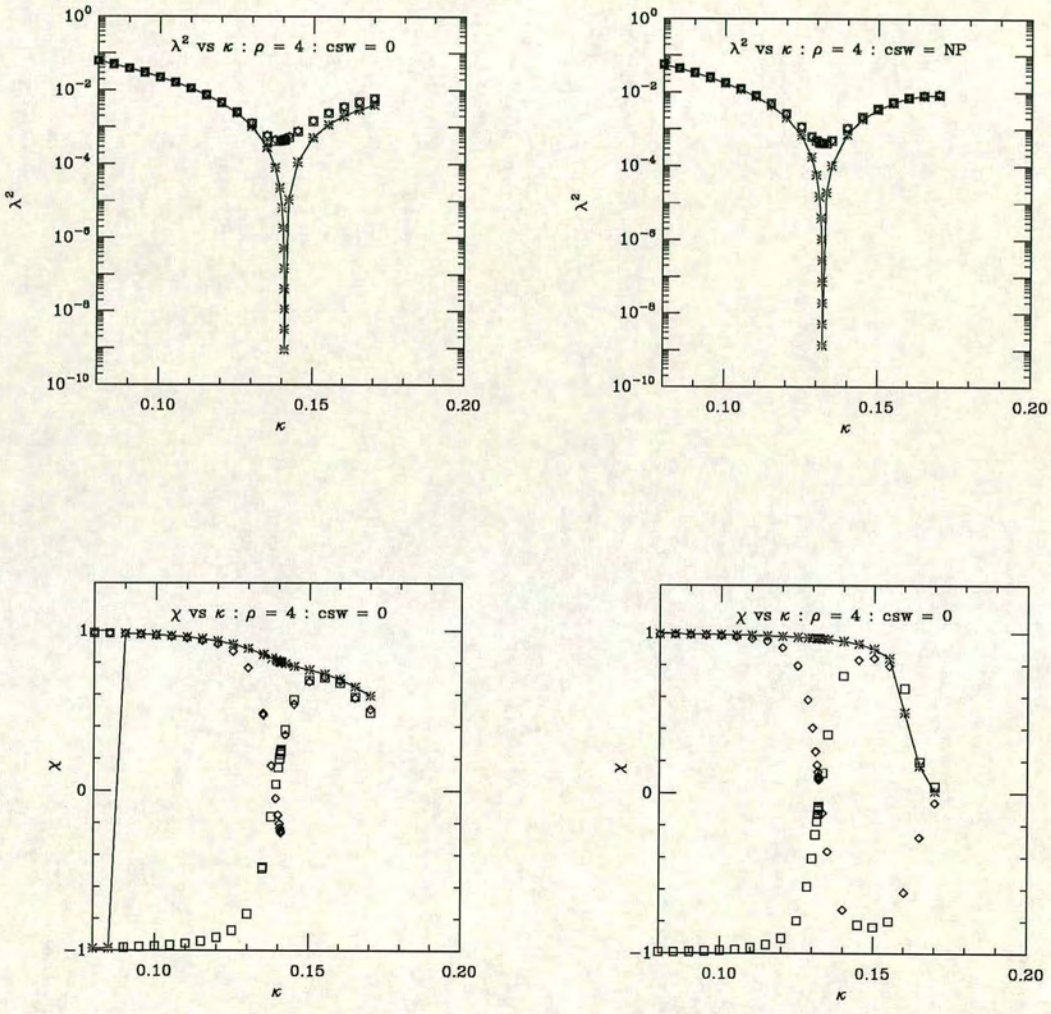

Figure 5.15: $\rho = 4$ $\beta = 9.0$

c_{sw}	ρ	$\langle\kappa_0\rangle$	$var(\kappa_0)$
0	2.0	0.1510	0.0053
0	3.0	0.1420	0.00098
0	4.0	0.1405	0.00039
1	2.0	0.1339	0.00156
1	3.0	0.1322	0.00013
1	4.0	0.1321	0.00005

Table 5.2: $\langle\kappa_0\rangle$ and $var(\kappa_0)$ for $\beta = 9.0$

As in the $\beta = 6.0$ case, it is found that for each starting size κ_0 fluctuates about a mean value $\langle\kappa_0\rangle$ with variance $var(\kappa_0)$. The results averaged over all configurations are shown in table 5.2 and plotted in Figure 5.16 and 5.17. The bars on each point correspond to the variance of κ_0 rather than the error.

The results show that the smaller the size of the instanton the larger the fluctuations in κ_0. There is some uncertainty with the final size of the $\rho = 2$ instantons, as they are more likely to be affected by the heating which may amplify $var(\kappa_0)$ but for $\rho = 3, 4$ the size of the instanton is not expected to vary much during the heating. For the unimproved operator, both $\langle\kappa_0\rangle$ and $var(\kappa_0)$ depend on the size of the original instanton. Adding the improvement term reduces the size dependence of $\langle\kappa_0\rangle$ and $var(\kappa_0)$. In fact, with these parameters $\langle\kappa_0\rangle$ for $\rho = 3$ and $\rho = 4$ are within $var(\kappa_0, \rho = 3)$ of each other.

The behaviour of κ_χ is analogous to its behaviour at $\beta = 6.0$. The heating again shifts κ_χ upwards. For $\beta = 9.0$, $0.139 < \kappa_\chi < 0.140$ for the unimproved operator and $0.132 < \kappa_\chi < 0.133$ for the improved operator. To the accuracy that κ_χ was measured, there is no variation of κ_χ with the size of the underlying object and $\delta\kappa_\chi \approx 0$. The data shows that $var(\kappa_\chi) << var(\kappa_0)$. This shows that unlike κ_0, κ_χ is both insensitive to the size of the underlying object and to the fluctuations of the gauge field.

As in the cold case, another effect of improvement can be seen in the chiralities of the zero-modes. Note again that increasing ρ or using the improved operator

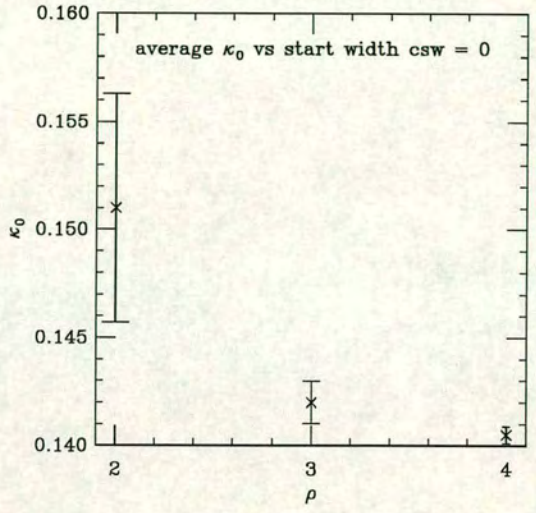

Figure 5.16: $\langle \kappa_0 \rangle \pm var(\kappa_0)$ vs ρ: $c_{sw} = 0$

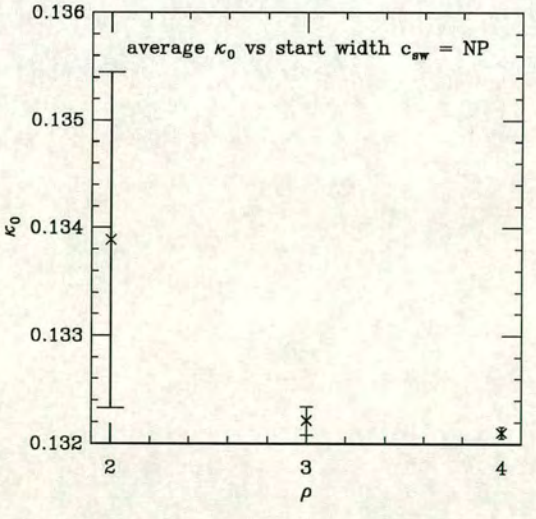

Figure 5.17: $\langle \kappa_0 \rangle \pm var(\kappa_0)$ vs ρ: $c_{sw} = NP$

makes the chirality of the zero mode closer to 1 and moves $\langle\kappa_0\rangle$ closer to κ_χ.

As described above, on all but two of the heated configurations, both with starting width $\rho = 2$, the topological charge of the configuration as measured by cooling is $Q = 1$ and the index theorem is satisfied with $n_+ = 1$ and $n_- = 0$. On one of the configurations where $Q = 0$ both the improved and unimproved operator have $n_+ = n_- = 0$ in the κ range investigated. In the other case it was found that the unimproved operator had $n_+ = n_- = 0$, while the improved operator had $n_+ = 1$ and $n_- = 0$ and $\kappa_0 = 0.1539$ very much higher than $\langle\kappa_0\rangle$. Examining the cooling curve of this configuration suggested that either heating had destroyed the instanton, or it had become very narrow. The zero-mode is centered on the original object which suggests the object has become very narrow. The conclusion from this and the $\beta = 6.0$ study is that the fermionic method of measuring topological charge (with the improved operator) is more sensitive to small objects and will record structure where cooling will record none.

5.5 Exceptional Configurations

5.5.1 The problem

Exceptional Configurations are those that have a zero-mode of the Wilson-Dirac Operator at a κ value that is in the physical region. These zero-modes show up as poles in the fermion propagator. For κ close to κ_0, the quark propagator is dominated by the lowest mode and these *exceptional* configurations dominate the final results. This is shown for the exceptional configurations encountered by UKQCD[48] in figures 5.18 and 5.19

Exceptional configurations are normally ignored in hadron spectrum calculations. However, Eichten et al [49] have recently introduced the Modified Quenched Approximation, which corrects for these exceptional poles in the propagator and leads to a suppresion of the large statistical errors associated with the exceptional configurations. The folklore of exceptional configurations is that they are more likely to appear for higher g^2, higher c_{sw} and larger volume.

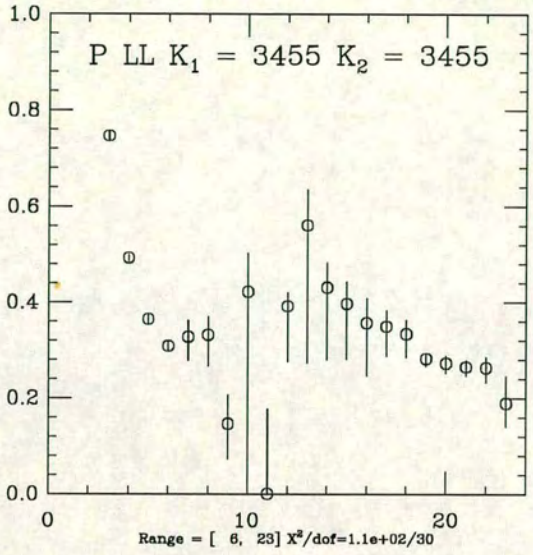

Figure 5.18: $\beta = 6.0$ pion effective mass including exceptional configurations

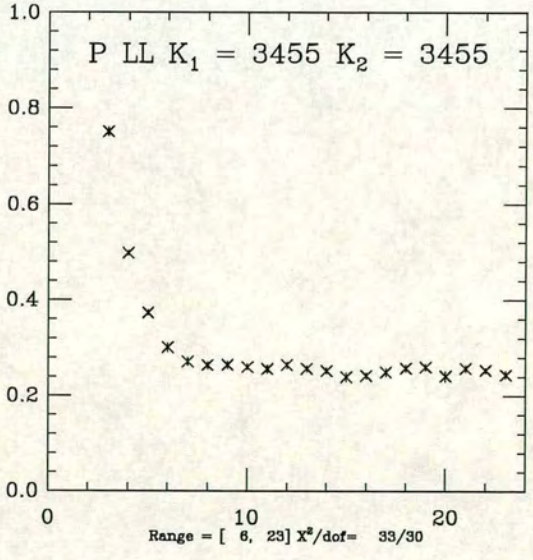

Figure 5.19: $\beta = 6.0$ pion effective mass excluding exceptional configurations

lattice	cfg#	χ	nearest object	size	distance	Q
$16^3 48$	1	+	+	2.0	0	-1
$16^3 48$	2	-	-	3.1	1	-9
$16^3 48$	3	+	+	2.0	1	+4
$32^3 64$	4	-	-	2.8	$\sqrt{2}$	-1

Table 5.3: Localisation of Exceptional Modes

This section investigates the space-time localisation properties of the four exceptional configurations encountered by UKQCD during their light hadron spectrum calculations. There were three discovered at $\beta = 6.0$ on $16^3 \times 48$ lattices and one on at $\beta = 6.0$ on a $32^3 \times 64$ lattice. The fermion action was the clover improved action using the non-perturbative value of c_{sw} suggested by the Alpha collaboration[40]. The actual quark masses where the UKQCD exceptional zero modes occur are of the order of $500MeV$ and therefore far below κ_{crit}.

5.5.2 Space-time localisation

We again consider the eigenvectors of $\mathbf{Q}$. In order to investigate the localisation, the eigenvector density is calculated and compared with the topological charge density. On the $16^3 \times 48$ lattices the comparison is carried out after 23 under-relaxed cooling sweeps with $\alpha = 1$ while on the large lattice the comparison is carried out after 46 under-relaxed cooling sweeps with $\alpha = 1$. (These are the same parameters used in the study of the vacuum in chapters 3 and 4. The widths of the instantons are calculated using the peak-iteration algorithm described in chapter 3.).

The results are summarised in the table 5.3 They show that the exceptional eigenvectors are localised close to an underlying topological object in the gauge configuration. The closest object is at most $\sqrt{2}$ lattice spacings away from the maximum of the eigenvector density. The sign of the chirality of the mode is correlated with the sign of the underlying instanton, but not correlated with the sign of the overall topological charge. A further point to note is that the closest

instanton is very small, both in terms of its size in lattice spacings and in physical units, where its size is less than the average instanton size found in chapter 4.

There is a strong hint here that the exceptional modes are related to small instantons in the underlying gauge field. If this is the case it could go some way to explaining part of the folklore. As the volume is increased at fixed β, the number of small instantons in the underlying gauge field will increase and therefore the number of exceptional modes would also increase. As β is lowered, the size distribution of the instantons will become smaller in lattice units. The size distribution will peak at a smaller number of lattice spacings and therefore the number of small instantons will increase.

5.6 Conclusions

This study has shown how a single instanton satisfies the index theorem on the lattice both in the cold case and after heating.

In the cold case, it was found that on a single instanton configuration with periodic boundary conditions imposed on the fermions, the index theorem was satisfied with $n_+ = 4$ and $n_- = 3$ while in the anti-periodic case $n_+ = 1$ and $n_- = 0$. The position of the zero-modes and the chiralities are sensitive to the discretisation errors. The inclusion of the improvement term has been seen to have a significant effect on both the chiralities and positions of the zero modes.

In the heated case, only the anti-periodic case was investigated as this is the case encountered in hadron spectrum calculations. By following the modes during the heating it has been shown that the zero-modes are stable during the heating. At $\beta = 9.0$ the fluctuations in κ_0 were measured and shown to increase as the underlying object is made smaller. The heating study again showed the index theorem was satisfied with $n_+ = 1$ and $n_- = 0$. Discrepancies between Q and $n_+ - n_-$ only appeared for the improved operator (extra zero modes for the unimproved operator were not seen). This can be explained by the coarseness of the measurement of Q by the cooling method; it misses small instantons while the improved Wilson operator has a zero mode indicating the presence of an

instanton-like object.

The larger fluctuations in κ_0 for smaller ρ and the investigation of the localisation of exceptional eigenmodes suggests that the problem of exceptional configurations is related to the presence of small instantons in the underlying gauge field.

The κ-value of vanishing chirality of the lowest non-zero modes, κ_χ, seems to be an interesting quantity to characterise the "bulk" modes of the spectrum. On cold and heated instantons κ_χ is fairly insensitive to the size of the underlying instanton and $var(\kappa_\chi) << var(\kappa_0)$. Moreover, in the cases where it could be compared with the known value of κ_{crit} (the $\beta = 6.0$ configurations) κ_χ appears closely related to κ_{crit}. This supports the idea of Simma [41] that κ_χ may be a better quantity than κ_0 to characterise κ_{crit} for single configurations.

The results presented in this chapter will be published in [50].

Chapter 6

Conclusions

This thesis has investigated the structure of the $SU(3)$ vacuum using under-relaxed cooling and carried out an exploratory study of the low-lying eigenmodes of the Wilson-Dirac Operator on instanton configurations.

The study of the structure of the vacuum has investigated the size and spatial distributions of the instantons. Correlations amongst the instantons have also been investigated. It has been found that the average size of the instantons on the cooled configurations is $\frac{1}{\sqrt{K}}$ and that instantons and anti-instantons sit close together in the vacuum as expected. More interestingly, it has been found that large instantons are *overscreened* by small anti-instantons.

Future work on the vacuum structure of $SU(3)$ gauge theory should perhaps be carried out at higher β values. This would enable a fuller investigation of the scaling of the distributions to be carried out. The results presented in chapter 4 have shown that there is rapid variation of the number of peaks in the vacuum during cooling; a higher β value will mean that both the sizes of and distances between instantons will be bigger (in lattice units) and short cooling should therefore not affect the distributions so much.

A further investigation will be whether light fermions have any effect on the instanton distributions. For a single flavour of quark $\langle Q^2 \rangle$ is given by [51]

$$\langle Q^2 \rangle \propto mV \tag{6.1}$$

where m is the mass of the quark and V is the volume of space-time. For light

quark masses, the susceptibility is suppressed and if $m = 0$, $\langle Q \rangle = 0$; for every instanton there will be an anti-instanton, the screening will be exact. However, there may still be the division between large and small instantons; on each configuration an investigation of $Q^2(\rho < \rho_{cut})$ may still reveal a large peak at some value of ρ_{cut} indicating that small instantons are screening large anti-instantons.

A mechanism for the overscreening of large instantons by small anti-instantons is as yet unknown. The effect of such behaviour on physics also needs investigating.

This thesis has also examined the appearance and spacetime localisation properties of the zero modes of the unimproved and improved Wilson-Dirac operator on single instanton configurations (both cold and heated).

In general the κ dependence of the low-lying eigenvalues and the nature of the localisation of the eigenmodes deserves further investigation on thermalised (multi-instanton) configurations and finally on unquenched configurations. An interesting question in this context is to what extent quark propagators and hadronic correlation functions are dominated by the low-lying modes. This is assumed in the interacting instanton liquid model and an investigation of these issues has also been started by Negele[52].

For the exceptional configurations, it should be investigated whether one can clearly identify properties of the topological charge distribution that lead to the appearance of exceptional modes. A related question to this is how the charge correlations discovered during the cooling investigation affect the localisation of the modes. Moreover, it is necessary to understand whether the exceptional modes are related to relevant physical effects or whether they are effects of the lattice discretisation (as suggested by their origin from small objects). Such an investigation must then finally be extended to configurations generated with the inclusion of dynamical fermion effects.

References

[1] D. Gross and F. Wilczek. Asymptotically free gauge theories. 1. *Phys. Rev. D*, **8**, 3633, (1973).

[2] D. Gross and F. Wilczek. Ultraviolet behaviour of non-abelian gauge theories. **30**, 1343, (1973).

[3] S. Coleman. The Uses of Instantons, chapter 7, page 265. Cambridge University Press, Cambridge, 1985.

[4] C. Nash and S. Sen. Topology and Geometry for Physicists. Academic Press, London, 1983.

[5] A. A. Belavin et. al. Pseudoparticle solutions of the Yang-Mills Equations. *Phys. Lett.*, **59B**, 85, (1975).

[6] C. G. Callan Jnr et. al. Towards a theory of the strong interactions. *Phys. Rev. D*, **17**, 2717, (1978).

[7] R. Jackiw and C. Rebbi. Vacuum Periodicity in a Yang-Mills Quantum Theory. *Phys. Rev. Lett*, **37**, 172, (1976).

[8] D. Bailin and A. Love. Introduction to Gauge Field Theory. Institute of Physics Publishing, Techno House, Redcliffe Way, Bristol, 1993.

[9] G. A. Christos. Chiral Symmetry and the U(1) problem. *Physics Reports*, **116**, 252, (1984).

[10] S. Weinberg. The Quantum Theory of Fields Vol 2. Cambridge University Press, The Pitt Building, Trumpington Street, Cambridge, 1996.

[11] R. Rajamaran. An Introduction to Solitons and Instantons in Quantum Field Theory. North-Holland Physics Publishing, P.O. Box 103, 1000 AC Amsterdam, The Netherlands, 1982.

[12] M. Atiyah and I. Singer. *Annals of Mathematics*, **87**, 484, (1968).

[13] E. Witten. Current Algebra Theorems for the U(1) Goldstone Boson. *Nucl. Phys. B*, **156B**, 269, (1979).

[14] G. 't Hooft. A Planar Diagram Theory for the Strong Interactions. *Nucl. Phys. B*, **72B**, 461, (1974).

[15] G. 't Hooft. Computation of the quantum effects of a four-dimensional pseudoparticle. *Phys. Rev. D*, **14**, 3432, (1976).

[16] T. Schäfer and E.V. Shuryak. Instantons in QCD. *hep-ph/9610451.*

[17] Meng-yuan Wang. On multiple instanton anti-instanton Configurations. *hep-ph/9502332.*

[18] E.V. Shuryak. The Interacting Instanton Liquid in QCD at zero and finite temperature. *Phys. Rev. D*, **53**, 6522, (1996).

[19] D.G.R. Pugh and M.J. Teper. Topological dislocations in the continuum limit of SU(2) lattice gauge theory. *Phys. Lett.*, **B224**, 159, (1989).

[20] M. Campostrani et.al. The topological susceptibility on the lattice. *Phys. Lett.*, **B212**, 206, (1988).

[21] C. Christou et. al. Improving the topological charge density operator on the lattice. *Nucl. Phys. B (Proc. Suppl.)*, **47**, 266, (1996).

[22] B. Alles et. al. Topological susceptibility at zero and finite T in SU(3) Yang-ills theory. *Nucl. Phys. B*, **494**, 281, (1997).

[23] C. Christou et. al. Improved lattice operators: the case of the topological charge density. *Phys. Rev. D*, **53**, 2619, (1996).

[24] J. Hoek et al. Topological fluctuations and susceptibility in SU(3) lattice gauge theory. *Nucl. Phys. B*, **288**, 589, (1987).

[25] M. Teper. Unmasking the topological charge content of fluctuating lattice gauge fields. *Phys. Lett.*, **B232**, 227, (1989).

[26] Philippe de Forcrand et. al. *Nucl. Phys. B*, **499**, 409, (1997).

[27] P.S. Spencer and C.M. Michael. Topography of the cooled O(3) vacuum. *hep-lat/9401011.*

[28] P.S. Spencer and C.M. Michael. Instanton size distribution in O(3).

[29] P.S. Spencer and C.M. Michael. Cooling and the SU(2) instanton vacuum. *Phys. Rev. D*, **52**, 4691, (1995).

[30] M.L. Laursen et. al. Small scale instantons, staggered fermions and the topological susceptibility. *Nucl. Phys. B*, **343**, 522, (1990).

[31] M.C. Chu et al. Evidence for the role of instantons in hadron structure from lattice QCD . *Phys. Rev. D*, **49**, 6039, (1994).

[32] Pierre van Baal. *hep-lat/9709066.*

[33] M. Teper. *Private Communication.*

[34] Philippe de Forcrand et. al. *hep-lat/9710001.*

[35] D. Smith and M. Teper. In Preparation.

[36] S.J. Hands and M.J. Teper. On the value and origin of the chiral condensate in quenched SU(2) lattice gauge theory. *Nucl. Phys. B*, **347**, 819, (1990).

[37] H.B. Nielsen and M. Ninomiya. Absence of neutrinos on a lattice 1. Proof by Homotopy theory. *Nucl. Phys. B*, **185**, 20, (1981).

[38] K.G. Wilson. Plenum Press, 1975.

[39] C. R. Gattringer et al. Topological charge and the spectrum of the Fermion Matrix in Lattice-QED2. *hep-lat/9707011.*

[40] M. Lüscher et. al. Non perturbative O(a) improvement of lattice QCD. *Nucl. Phys. B*, **491**, 323, (1997).

[41] H. Simma. Private communication.

[42] T. Kalkreuter and H. Simma. An accelerated conjugate gradient algorithm to compute low-lying eigenvalues: a study for the Dirac operator in SU(2) lattice QCD. *Comp. Phys. Comm*, **93**, 33, (1996).

[43] I.G. Barbour and M.J. Teper. Topology and zero modes in the SU(2) lattice gauge vacuum. *Phys. Lett.*, **B175**, 445, (1986).

[44] Jan Smit and Jeroen C. Vink. Remnants of the index theorem on the lattice. *Nucl. Phys. B*, **286**, 485, (1987).

[45] Jeroen C. Vink. Topological charge and fermions in the 2-d lattice U(1) model 2. Wilson fermions. *Nucl. Phys. B*, **307**, 549, (1988).

[46] S. Itoh et. al. The U(1) problem and topological excitations on a lattice. *Phys. Rev. D*, **36**, 527, (1987).

[47] T. Bhattacharya et. al. Hadron spectrum with Wilson fermions. *Phys. Rev. D*, **53**, 6486, (1996).

[48] P.A. Rowland. Light Hadron Spectroscopy in Quenched QCD. PhD thesis, University of Edinburgh, 1997.

[49] W. Bardeen et al. Light Quarks, Zero modes and Exceptional Configurations. *hep-lat/9705008.*

[50] H. Simma and D. Smith. In Preparation.

[51] N. Dowrick and M. Teper. Instantons, chiral symmetry breaking and the fate of the ultimate quenched calculation. *Nucl. Phys. B (Proc. Suppl.)*, **42**, 237, (1995).

[52] J.W. Negele. Insight into Hadron Structure from Lattice QCD. *hep-lat/9709129.*